

Journal of Mechanics of Materials and Structures

Special issue

**Trends in Continuum Physics
(TRECOP 2014)**

Volume 11, No. 1

January 2016



JOURNAL OF MECHANICS OF MATERIALS AND STRUCTURES

msp.org/jomms

Founded by Charles R. Steele and Marie-Louise Steele

EDITORIAL BOARD

ADAIR R. AGUIAR University of São Paulo at São Carlos, Brazil
KATIA BERTOLDI Harvard University, USA
DAVIDE BIGONI University of Trento, Italy
YIBIN FU Keele University, UK
IWONA JASIUK University of Illinois at Urbana-Champaign, USA
C. W. LIM City University of Hong Kong
THOMAS J. PENCE Michigan State University, USA
DAVID STEIGMANN University of California at Berkeley, USA

ADVISORY BOARD

J. P. CARTER University of Sydney, Australia
D. H. HODGES Georgia Institute of Technology, USA
J. HUTCHINSON Harvard University, USA
D. PAMPLONA Universidade Católica do Rio de Janeiro, Brazil
M. B. RUBIN Technion, Haifa, Israel

PRODUCTION production@msp.org

SILVIO LEVY Scientific Editor

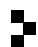
Cover photo: Ev Shafir

See msp.org/jomms for submission guidelines.

JoMMS (ISSN 1559-3959) at Mathematical Sciences Publishers, 798 Evans Hall #6840, c/o University of California, Berkeley, CA 94720-3840, is published in 10 issues a year. The subscription price for 2016 is US\$575/year for the electronic version, and \$735/year (+\$60, if shipping outside the US) for print and electronic. Subscriptions, requests for back issues, and changes of address should be sent to MSP.

JoMMS peer-review and production is managed by EditFLOW® from Mathematical Sciences Publishers.

PUBLISHED BY

 **mathematical sciences publishers**
nonprofit scientific publishing

<http://msp.org/>

© 2016 Mathematical Sciences Publishers

PREFACE

BOGDAN T. MARUSZEWSKI, WOLFGANG MUSCHIK,
ANDRZEJ RADOWICZ AND KRZYSZTOF W. WOJCIECHOWSKI

Guest Editors

Trends in Continuum Physics (acronym TRECOP) is the name of the scientific branch that concerns and focuses itself around many physical problems which can be described by continuum models. Special emphasis is placed on the representation of various concepts applied to different physical fields interacting with each other. Special stress is put on the mechanical side of the investigations made within TRECOP.

The scope of the TRECOP includes fundamentals of continuum physics, new trends in thermodynamics and in electrodynamics, physics of materials (encompassing defective crystals, ferroic crystals, liquid crystals, molecular crystals, high-temperature superconductors, semiconductors, plasma, polymers, amorphous media, smart materials, and anomalous material phenomena (such as auxetics, negative thermal expansion and other negative ones in materials)), biophysics, biomedical mechanics, multiphase systems, and multiscale also nanoscale problems. These fields have been developing fast in recent years. So TRECOP as itself can be treated as an young branch of research.

The Trends in Continuum Physics as the scientific branch was born and then was developed by international symposia which had the same name. The idea to organize those meetings comes from three persons: Bogdan T. Maruszewski, Wolfgang Muschik and Andrzej Radowicz. The symposia took place since 1998: in Poznań, Poland (1998, 2001, 2004, 2014), in Lviv, Ukraine (2007) and in Msida, Malta (2010). One of the main aims of those meetings has initially been to bring together scientists from Eastern Europe working in different fields of continuum physics, broadly understood, as well as those from Western and Central Europe, in order to extend their cooperation and to create new connections and acquaintances.

In this place should be presented a list (certainly incomplete) of scientists who have been developing the TRECOP scientific branch:

- Vladimir Alshits* — Institute of Crystallography, Russian Academy Sciences,
Moscow, Russia
- Jan Awrejcewicz* — Łódź University of Technology, Łódź, Poland
- Arkadi Berezowski* — CENS — Institute of Cybernetics, Tallinn, Estonia
- Yaroslav Burak* — Institute of Applied Mathematics and Mechanics, Ukrainian
National Academy of Sciences, Lviv, Ukraine
- Yevhen Chaplya* — Pitstrihach Institute of Applied Problems of Mechanics and Mathematics,
Ukrainian National Academy of Sciences, Lviv, Ukraine

- Enzo Ciancio* — Università di Messina, Messina, Italy
Juri Engelbrecht — Estonian Academy of Sciences, Tallinn, Estonia
Joseph N. Grima — University of Malta, Msida, Malta
Karl H. Hoffmann — Chemnitz University of Technology, Chemnitz, Germany
David Jou — University of Barcelona, Barcelona, Spain
Jan A. Kołodziej — Poznań University of Technology, Poznań, Poland
Józef Kubik — Kazimierz Wielki University, Bydgoszcz, Poland
Georgy Lebon — Liège University, Liège, Belgium
Bogdan T. Maruszewski — Poznań University of Technology, Poznań, Poland
Stanisław Matysiak — Warsaw University, Warsaw, Poland
Gerard A. Maugin — University of Paris VI, Paris, France
Wolfgang Muschik — Technische Universität Berlin, Berlin, Germany
Henryk Petryk — Institute of Fundamental Technological Research, Polish Academy of Sciences, Warsaw, Poland
Andrzej Radowicz — Kielce University of Technology, Kielce, Poland
Liliana Restuccia — Università di Messina, Messina, Italy
Jeremiah Rushchitsky — Institute of Mechanics, Ukrainian National of Sciences, Kiev, Ukraine
Jarosław Rybicki — Gdańsk University of Technology, Gdańsk, Poland
Czesław Rymarz — Institute of Fundamental Technological Research, Polish Academy of Sciences, Warsaw, Poland
Igor Selezov — Institute of Hydromechanics, Ukrainian National Academy of Sciences, Kiev, Ukraine
Stanisław Sieniutycz — Warsaw University of Technology, Warsaw, Poland
Gwidon Szefer — Cracow University of Technology, Cracow, Poland
Alfons A. F. van de Ven — Eindhoven University of Technology, Eindhoven, The Netherlands
Krzysztof W. Wojciechowski — Institute of Molecular Physics, Polish Academy of Sciences, Poznań, Poland

BOGDAN T. MARUSZEWSKI: bogdan.maruszewski@put.poznan.pl

Institute of Applied Mechanics, Poznań University of Technology, ul. Jana Pawła II 24, 60-965 Poznań, Poland

WOLFGANG MUSCHIK: muschik@mailbox.tu-berlin.de

Institut für Theoretische Physik, Technische Universität Berlin, EW 7-1, Hardenbergstraße 36, 10623 Berlin, Germany

ANDRZEJ RADOWICZ: radowicz@tu.kielce.pl

Chair of Mechanics, Kielce University of Technology, ul. Tysiąclecia, Państwa Polskiego 7, 25-314 Kielce, Poland

KRZYSZTOF W. WOJCIECHOWSKI: kww@ifmpan.poznan.pl

Institute of Molecular Physics, Polish Academy of Sciences, ul. Smoluchowskiego 17, 60-179 Poznań, Poland

STRESS AND DISPLACEMENT ANALYSIS OF AN AUXETIC QUARTER-PLANE UNDER A CONCENTRATED FORCE

PAWEŁ FRITZKOWSKI AND HENRYK KAMIŃSKI

The problem of a quarter-space under distributed normal and shear loads is considered. A mathematical model is formulated for the plane strain state. Theoretical background of the Mellin integral transform and calculation of residues is outlined. An analytical procedure involving the Mellin transform is presented for the general reduced problem of a quarter-plane. Numerical computation of residues allows for evaluation of the inverse transforms for the displacements and stresses. Simulation results are obtained for a special load case: a concentrated force. The deformation of the loaded boundary is analyzed for various values of Poisson's ratio. It turns out that auxetics exhibit locally negative stiffness, which leads to an anomalous behavior of the system. A simple explanation of the unusual deformation mechanism is proposed. The semianalytical solutions are compared with the results obtained by means of the finite element method.

1. Introduction

In the framework of the classical elasticity theory, a number of fundamental problems have been formulated in unbounded domains such as infinite or semi-infinite space. Prominent examples of this kind are the Boussinesq and the Cerruti problems: an elastic half-space under a normal or tangent concentrated force, respectively [Sadd 2005; Saada 1993; Nowacki 1970]. Usually the specific domain character enables one to apply certain analytical procedures like the complex variable method or the integral transform method (e.g., Laplace or Fourier transform), which can lead to closed-form solutions. Very often it requires considerable model simplifications, e.g., by using the plane stress or plane strain assumption. Nevertheless, such theoretical studies still provide significant information about more practical problems related to, among others, fracture and contact mechanics [Sadd 2005; Saada 1993; Timoshenko and Goodier 1951; Johnson 1985].

Nowadays, in the era of modern computational tools, mostly based on the finite element method, the classical elasticity problems and analytical approaches seem to be of less importance. However, they remain a helpful means of preliminary studies of unconventional systems whose anomalous behavior goes beyond the well-known theoretical solutions. One such example is auxetics, i.e., materials with negative Poisson's ratio, $\nu < 0$. Indeed, for decades scientists and researchers have been mainly focusing on traditional engineering materials for which usually $0.25 < \nu < 0.35$. But even today, despite numerous present and potential applications of auxetics (e.g., in aerospace, biomedical and military engineering), and constantly developed techniques for their manufacture [Prawoto 2012; Alderson and Alderson 2007], the behavior and mechanical properties of these materials are not intuitive. Therefore, the authors of

This work has been supported by grant 02/21/DSPB/3453.

Keywords: linear elasticity, quarter-plane, deformation, auxetic materials, Mellin transform.

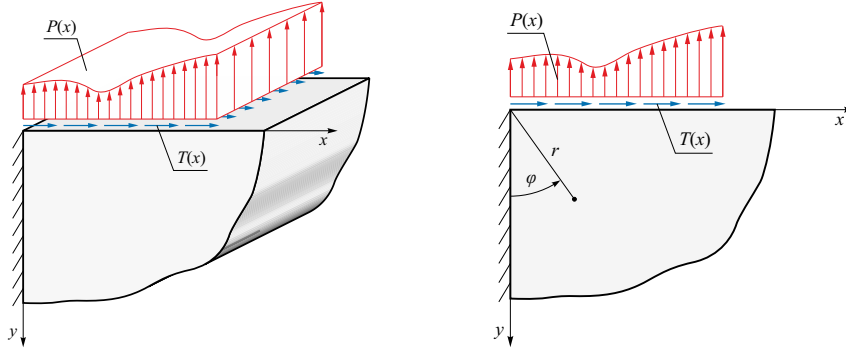


Figure 1. Elastic quarter-space with a loaded surface: (left) the primary, three-dimensional problem and (right) the reduced problem of a quarter-plane.

excellent review papers not only report auxetics-related advances in research and technology but also thoroughly discuss the concept and physical significance of Poisson's ratio [Greaves et al. 2011] as well as deformation mechanisms of auxetic systems [Evans and Alderson 2000; Prawoto 2012]. It should be noted that the classical theory of elasticity places the following bounds on Poisson's ratio of isotropic materials [Sadd 2005; Greaves et al. 2011]: $-1 < \nu < 1/2$.

This paper is devoted to stress and deformation analysis of an elastic solid quarter-space subjected to a line-distributed loading. Due to the plane strain state, the problem is reduced to a static analysis of a quarter-plane under a concentrated force. A semianalytical approach is used to solve the displacement field equations. More precisely, the Mellin transform technique is applied in combination with a numerical calculation of residues. The main aim of this work is to investigate the effect of Poisson's ratio on deformation of the loaded surface and report on an application of the Mellin transform that has been rather rarely employed in computational practice.

The paper is divided into six sections. In Section 2, a mathematical formulation of the problem is presented. Section 3 outlines the concept of the Mellin integral transform and computation of residues. In turn, a general solution procedure of the stated problem is specified in Section 4. Section 5 contains simulation results and discussion. Conclusions and final remarks are given in Section 6.

2. Formulation of the problem

Let us consider the generalized problem of an elastic quarter-space shown in Figure 1, left. The vertical boundary half-plane is fixed, while the horizontal one is free and subjected to distributed normal and shear loads: $P(x)$ and $T(x)$, respectively. The solid material occupying the domain is assumed to be homogeneous, isotropic and linear, and it is characterized by shear modulus G and Poisson's ratio ν . In the case of auxetics, $\nu < 0$.

Since the support and loading conditions are independent of the z coordinate, the spatial problem can be reduced to two dimensions (see Figure 1, right). Accordingly, the plane strain formulation is used below. Now, we focus on a quarter-plane, i.e., the region with semi-infinite boundaries:

$$\Omega = \begin{cases} 0 \leq x < \infty, \\ 0 \leq y < \infty. \end{cases} \quad (2-1)$$

It can be actually treated as a domain in the shape of a right-angle infinite wedge. Therefore, the mathematical model is formulated in a polar coordinate system (r, φ) .

Let $\mathbf{u}(r, \varphi) = [u_r, u_\varphi]^T$ be the displacement vector, where u_r and u_φ denote its radial and tangential components. The strain-displacement relations involving only the in-plane strains have the forms

$$\varepsilon_r = \frac{\partial u_r}{\partial r}, \quad \varepsilon_\varphi = \frac{1}{r} \left(u_r + \frac{\partial u_\varphi}{\partial \varphi} \right), \quad \varepsilon_{r\varphi} = \frac{1}{2} \left(\frac{1}{r} \frac{\partial u_r}{\partial \varphi} + \frac{\partial u_\varphi}{\partial r} - \frac{u_\varphi}{r} \right). \quad (2-2)$$

From Hooke's law, the corresponding stress components are given by

$$\sigma_r = \lambda(\varepsilon_r + \varepsilon_\varphi) + 2\mu\varepsilon_r, \quad \sigma_\varphi = \lambda(\varepsilon_r + \varepsilon_\varphi) + 2\mu\varepsilon_\varphi, \quad \sigma_{r\varphi} = 2\mu\varepsilon_{r\varphi}, \quad (2-3)$$

where λ and μ are Lamé constants:

$$\lambda = \frac{2G\nu}{1-2\nu}, \quad \mu = G. \quad (2-4)$$

Finally, in the case of zero body forces, the Navier–Lamé equations reduce to [Nowacki 1970; Sadd 2005]

$$\mu \left(\nabla^2 u_r - \frac{u_r}{r^2} - \frac{2}{r^2} \frac{\partial u_\varphi}{\partial \varphi} \right) + (\lambda + \mu) \frac{\partial}{\partial r} \left(\frac{1}{r} \frac{\partial}{\partial r} (r u_r) + \frac{1}{r} \frac{\partial u_\varphi}{\partial \varphi} (r u_r) \right) = 0, \quad (2-5a)$$

$$\mu \left(\nabla^2 u_\varphi - \frac{u_\varphi}{r^2} - \frac{2}{r^2} \frac{\partial u_r}{\partial \varphi} \right) + (\lambda + \mu) \frac{1}{r} \frac{\partial}{\partial \varphi} \left(\frac{1}{r} \frac{\partial}{\partial r} (r u_r) + \frac{1}{r} \frac{\partial u_\varphi}{\partial \varphi} (r u_r) \right) = 0. \quad (2-5b)$$

Moreover, for the given quarter-plane problem, the unknown vector-valued function $\mathbf{u}(r, \varphi)$ must satisfy the following mixed boundary conditions:

$$u_r(r, 0) = u_\varphi(r, 0) = 0 \quad (\text{displacement conditions}), \quad (2-6a)$$

$$\sigma_\varphi(r, \pi/2) = P(r) \quad (\text{traction condition}), \quad (2-6b)$$

$$\sigma_{r\varphi}(r, \pi/2) = T(r) \quad (\text{traction condition}). \quad (2-6c)$$

Thus, the resulting mathematical model consists of the system of coupled partial differential equations (2-5) together with four boundary conditions (2-6).

The boundary value problem is not of a simple nature. To solve it analytically, we apply operational calculus with the Mellin transformation method. Owing to the fact that this mathematical tool is less commonly used than other integral transforms (e.g., the Fourier or Laplace transforms), basic theoretical concepts are outlined in the next section.

3. Mathematical background

In literature one can find a few applications of the classical Mellin transform to plane elasticity problems. Sneddon [1951] considered an infinite elastic wedge subjected to surface stresses. Consequently, the author used the stress formulation and an Airy stress function. A similar approach for a finite wedge was employed by Tsamasphyros and Theocaris [1979]. They obtained the stress function as an asymptotic expansion of the complex inversion integral. More recently, Martin [2003] analyzed the problem of a composite elastic half-plane, made from two isotropic quarter-planes, subjected to a concentrated force. An exact solution was constructed using Mellin transforms and the Melan solution for a homogeneous

half-plane. Moreover, the Mellin transform was applied to some fracture and contact problems for wedge-shaped domains; see, e.g., [Erdogan and Arin 1976; Theocaris and Makrakis 1987]. In these cases, understandably, the stress formulation was preferable too.

The information given below is a concise selection from many handbooks devoted to both mathematical theory and applications. The interested reader is referred especially to [Kącki 1992; Bateman 1954; Debnath and Bhatta 2007].

Let $f(x)$ be a function of a real variable x . The Mellin integral transform of f is defined by

$$\tilde{f}(s) = \int_0^{\infty} f(x)x^{s-1} dx, \quad (3-1)$$

where s is a complex variable. In further considerations, the transform will be denoted symbolically by

$$\tilde{f}(s) = \mathcal{M}[f(x)]. \quad (3-2)$$

The inverse Mellin transform, in turn, is defined formally as

$$f(x) = \mathcal{M}^{-1}[\tilde{f}(s)] = \frac{1}{2\pi i} \int_{c-i\infty}^{c+i\infty} \tilde{f}(s)x^{-s} ds, \quad (3-3)$$

where i is the imaginary unit and c lies on the complex plane in the strip of analyticity of the function $\tilde{f}(s)$.

Additionally, for further purposes, two operational properties of the Mellin transform are listed below:

- Suppose that $\tilde{f}(s)$ is defined by (3-2) and there exists the Mellin transform of

$$g(x) = \left(x \frac{d}{dx}\right)^n f(x). \quad (3-4)$$

Then

$$\mathcal{M}[g(x)] = (-s)^n \tilde{f}(s). \quad (3-5)$$

- Let $f(x, y)$ be a function of two variables. If

$$\mathcal{M}_x[f(x, y)] = \tilde{f}(s, y) \quad (3-6)$$

is the Mellin transform of f with respect to x , then

$$\mathcal{M}_x \left[\frac{\partial^n f(x, y)}{\partial y^n} \right] = \frac{\partial^n \tilde{f}(s, y)}{\partial y^n}. \quad (3-7)$$

Suppose that $f(x)$ is an unknown solution of a given problem. Moreover, let $g(s) = \tilde{f}(s)$ be its Mellin transform, i.e., the solution of the problem transformed by means of the direct transformation. Obviously, the inverse Mellin transform is used to recover f from g . In practice, the complex integral (3-3) can be calculated by applying Cauchy's residue theorem. Accordingly, if D is a region bounded by a simple closed contour C and $g(s)$ is analytic in D , except for a finite number of isolated singularities at s_1, s_2, \dots, s_n , then the counterclockwise contour integral

$$\oint_C g(s) ds = 2\pi i \sum_{k=1}^n \text{Res}[g(s), s_k], \quad (3-8)$$

where $\text{Res}[g(s), s_k]$ denotes the residue of $g(s)$ at s_k [Bronsztejn et al. 2009; Kaplan 2002].

As can be seen, calculating residues of the direct transform is crucial to an efficient evaluation of the inverse transform. In particular, the following rule is indispensable in computational practice: if $g(s)$ is a function of the form

$$g(s) = \frac{p(s)}{q(s)} \quad (3-9)$$

and it has a pole of first order at s_0 , then

$$\text{Res}[g(s), s_0] = \frac{p(s_0)}{q'(s_0)}. \quad (3-10)$$

The outlined Mellin transform method together with a numerical computation of residues allow for a semianalytical treatment of the quarter-plane problem, which is discussed in the next sections.

4. General analytical procedure

4A. Transformation of the problem. Let \tilde{u}_r and \tilde{u}_φ denote the Mellin transforms of the displacements with respect to the polar coordinate r , that is,

$$\tilde{u}_r(s, \varphi) = \mathcal{M}_r[u_r(r, \varphi)], \quad \tilde{u}_\varphi(s, \varphi) = \mathcal{M}_r[u_\varphi(r, \varphi)]. \quad (4-1)$$

Multiplying the governing equations (2-5) by r^2 and using the properties (3-5) and (3-7) yields the following transformed pair:

$$\mu \frac{\partial^2 \tilde{u}_r}{\partial \varphi^2} + (\lambda + 2\mu)(s^2 - 1)\tilde{u}_r - [s(\lambda + \mu) + (\lambda + 3\mu)] \frac{\partial \tilde{u}_\varphi}{\partial \varphi} = 0, \quad (4-2a)$$

$$(\lambda + 2\mu) \frac{\partial^2 \tilde{u}_\varphi}{\partial \varphi^2} + \mu(s^2 - 1)\tilde{u}_\varphi - [s(\lambda + \mu) - (\lambda + 3\mu)] \frac{\partial \tilde{u}_r}{\partial \varphi} = 0. \quad (4-2b)$$

It should be noted that these equations are much simpler than the original ones.

Next, consider the stress-displacement relations that can be obtained by inserting (2-2) into (2-3). Transformations of the stress components multiplied by r

$$\tilde{t}_r(s, \varphi) = \mathcal{M}_r[r\sigma_r(r, \varphi)],$$

$$\tilde{t}_\varphi(s, \varphi) = \mathcal{M}_r[r\sigma_\varphi(r, \varphi)],$$

$$\tilde{t}_{r\varphi}(s, \varphi) = \mathcal{M}_r[r\sigma_{r\varphi}(r, \varphi)]$$

become

$$\tilde{t}_r(s, \varphi) = [\lambda - s(\lambda + 2\mu)]\tilde{u}_r + \lambda \frac{\partial \tilde{u}_\varphi}{\partial \varphi}, \quad (4-3a)$$

$$\tilde{t}_\varphi(s, \varphi) = [(\lambda + 2\mu) - s\lambda]\tilde{u}_r + (\lambda + 2\mu) \frac{\partial \tilde{u}_\varphi}{\partial \varphi}, \quad (4-3b)$$

$$\tilde{t}_{r\varphi}(s, \varphi) = \mu \left[-(s + 1)\tilde{u}_\varphi + \frac{\partial \tilde{u}_r}{\partial \varphi} \right]. \quad (4-3c)$$

Now, boundary conditions (2-6) can be converted to

$$\tilde{u}_r(s, 0) = \tilde{u}_\varphi(s, 0) = 0 \quad (\text{displacement conditions}), \quad (4-4a)$$

$$\tilde{i}_\varphi(s, \pi/2) = \tilde{P}(s) \quad (\text{traction condition}), \quad (4-4b)$$

$$\tilde{i}_{r\varphi}(s, \pi/2) = \tilde{T}(s) \quad (\text{traction condition}), \quad (4-4c)$$

where

$$\tilde{T}(s) = \mathcal{M}_r[rT(r)], \quad \tilde{P}(s) = \mathcal{M}_r[rP(r)]. \quad (4-5)$$

To sum up, after the transformation the boundary value problem comprises the equilibrium equations (4-2) and associated boundary conditions (4-4).

4B. Solution of the problem. Due to its relatively simple form, the transformed problem can be solved in a quite conventional way. For the second-order partial differential equations (4-2), one can suppose that

$$\tilde{u}_r(s, \varphi) = C_1 e^{h\varphi}, \quad \tilde{u}_\varphi(s, \varphi) = C_2 e^{h\varphi}, \quad (4-6)$$

where C_1 and C_2 are real constants, while h is a complex parameter to be determined. Inserting (4-6) into (4-2) leads to a system of two characteristic equations. All their roots are complex:

$$h_1 = i(s+1), \quad h_2 = -i(s+1), \quad h_3 = i(s-1), \quad h_4 = -i(s-1).$$

Hence, the solution is given by

$$\tilde{u}_r(s, \varphi) = A_{11} \sin[(s+1)\varphi] + B_{11} \cos[(s+1)\varphi] + A_{12} \sin[(s-1)\varphi] + B_{12} \cos[(s-1)\varphi], \quad (4-7a)$$

$$\tilde{u}_\varphi(s, \varphi) = A_{21} \sin[(s+1)\varphi] + B_{21} \cos[(s+1)\varphi] + A_{22} \sin[(s-1)\varphi] + B_{22} \cos[(s-1)\varphi], \quad (4-7b)$$

where $A_{11}, B_{11}, A_{12}, \dots, A_{22}$ are real constants. As can be ascertained by substitution, in order to satisfy (4-2), the relations

$$A_{21} = B_{11} \frac{\eta_1 s - \eta_3}{\eta_1 s + \eta_3}, \quad A_{22} = B_{12}, \quad B_{21} = -A_{11} \frac{\eta_1 s - \eta_3}{\eta_1 s + \eta_3}, \quad B_{22} = -A_{12} \quad (4-8)$$

must be fulfilled, where auxiliary parameters are introduced for notational brevity:

$$\eta_j = \lambda + j\mu, \quad j = 1, 2, 3.$$

The next four constants can be determined from the prescribed boundary conditions. Taking into consideration (4-4a) produces

$$B_{12} = -B_{11}, \quad A_{12} = -A_{11} \frac{\eta_1 s - \eta_3}{\eta_1 s + \eta_3}. \quad (4-9)$$

Similarly, the traction conditions (4-4b) and (4-4c) require

$$A_{11} = -\frac{\tilde{T}(\eta_1 s + \eta_3) + 4B_{11}\mu s(\eta_1 s + \eta_2) \cos(\frac{1}{2}\pi s)}{4\mu s(\eta_1 s - \mu) \sin(\frac{1}{2}\pi s)}, \quad (4-10)$$

$$B_{11} = -\frac{(\eta_1 s + \eta_3)[\tilde{P}(\eta_1 s - \mu) \sin(\frac{1}{2}\pi s) + \tilde{T}(\eta_1 s + \eta_2) \cos(\frac{1}{2}\pi s)]}{2\mu s[2(\eta_1^2 s^2 - \mu^2) - \eta_1 \eta_3 \cos(\pi s) - \eta_1 \eta_3]}.$$

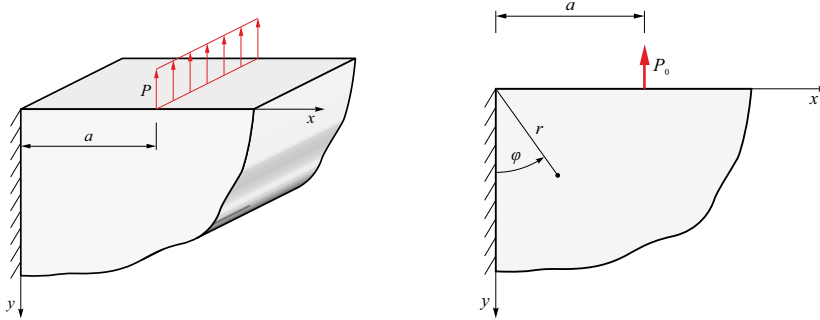


Figure 2. Elastic quarter-space with line-distributed loading: (left) the primary, three-dimensional problem and (right) the reduced problem of a quarter-plane under a concentrated force.

Using all the relationships (4-8), (4-9) and (4-10), one can find expressions for the Mellin transforms of the desired displacement, strain and stress components. They are not presented here because of their considerable complexity. Instead, we concentrate on displacements related to the loaded boundary:

$$\tilde{u}_r(s, \pi/2) = \frac{\tilde{T}}{2Gq(s)} \kappa(\kappa + 1) \sin(\pi s) - \frac{\tilde{P}}{2Gq(s)} [4s^2 + 2(\kappa + 1)s + \kappa(\kappa - 1)(\cos(\pi s) - 1)], \quad (4-11a)$$

$$\tilde{u}_\varphi(s, \pi/2) = \frac{\tilde{P}}{2Gq(s)} \kappa(\kappa + 1) \sin(\pi s) + \frac{\tilde{T}}{2Gq(s)} [4s^2 - 2(\kappa + 1)s + \kappa(\kappa - 1)(\cos(\pi s) - 1)], \quad (4-11b)$$

where κ denotes the Kolosov constant

$$\kappa = 3 - 4\nu \quad (4-12)$$

and the common variable part of the denominators is

$$q(s) = s[1 - 4s^2 + \kappa^2 + 2\kappa \cos(\pi s)]. \quad (4-13)$$

For a certain load case, the obtained formulas can be subjected to the inverse Mellin transform performed numerically, which leads to displacement values u_r and u_φ .

5. Case study and results

5A. Analytical results. Consider the specific problem indicated in the title. The original problem relates to an elastic quarter-space with a line load that is applied at a distance a from the z axis (see Figure 2, left). Consequently, in the plain strain formulation, the horizontal edge of the quarter-plane is loaded by a concentrated force P_0 . Thus,

$$P(r) = P_0 \delta(r - a), \quad T(r) = 0,$$

where δ denotes the Dirac delta. Then the boundary conditions (2-6) become

$$u_r(r, 0) = u_\varphi(r, 0) = 0 \quad (\text{displacement conditions}), \quad (5-1a)$$

$$\sigma_\varphi(r, \pi/2) = P_0 \delta(r - a) \quad (\text{traction condition}), \quad (5-1b)$$

$$\sigma_{r\varphi}(r, \pi/2) = 0 \quad (\text{traction condition}). \quad (5-1c)$$

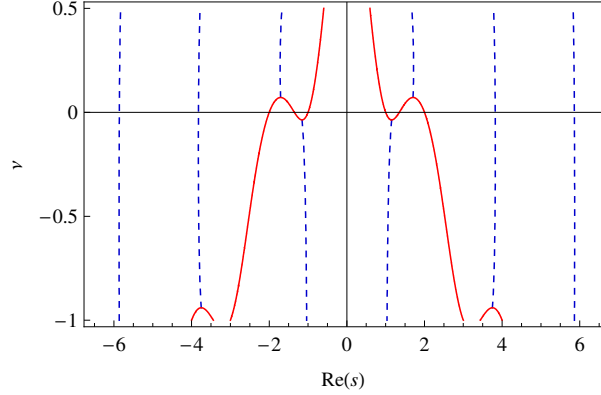


Figure 3. Values of the real parts of poles versus Poisson's ratio: real poles (solid) and initial complex poles (dashed).

The nonhomogeneous traction condition can be easily transformed by using the so-called sifting property of the Dirac delta:

$$\tilde{P}(s) = \int_0^\infty r P(r) r^{s-1} dr = \int_0^\infty r^s P_0 \delta(r-a) dr = P_0 a^s.$$

Taking into account that $\tilde{T}(s) = 0$, the complete set of transformed conditions (4-4) is given by

$$\tilde{u}_r(s, 0) = \tilde{u}_\varphi(s, 0) = 0 \quad (\text{displacement conditions}), \quad (5-2a)$$

$$\tilde{t}_\varphi(s, \pi/2) = P_0 a^s \quad (\text{traction condition}), \quad (5-2b)$$

$$\tilde{t}_{r\varphi}(s, \pi/2) = 0 \quad (\text{traction condition}). \quad (5-2c)$$

By analogy to the general case, we present only the Mellin transforms of displacements of the loaded surface. Equations (4-11) become

$$\tilde{u}_r(s, \pi/2) = -\frac{P_0 a^s}{2Gq(s)} [4s^2 + 2(\kappa + 1)s + \kappa(\kappa - 1)(\cos(\pi s) - 1)], \quad (5-3a)$$

$$\tilde{u}_\varphi(s, \pi/2) = \frac{P_0 a^s}{2Gq(s)} \kappa(\kappa + 1) \sin(\pi s). \quad (5-3b)$$

Expressions for \tilde{t}_r , \tilde{t}_φ and $\tilde{t}_{r\varphi}$ are much more complex; however, they also include the denominator $q(s)$.

5B. Some computational issues. As suggested in Section 3, the inversion process can be performed via numerical evaluation of residues. This approach requires finding poles of the given Mellin transforms multiplied by r^{-s} . Since the integrands of the inversion integral (3-3) can be written in the form (3-9), the function $q(s)$ plays a key role. In fact, the solutions of the transcendental equation $q(s) = 0$ must be found.

It can be easily shown that the integrands do not have poles at $s = 0$, whereas the other zeros of $q(s)$ correspond to the poles of first order. Their location in the complex plane is symmetric with respect to both axes. Figure 3 shows values of the real parts of a few initial poles, calculated for the whole range $-1 \leq \nu \leq 1/2$. There is a finite number $2n_r$ of real poles, all of which lie near the origin ($1 \leq n_r \leq 3$). Moreover, there are infinitely many complex conjugate poles ($n_c = \infty$).

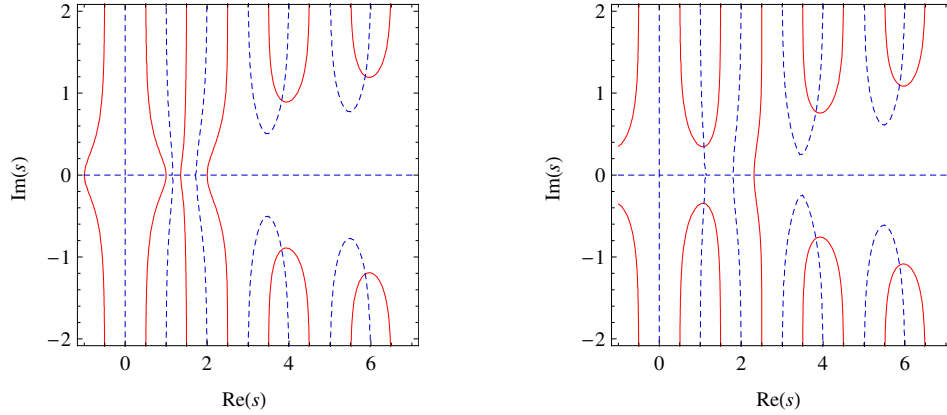


Figure 4. Zero-level contour lines of the real part (solid) and the imaginary part (dashed) of $q(s)$: (left) $\nu = 0$ and (right) $\nu = -0.25$. The intersections of different contours indicate poles' loci.

Achieving a good insight into the pattern of singularities' locations is essential to construct an algorithm for evaluation of residues. Due to the mentioned symmetry, we concentrate on the right half-plane. In Figure 4 two isoline plots are presented for $\nu = 0$ and $\nu = -0.25$. They display just the zero-level contours of the real and imaginary parts of the function $q(s)$. Thus, a real pole $s_{rk} = \alpha_{rk}$ ($k = 1, 2, \dots, n_r$) of $p(s)/q(s)$ is indicated by the intersection of a real-part-related contour with the real axis. A complex pole $s_{ck} = \alpha_{ck} + \beta_{ck}i$ ($k = 1, 2, \dots, n_c$), in turn, lies at the intersection of two contours of different types and has a corresponding conjugate, $\bar{s}_{ck} = \alpha_{ck} - \beta_{ck}i$. As $\nu = 0$, for example, in the right half-plane three real poles s_{r1} , s_{r2} and s_{r3} are followed by all the complex poles s_{ck} and \bar{s}_{ck} ($k = 1, 2, \dots, n_c$). For the other case, in turn, a single real pole s_{r1} is located between the first and second complex conjugate pairs, s_{c1} , \bar{s}_{c1} and s_{c2} , \bar{s}_{c2} . Generally, the difference between the real parts of two directly neighboring complex poles $\Delta\alpha_c = \alpha_{c_{k+1}} - \alpha_{ck} \approx 2$, whereas the imaginary difference decreases exponentially to zero ($\Delta\beta_c \rightarrow 0$).

Although there is an infinite number of isolated complex singularities, residue values gradually decrease with increasing absolute value of the real part α_{ck} . Consequently, the true solution can be well-approximated by a finite (truncated) sum of residues of the direct transforms. The degree of accuracy of this approximation is affected by two factors. Firstly, one should reasonably select the number n_c^* of the complex poles being taken. Secondly, the numerical solution of $q(s) = 0$ plays a vital role. In our simulations the real roots are found with the use of Muller's method. The complex roots, in turn, are obtained by a consecutive application of the method of successive approximations (a fixed-point iteration scheme).

In practice, calculation of the so-called Bromwich integral (3-3) may seem a bit enigmatic. The integration must be performed along an infinite line L that is parallel to the imaginary axis ($\text{Re}(s) = c$). In the given problem, two lines, L_1 and L_2 , are used as illustrated in Figure 5. Thus, $c_1 = c$ and $c_2 = -c$ where c is a small positive value so that $c < s_{r1}$ as well as $c < \text{Re}(s_{c1})$. Additionally, two half-circles of radius R , Γ_1 and Γ_2 , are chosen as the completion paths. For $R \rightarrow \infty$ the lines and curves constitute closed contours, $C_1 = L_1 \cup \Gamma_1$ and $C_2 = L_2 \cup \Gamma_2$, which enclose all the poles in the right and left complex half-planes, respectively. Convergence of the computation can be ensured by the proper choice of the inversion contour.

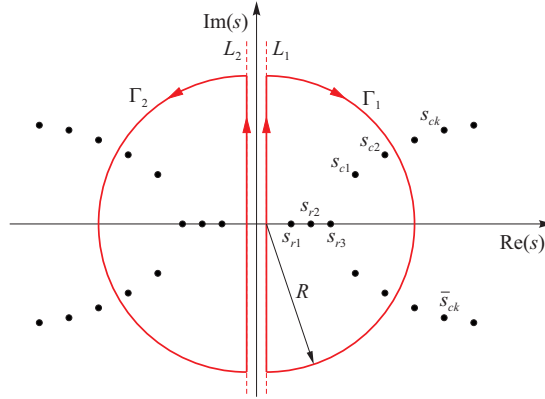


Figure 5. Two alternative inversion contours to use in the Bromwich integral.

Generally, the Mellin transforms of the displacements, $\tilde{u}_r(s, \varphi)$ and $\tilde{u}_\varphi(s, \varphi)$, have the form $\tilde{f}(s, \varphi) = p(s, \varphi)/q(s, \varphi)$. The integrands for the inversion formula (3-3), in turn, are given by

$$\tilde{f}(s, \varphi)r^{-s} = \left(\frac{r}{a}\right)^{-s} \frac{p^*(s, \varphi)}{q(s, \varphi)}. \quad (5-4)$$

It can be shown that the behavior of these functions is determined by the factor $(r/a)^{-s}$. For $r \geq a$ the functions tend to zero if $\text{Re}(s) \rightarrow +\infty$. Thus, the integral of (5-4) along the curve Γ_1 vanishes in the limit for $R \rightarrow \infty$, and the Bromwich integral can be evaluated by means of the contour C_1 . In the other case, when $r < a$, the integrands tend to zero if $\text{Re}(s) \rightarrow -\infty$. Consequently, the contour C_2 is used for the inversion integral since the integral along the curve Γ_2 vanishes for $R \rightarrow \infty$. In both cases, the integration is performed by summing up the residues enclosed by C_1 or C_2 .

5C. Simulation results. Although an immanent feature of numerical calculations is that they are performed for specific values of model parameters, the results reported below have a nondimensional form. More precisely, the dimensionless displacements are defined as

$$U_x(x, y) = \frac{Ga}{P_0} u_x(x, y) \times 10^6, \quad U_y(x, y) = \frac{Ga}{P_0} u_y(x, y) \times 10^6. \quad (5-5)$$

The polar components, $U_r(r, \varphi)$ and $U_\varphi(r, \varphi)$, are computed in the same way. Analogously, the following nondimensional stresses are introduced:

$$S_x(x, y) = \frac{a}{P_0} \sigma_x(x, y), \quad S_y(x, y) = \frac{a}{P_0} \sigma_y(x, y), \quad S_{xy}(x, y) = \frac{a}{P_0} \sigma_{xy}(x, y). \quad (5-6)$$

Let us start with an overall look at the displacement and stress fields. Figure 6 shows the distribution of the vertical displacement U_y , normal stress S_y and shear stress S_{xy} in a rectangular subregion of the quarter-plane, $\langle 0, 2a \rangle \times \langle 0, a \rangle$, for two values of Poisson's ratio: $\nu = 0.25$ and $\nu = -0.5$. Generally, in both cases the distributions are qualitatively similar, and far away from the fixed boundary, their nature resembles the results for an elastic half-plane (see, e.g., [Sadd 2005; Saada 1993]). The effects of the concentrated force are highly localized. The displacement U_y decreases radially outward from the point of application of the load. The contours of constant tensile stress S_y form closed curves converging at

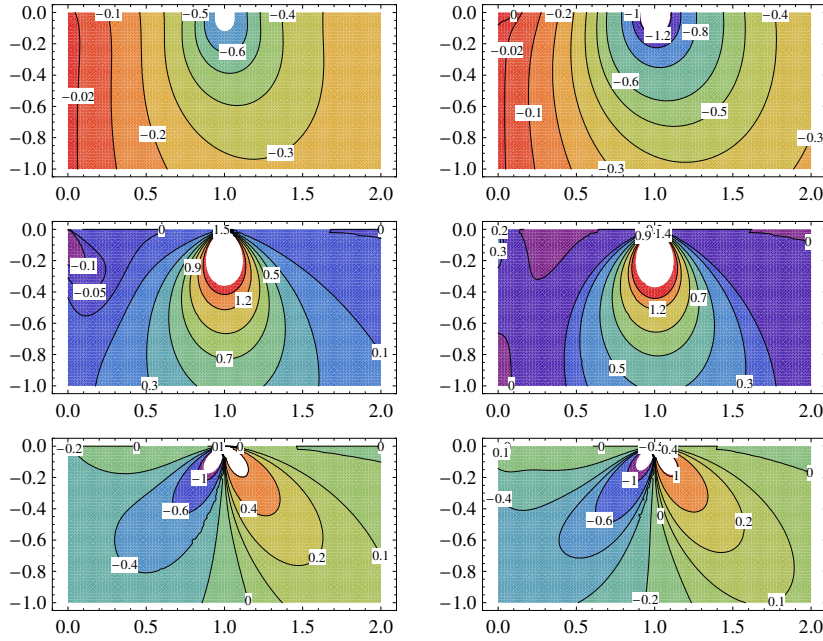


Figure 6. Displacement and stress distributions in a rectangular region for $\nu = 0.25$ (left column) and $\nu = -0.5$ (right column): (top) vertical displacement U_y , (middle) normal stress S_y and (bottom) shear stress S_{xy} . Results obtained for $n_c^* = 5 \times 10^3$.

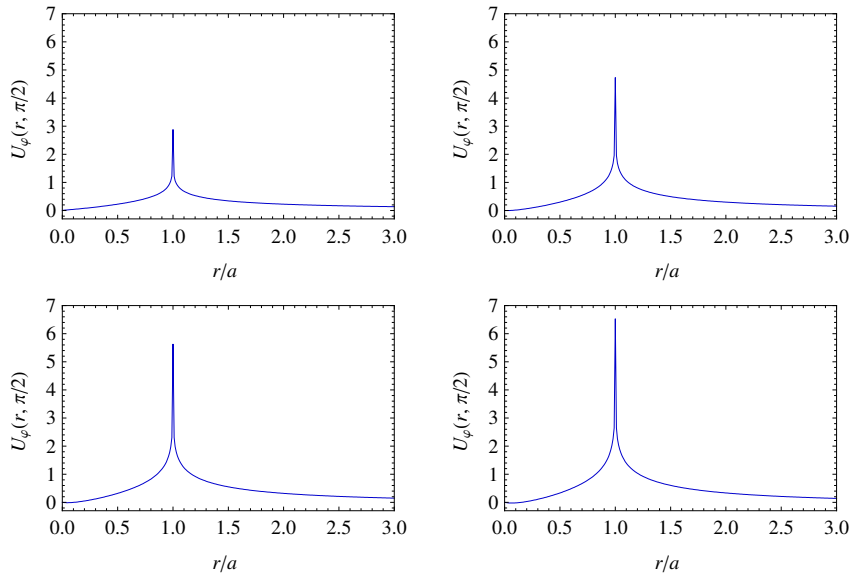


Figure 7. Vertical displacement of the loaded surface for various values of Poisson's ratio: (top left) $\nu = 0.25$, (top right) $\nu = -0.25$, (bottom left) $\nu = -0.5$ and (bottom right) $\nu = -0.75$. Results obtained for $n_c^* = 3 \times 10^4$.

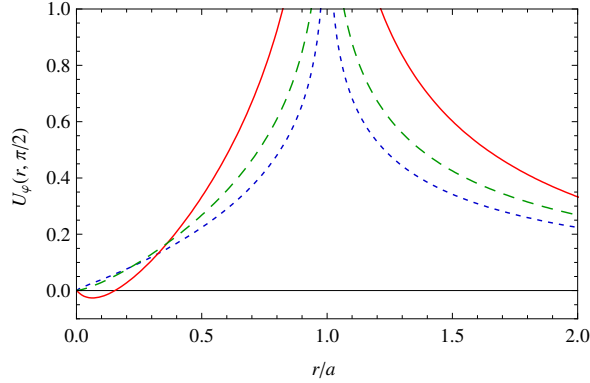


Figure 8. The effect of the anomalous vertical displacement of the loaded surface for negative Poisson's ratio: $\nu = -0.75$ (solid), $\nu = 0$ (dashed) and $\nu = 0.25$ (dotted).

this point. In this sense they bring to mind the isochromatic photoelastic fringe patterns (isolines of the principal shear stress) for a point load, well-known from contact mechanics [Sadd 2005; Johnson 1985]. The shear stress field indicates that below the free surface, for example at the level $y_1 = a/10$, a change in sign of $S_{xy}(x, y_1)$ occurs at $x = a$ (compare the classical Flamant problem [Sadd 2005]). The stress becomes vanishingly small at a sufficiently large distance from this point. Obviously, due to the constraints, the general view is disturbed by some local effects near the fixed boundary, which is discussed later.

Now let us turn to a displacement analysis of the loaded surface. In Figure 7 the vertical displacement $U_\varphi(r, \pi/2) = -U_y(x, 0)$ is presented for various values of Poisson's ratio. For ease of comparison, all the plots have equal axis scales. As can be seen, values of the sharp peak at the loading point grow with decreasingly lower ν . The deformation behavior is intuitively reasonable and seems qualitatively identical in each case. However, a closer look at the curves allows one to notice an interesting detail. If $\nu > 0$ the vertical displacement component of every point on the boundary is directed upward, i.e., has the same direction as the active force. But for the auxetic case, $\nu < 0$, a strict minimum of the function $U_\varphi(r, \pi/2)$ arises in the range $0 < r < a$: the edge deflects locally in the opposite direction to the load. This unusual valley effect can be clearly observed in Figure 8. Zero Poisson's ratio seems to be the intermediate case, when the deflection curve is tangent to the horizontal axis at $r = 0$.

Figure 9 shows how Poisson's ratio affects the zero locus x_0 of the function $-U_y(x, 0)$. Evidently, the distance between the zero-crossing and the origin increases as ν tends to -1 . In the opposite case, when $\nu = 0$, the two points overlap, i.e., there is no additional minimum for $x > 0$. Thus, $\nu = 0$ can be treated as the critical value, ν_{cr} , below which the valley effect always occurs; the effect intensifies with stronger auxetic behavior exhibited by the material.

In general, mutually opposite directions of the active force and the resulting displacement contradict practical experience. This property is referred to as negative stiffness and should be distinguished from negative Poisson's ratio. However, systems with such an anomaly exist not only in theory. Experimental realization of composite materials with negative stiffness has been discussed, for example, in [Lakes et al. 2001; Lakes 2001].

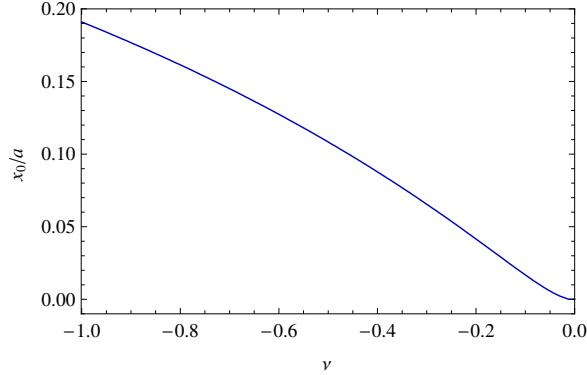


Figure 9. Locus of the zero of $U_\varphi(r, \pi/2)$ versus Poisson's ratio.

In [Maruszewski et al. 2010; Poźniak et al. 2010] it is suggested that the unusual deformation found in our simulations may be treated as locally negative compliance. The authors numerically investigated similar behavior of simple two- or three-dimensional systems. In the planar case, they considered a unit square domain whose two opposite sides are fixed, whereas the others are subjected to uniform compression loading. The elastostatic problem was solved under the plane stress assumption by using the finite element method (FEM). The results indicate counterintuitive deformation of the square near its vertices for negative Poisson's ratio. Nevertheless, the papers do not contain the definite conclusion that $\nu = 0$ is the critical value for occurrence of this effect. With the FEM approach, the evaluated ν_{cr} strongly depends on the mesh density. Analyzing the result convergence, the authors stated that $\nu_{cr} \geq -0.25$ [Poźniak et al. 2010] or $\nu_{cr} \geq -0.2$ [Maruszewski et al. 2010].

Finally, the question about the mechanism of the anomalous deformation arises. The contour plots shown in Figure 10 refer to a smaller fragment of the quarter-plane: $\langle 0, a \rangle \times \langle 0, a \rangle$. In the left-hand column the distribution of the stress S_y is presented more clearly than before. The right-hand plots, in turn, display isolines of the first (maximum) principal strain ε_1 , which is scaled according to

$$E_1 = 2(1 + \nu)G \frac{a^2}{P_0} \varepsilon_1. \quad (5-7)$$

For various values of ν both the fields have quite similar character in the area below the load. The most significant differences appear at the fixed edge, near the origin.

When it comes to the normal stress S_y , there is an evident change in sign due to a decrease of Poisson's ratio. The corner of compressive stress (for $\nu = 0.25$) becomes a neutral zone ($S_y = 0$) with a closed area of low compression (for $\nu = 0$) and is eventually transformed into a corner of tensile stress and a wedge neutral zone at the free surface (for $\nu = -0.5$). In the latter case one should notice the specific saddle-shaped arrangement of the near zero-level contours.

This gradual transformation of the normal stress, among others, entails an essential change in the maximum principal strain E_1 . As $\nu > 0$, the material undergoes elongation just under the free surface, which results mainly from the pulling force and the counterdirected reaction. For the critical value, $\nu = 0$, the strain E_1 is close to zero at the boundary but still nonnegative in the area below. As $\nu < 0$, however,

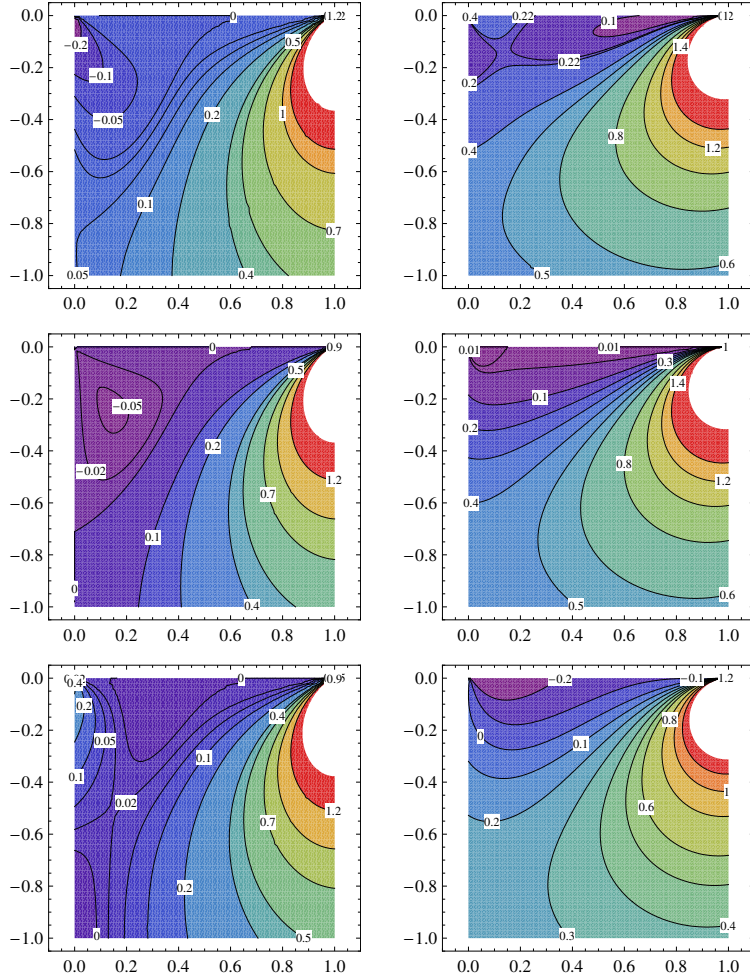


Figure 10. Stress and strain distribution in a square region. Normal stress S_y (left column) and the first principal strain E_1 (right column): (top) $\nu = 0.25$, (middle) $\nu = 0$ and (bottom) $\nu = -0.5$.

the maximum strain here becomes negative, and the isolines form a valley that strictly corresponds to the anomalous deformation of the loaded surface.

These differences arising when ν is varied may be basically explained by the example of a finite-sized elastic solid under uniaxial tensile load. First, consider the unconstrained case illustrated in Figure 11, left. Typically for conventional (nonauxetic) materials, elongation is accompanied by transverse contraction (see Figure 11, middle). Auxetics, by contrast, expand laterally in the same conditions (see Figure 11, right). Now, suppose that geometric constraints (fixed support) are imposed on the left side of the square. In the normal case ($\nu > 0$), the contraction of the solid generally produces a pulling horizontal (leftward) reaction force. Near the top-left corner, the displacement tendency of the vertex causes a slight pushing (rightward) reaction. As an overall result, the tension zone appears under the free surface. In the auxetic case, in turn, the lateral expansion must generate a pushing (rightward) reaction. The high horizontal

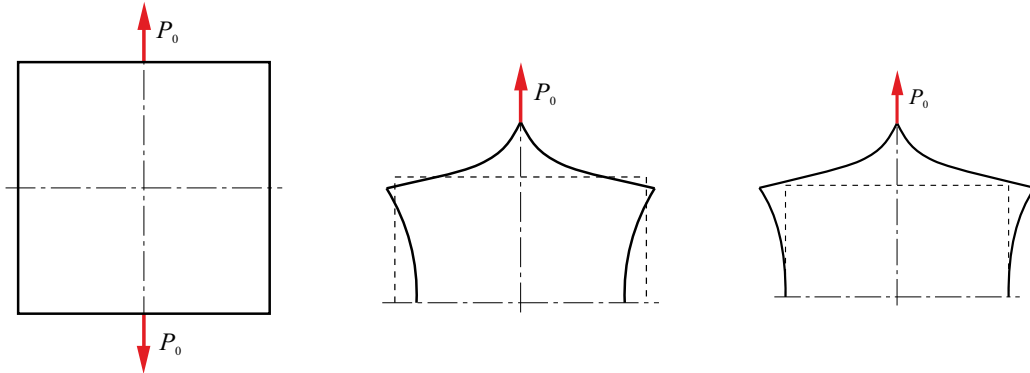


Figure 11. Deformation of an unconstrained elastic square under a tensile point load: (left) initial geometry and loading, (middle) deformation scheme in an ordinary, nonauxetic case and (right) deformation scheme in an auxetic case.

compression at the corner may lead to a local contraction in the transverse (vertical) direction, which manifests itself by the valley effect.

Despite its simplicity and schematic nature, the above explanation casts some light on the mechanism of the anomalous deformation of the quarter-plane. To some degree, the expansion-contraction behavior of the conventional and auxetic materials is reflected in the streamline patterns for the displacement field in the system (see Figure 12).

5D. Comparison to FEM results. Usually approximate methods are tested and validated by comparing their results to exact solutions. However, another well-established computer method also can be a source of the reference data. Very often the finite element method is employed for this purpose as one of the dominant tools applied in various fields of science and engineering. For instance, FEM results were used to test efficiency of mesh-based and meshless techniques in [Walczak et al. 2014; Bai and Lu 2004; Liu 2010]. Similar comparative study is carried out below for the semianalytical approach. All the presented results have been obtained using the COMSOL Multiphysics environment.

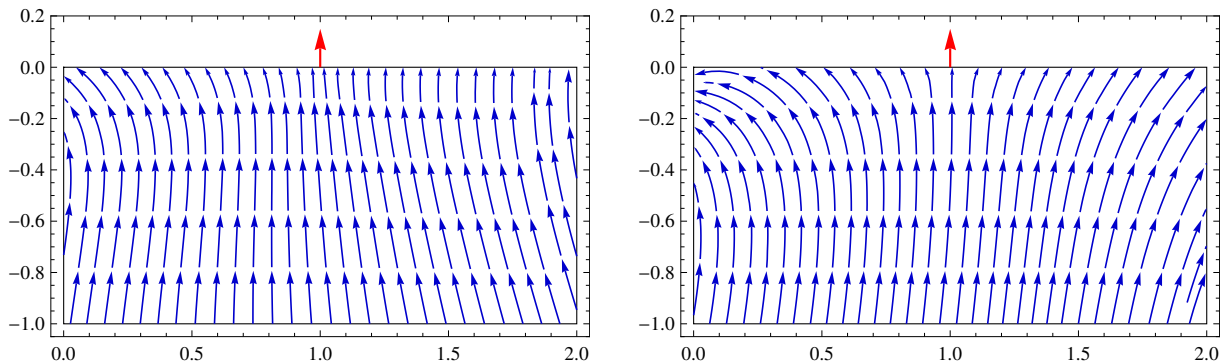


Figure 12. Streamline patterns for the displacement field: (left) $\nu = 0.25$ and (right) $\nu = -0.5$.

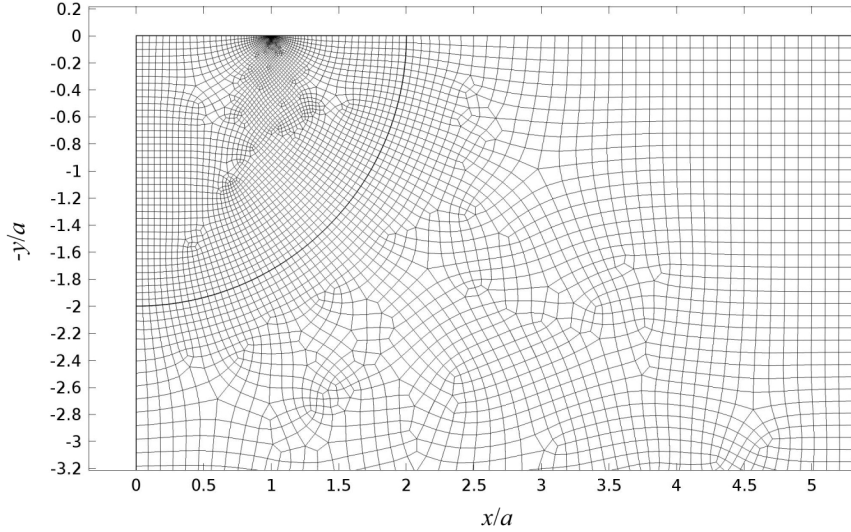


Figure 13. Finite element mesh near the loading point (a clipped view).

Some commercial FEM systems offer various implementations of infinite elements, which allows one to model unbounded domains. However, we decided to restrict the linear static analysis to a finite-sized square solid:

$$\widehat{\Omega} = \begin{cases} 0 \leq x \leq b, \\ 0 \leq y \leq b, \end{cases} \quad (5-8)$$

where $b > a$. Apart from the boundary conditions (5-1) reformulated in the Cartesian coordinate system, the following ones are imposed on the right and bottom edges:

$$u_x(b, y) = 0 \quad (\text{displacement condition}), \quad (5-9a)$$

$$u_y(x, b) = 0 \quad (\text{displacement condition}). \quad (5-9b)$$

It is assumed that $b = 10a$ to reduce the effect of the boundaries on the elastic field near the loading point. At the same time, the reasonable domain size protects the discrete model from an excessive number of finite elements.

For an efficient mesh generation, a quarter-disc of radius $2a$, centered at the origin, is set apart from the whole domain. The defined maximal element size within this subregion is significantly lower than outside. Moreover, taking into account the peak character of the loaded boundary displacement, a nonuniform mesh distribution is applied: mesh density increases towards the loading point. An exemplary fragment of the discretized system $\widehat{\Omega}$ is shown in Figure 13. The quadratic quadrilateral elements are used in the entire domain.

Figure 14 presents numerical results for $\nu = 0.25$ and $\nu = -0.5$ in the nondimensional form: the distribution of displacement U_y and stress S_y as well as the vertical displacement of the loaded surface $-U_y(x, 0)$. Thus, the graphs correspond to Figure 6 (top/middle left and top/middle right) and Figure 7 (left). The displacement and stress fields produced by two different methods are in close agreement with each other. When it comes to the loaded boundary, the maximal displacements obtained with FEM are

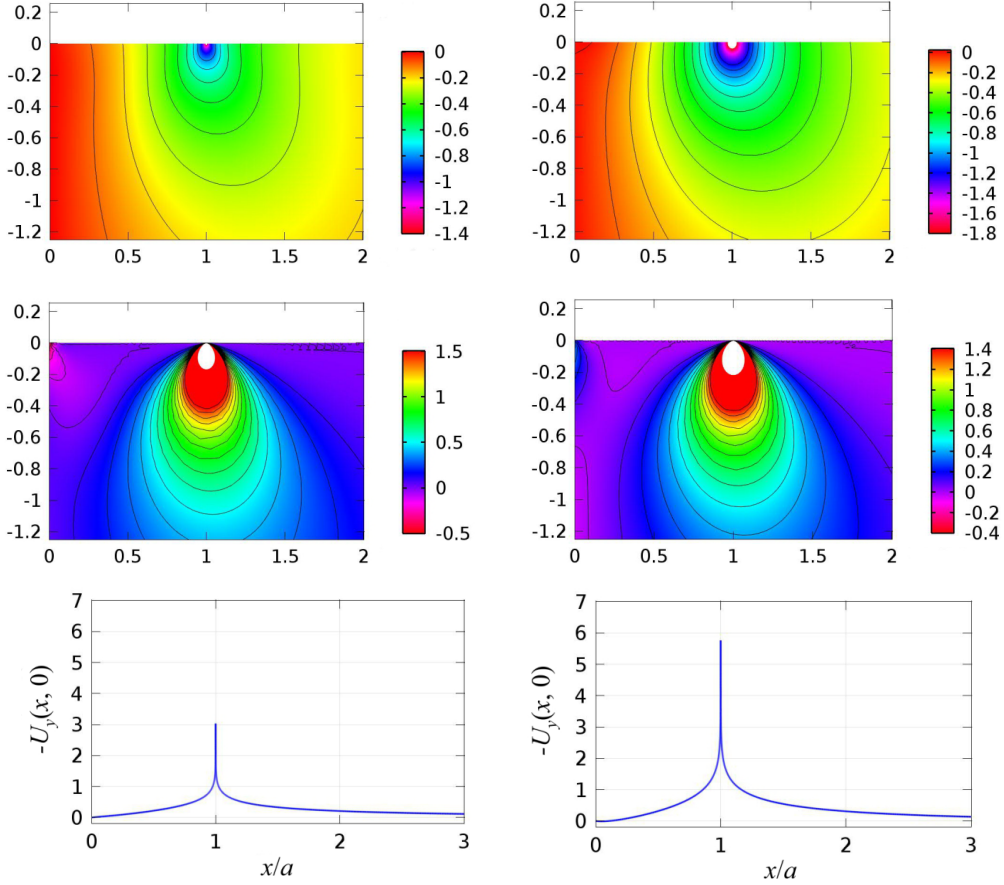


Figure 14. Displacement and stress field for $\nu = 0.25$ (left column) and $\nu = -0.5$ (right column): (top) normal stress S_y , (middle) vertical displacement U_y and (bottom) upward displacement $-U_y$ of the loaded surface.

2–5% greater than the ones from the semianalytical solutions. The simulations were performed for the number of finite elements $n_e = 13\,938$ and the number of degrees of freedom $n_{\text{dof}} = 112\,606$.

In order to examine the convergence of computations, a series of numerical experiments were conducted for gradually increasing mesh density inside the quarter-disc subdomain. As can be seen in Figure 15, left, a significant growth of the maximal value $-U_y(a, 0)$ occurs for relatively small numbers of degrees of freedom. Nevertheless, the displacement stabilizes when $n_{\text{dof}} > 118\,000$. An analogous test for the semianalytical approach (see Figure 15, right) indicates more regular change of the peak displacement with the number of complex poles n_c^* : logarithmic convergence rate is clearly observed (notice the logarithmic scale on the horizontal axis).

It should be emphasized that achieving such an agreement between both methods has been somewhat troublesome from the viewpoint of FEM. Using gradually finer but uniform meshes in the whole quarter-disc region does not bring the expected results: the maximal displacement grows much slower than the number of degrees of freedom. Consequently, gaining reliable values becomes unattainable even for

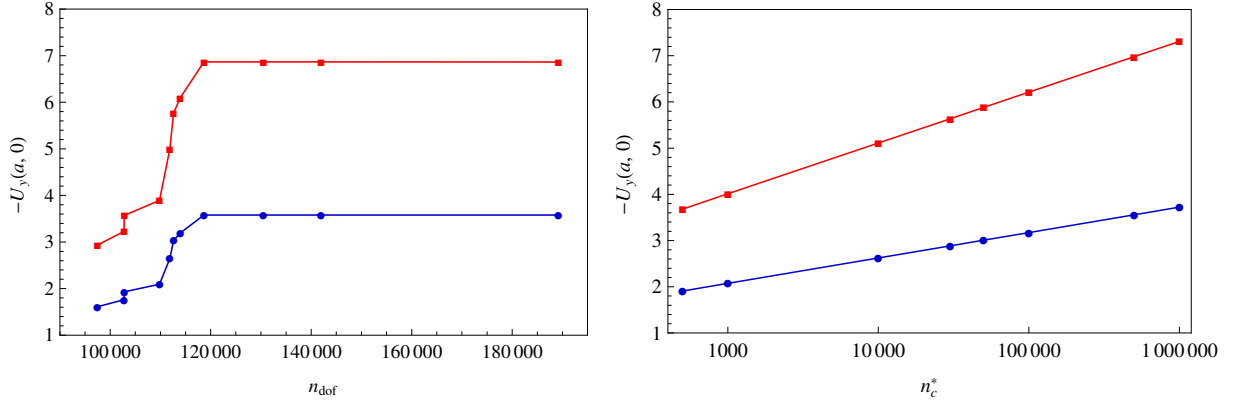


Figure 15. Convergence of the maximal vertical displacement for $\nu = 0.25$ (●) and $\nu = -0.5$ (■): (left) FEM results and (right) results of the semianalytical approach.

users of PCs with relatively large memory resources. Hence, increasing the mesh density locally (at the loading point) is indispensable.

However, these difficulties and, more generally, the requirement for high-resolution computations by the two methods (large n_{dof} and n_c^* , respectively) relate mainly to a small neighborhood of the loading point. The displacement and stress fields far enough from this point are rather weakly affected by a change in n_{dof} and n_c^* .

A comparison of the curve $U_\varphi(r, \pi/2)$ from Figure 8 ($n_c^* = 3 \times 10^4$) and the one obtained by FEM ($n_{\text{dof}} = 112\,606$) for $\nu = -0.75$ is presented in Figure 16. As can be seen, the applied discretization method is sufficient and the results capture the valley effect very well. Noticeable differences appear for $x/a > 3/2$, and they grow with increasing x . However, this discrepancy can be effectively eliminated by adjusting n_{dof} and n_c^* to ensure very close values of the peak displacements $-U_y(a, 0)$ provided by both approaches.

6. Conclusions

In this paper, the distributions of the vertical displacement as well as the normal and shear stresses in a finite subregion of the quarter-plane have been discussed. Much attention has been paid to the deformation of the loaded boundary, which has been analyzed for various values of Poisson's ratio. It has been found that auxetics exhibit an anomalous deformation of the loaded surface near the fixed boundary: the valley effect that intensifies with stronger auxeticity of the material. The obtained results indicate that $\nu = 0$ is just the critical value below which the effect always occurs. A simple explanation of the unusual deformation mechanism has been suggested by using the example of an unconstrained auxetic and nonauxetic solid under a tensile load. The presented solutions are in close agreement with the FEM results, although the latter ones have been obtained for a finite-sized solid.

The discussed valley effect can be treated as a kind of ersatz of negative stiffness (or negative compliance). In the case of the analyzed system, it arises from a combination of specific conditions: constraints (fixed boundary), load (vertical concentrated force) and material ($\nu \leq 0$). But generally, the systems exhibiting negative stiffness are interesting from both theoretical and practical points of view.

Combining an ordinary material with the one of negative stiffness may produce a composite having amazing properties, e.g., very large elastic modulus. In theory, it is possible to construct a material of zero compliance [Maruszewski et al. 2010; Poźniak et al. 2010]. Such modern trends in science and engineering require efficient numerical simulations that cast new light on unusual phenomena that have not yet been investigated experimentally.

Assuming the semi-infinite character of the domain allows for a semianalytical treatment of the problem. Such an approach has a huge advantage compared to purely numerical techniques. One can focus on the displacement and stress analysis of the loaded surface only, without the necessity of solving the problem in the whole domain. Moreover, the proposed method is free from various difficulties connected to the discretization process. Based on the obtained results, it may be concluded that the semianalytical approach exhibits logarithmic convergence.

References

- [Alderson and Alderson 2007] A. Alderson and K. L. Alderson, “Auxetic materials”, *J. Aerosp. Eng. (ASCE)* **221**:4 (2007), 565–575.
- [Bai and Lu 2004] F. Bai and W.-Q. Lu, “The selection and assemblage of approximation functions and disposal of its singularity in axisymmetric DRBEM for heat transfer problems”, *Eng. Anal. Bound. Elem.* **28**:8 (2004), 955–965.
- [Bateman 1954] H. Bateman, *Tables of integral transforms, I*, edited by A. Erdélyi et al., McGraw-Hill, New York, 1954.
- [Bronsztejn et al. 2009] I. N. Bronsztejn, K. A. Siemiendajew, G. Musiol, and H. Mühligh, *Nowoczesne kompendium matematyki*, PWN, Warsaw, 2009.
- [Debnath and Bhatta 2007] L. Debnath and D. Bhatta, *Integral transforms and their applications*, 2nd ed., Chapman & Hall/CRC, Boca Raton, FL, 2007.
- [Erdogan and Arin 1976] F. Erdogan and K. Arin, “Fracture and contact problems for an elastic wedge”, *J. Elasticity* **6**:1 (1976), 57–71.
- [Evans and Alderson 2000] K. E. Evans and K. L. Alderson, “Auxetic materials: the positive side of being negative”, *Eng. Sci. Educ. J.* **9**:4 (2000), 148–154.

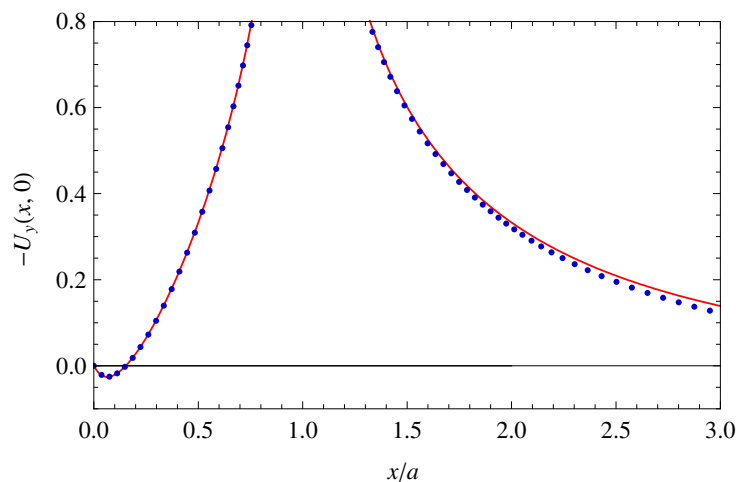


Figure 16. The effect of the anomalous vertical displacement of the loaded surface for $\nu = -0.75$: results of the semianalytical approach (line) and FEM results (dots).

- [Greaves et al. 2011] G. N. Greaves, A. L. Greer, R. S. Lakes, and T. Rouxel, “Poisson’s ratio and modern materials”, *Nat. Mater.* **10**:11 (2011), 823–837.
- [Johnson 1985] K. L. Johnson, *Contact mechanics*, Cambridge Univ. Press, 1985.
- [Kaplan 2002] W. Kaplan, *Advanced calculus*, 5th ed., Addison-Wesley, Boston, 2002.
- [Kącki 1992] E. Kącki, *Równania różniczkowe cząstkowe w zagadnieniach fizyki i techniki*, 3rd ed., WNT, Warsaw, 1992.
- [Lakes 2001] R. S. Lakes, “Extreme damping in composite materials with a negative stiffness phase”, *Phys. Rev. Lett.* **86**:13 (2001), 2897–2900.
- [Lakes et al. 2001] R. S. Lakes, T. Lee, A. Bersie, and Y. Wang, “Extreme damping in composite materials with negative-stiffness inclusions”, *Nature* **410**:6828 (2001), 565–567.
- [Liu 2010] G. R. Liu, *Meshfree methods: moving beyond the finite element method*, 2nd ed., CRC Press, Boca Raton, FL, 2010.
- [Martin 2003] P. A. Martin, “On Green’s function for a bimaterial elastic half-plane”, *Int. J. Solids Struct.* **40**:9 (2003), 2101–2119.
- [Maruszewski et al. 2010] B. Maruszewski, T. Stręk, A. A. Poźniak, and K. W. Wojciechowski, “Computational modelling of auxetics”, Chapter 12, pp. 265–284 in *Finite element analysis*, edited by D. Moratal, Sciyo, Croatia, 2010.
- [Nowacki 1970] W. Nowacki, *Teoria sprężystości*, PWN, Warsaw, 1970.
- [Poźniak et al. 2010] A. A. Poźniak, H. Kamiński, P. Kędziora, B. Maruszewski, T. Stręk, and K. W. Wojciechowski, “Anomalous deformation of constrained auxetic square”, *Rev. Adv. Mater. Sci.* **23**:2 (2010), 169–174.
- [Prawoto 2012] Y. Prawoto, “Seeing auxetic materials from the mechanics point of view: a structural review on the negative Poisson’s ratio”, *Comput. Mater. Sci.* **58** (2012), 140–153.
- [Saada 1993] A. S. Saada, *Elasticity: theory and applications*, 2nd ed., Krieger, Malabar, FL, 1993.
- [Sadd 2005] M. H. Sadd, *Elasticity: theory, applications, and numerics*, Elsevier, Boston, 2005.
- [Sneddon 1951] I. N. Sneddon, *Fourier transforms*, McGraw-Hill, New York, 1951.
- [Theocaris and Makrakis 1987] P. S. Theocaris and G. Makrakis, “Crack kinking in anti-plane shear solved by the Mellin transform”, *Int. J. Fract.* **34**:4 (1987), 251–262.
- [Timoshenko and Goodier 1951] S. Timoshenko and J. N. Goodier, *Theory of elasticity*, 2nd ed., McGraw-Hill, New York, 1951.
- [Tsamasphyros and Theocaris 1979] G. Tsamasphyros and P. S. Theocaris, “On the solution of the sector problem”, *J. Elasticity* **9**:3 (1979), 271–281.
- [Walczak et al. 2014] T. Walczak, G. Sypniewska-Kamińska, B. T. Maruszewski, and K. W. Wojciechowski, “Mesh versus meshless method of elastic displacement determination in a common and an auxetic material”, *Phys. Status Solidi B* **251**:11 (2014), 2225–2232.

Received 30 Sep 2014. Revised 23 Mar 2015. Accepted 23 Mar 2015.

PAWEŁ FRITZKOWSKI: pawel.fritzkowski@put.poznan.pl
Institute of Applied Mechanics, Poznań University of Technology, Jana Pawła II 24, 60-965 Poznań, Poland

HENRYK KAMIŃSKI: henryk.kaminski@put.poznan.pl
Institute of Applied Mechanics, Poznań University of Technology, Jana Pawła II 24, 60-965 Poznań, Poland

LAMINAR FLOW OF A POWER-LAW FLUID BETWEEN CORRUGATED PLATES

JAKUB KRZYSZTOF GRABSKI AND JAN ADAM KOŁODZIEJ

This paper deals with the problem of a steady, fully developed, laminar flow of a power-law fluid between corrugated plates. A nonlinear governing equation is transformed into a sequence of linear inhomogeneous equations by the Picard iteration method. At each iteration step, the inhomogeneous equation is solved using the method of particular solutions in which the solution consists of two parts: the general solution and the particular solution. The right-hand side of the inhomogeneous equation is interpolated using the radial basis functions and monomials, and simultaneously unknown coefficients of the particular solution are obtained. The method of fundamental solutions is applied in order to obtain the general solution. Unknown coefficients of the general solution are calculated by fulfilling the boundary conditions. In this paper, dimensionless velocity of the fluid and the product of the friction factor and Reynolds number fRe are presented for different values of corrugation amplitude and different parameters of the power-law fluid model.

1. Introduction

The problem of a steady, fully developed, laminar flow in ducts of different cross-sectional shapes has received quite extensive attention over the years. A wide range of problems was researched in this area. For instance, a laminar flow between cylinders arranged in a regular array by means of the eigenfunction expansion and the boundary collocation method was investigated by Sparrow and Loeffler [1959]. Zarling [1976] considered flow in different complexly shaped ducts (a circular duct, a square duct, a rectangular duct, an elliptical duct) using the Schwarz–Neumann alternating method along with the boundary collocation method in the least-square sense. Flow in a channel with longitudinal ribs was examined by Wang [1994]. He solved the problem by means of the eigenfunction expansion and the boundary collocation method. The same method was applied by Hu and Yeh [2009] in order to obtain the solution for the problem of a laminar flow in a channel with moving bars. Fluid flow and heat transfer in internally finned tubes were often analyzed in the literature because of their importance from a practical point of view; see for example [Tien et al. 2012].

Also structures with corrugated boundaries have a wide range of practical applications in technology, and one can find many examples in nature. It is worth mentioning the application of this class of flows to corrugated walls in heat exchangers. An experimental comparison of heat and mass transfer between different heat exchangers with corrugated walls was conducted Zimmerer et al. [2002]. Another example of practical problems with corrugated boundaries is peristaltic pumping, which is the transport of fluid induced by a progressive wave of contraction along the distensible duct. Such phenomena exist in many biological systems, e.g., the gastrointestinal tract, the ureter and the small blood vessels. Peristaltic pumps are also used in industry (to transport corrosive or aggressive fluids) and medicine (to transport

Keywords: power-law fluid, corrugated plates, method of fundamental solutions, radial basis functions.

bodily fluids outside the human body). See [Yin and Fung 1971] for a comparison between theory and experiment in peristaltic transport.

Recently more researchers have dealt with the mechanics of non-Newtonian fluids because of their great importance in practical issues, e.g., in plastic processing (molten polymers), the food industry (chocolate, ketchup, yogurt), the personal care industry (shampoo, shaving foam or cream, toothpaste) or medicine (blood, synovial fluid, saliva) [Astarita and Marrucci 1974; Chhabra and Richardson 2008; Irgens 2014]. One of the simplest non-Newtonian fluid models is the power-law fluid. This model is very common in the literature. It was investigated using different numerical methods. Schechter [1961] analyzed flow of a power-law fluid in a rectangular duct using the Ritz method for solving the momentum equation. More accurate results for the same problem were obtained by Wheeler and Wissler [1965], who employed the finite-difference scheme based on the over-relaxation method. The finite-element method was applied to isothermal slow channel flow of power-law fluids by Palit and Fenner [1972]. Their results were compared to the results obtained using the finite-difference method (for rectangular channels) and to an exact solution (Newtonian fluid flow). Liu et al. [1988] presented a comparison of the Galerkin finite-element method and the boundary-fitted coordinate transformation method. The power-law fluid flow in a circular pipe and square and triangular ducts was analyzed. Kostic [1993] investigated flow of a power-law fluid in rectangular ducts by means of the finite-difference method. Fully developed, laminar flow of a power-law fluid in rectangular ducts was also examined by Syrjälä [1995]. He used the finite-element method to solve the momentum equations numerically. Madhav and Malin [1997] analyzed the same problem with application of the single-slab solution procedure. Lima et al. [2000] investigated two-dimensional, laminar flow of a power-law fluid inside the rectangular ducts by means of the generalized integral transform technique.

The problem of fully developed, laminar flow of a Newtonian fluid between corrugated plates was first investigated by Wang [1976]. Ng and Wang [2010] analyzed Darcy–Brinkman flow between corrugated plates. To our best knowledge, there are no other published works on the flow between corrugated plates. The purpose of this paper is to analyze the flow of a power-law fluid between corrugated plates using the method of fundamental solutions and the radial basis functions.

2. Method of fundamental solutions and its applications to solving nonlinear problems

The method of fundamental solutions (MFS) is a meshless method. The method can be applied to solve problems described by partial differential equations for which the fundamental solutions are known. The fundamental solution is a function of a distance between a point inside the considered region and a source point. The source points are located on a *pseudoboundary* that is outside the considered region. The boundary of the considered region and the pseudoboundary do not have any common points. The approximate solution in the MFS is assumed to be a linear combination of fundamental solutions. The governing equation is satisfied exactly by the fundamental solution at any point in the considered region, which also ensures that the approximate solution fulfills the governing equation at any point of the region. The boundary conditions are fulfilled approximately using the boundary collocation technique. The MFS was originally proposed by Kupradze and Aleksidze [1964]. A numerical implementation of the MFS was presented in [Mathon and Johnston 1977]. Some noteworthy review articles can be found in the literature. A review of the MFS applications to elliptic boundary problems was presented in [Fairweather

and Karageorghis 1998] while a review of applications of the MFS to scattering and radiation problems was included in [Fairweather et al. 2003]. Applications of the MFS to inverse problems, in turn, were reviewed in [Karageorghis et al. 2011].

The MFS can also be found in the literature under other names: the superposition method [Burgess and Mahajerin 1984], the boundary point method [Johnson 1987], the fundamental solutions method [Bogomolny 1985], the source functions method [de Mey 1978], the fundamental collocation method [Burgess and Mahajerin 1987], the charge simulation method [Amano 1998] or the regular indirect boundary element method [Wearing and Sheikh 1988].

The problem of a steady, fully developed, laminar flow of a power-law fluid is governed by a nonlinear equation. There are only a few examples of applications of the MFS to such problems, and the first attempt to use the MFS for a nonlinear Poisson problem was probably given in [Burgess and Mahajerin 1987]. In that paper, the particular solution was expressed as an integral over the considered region and as a sum of the right-hand-side function times the fundamental solution. Then the Picard iteration method was applied. In [Balakrishnan and Ramachandran 1999; Balakrishnan et al. 2002; Chen 1995; Wang and Qin 2006; Wang et al. 2006], an original nonlinear Poisson-type differential equation in a two-dimensional domain was converted into a sequence of linear Poisson equations. Then the radial basis functions (RBF) and the MFS were applied respectively to construct the expression of the particular and the homogeneous solutions at each iteration step. This procedure was used for more complicated problems of applied mechanics: heat conduction problems in anisotropic and inhomogeneous media [Wang et al. 2005], large deflection of plates [Klekiel and Kołodziej 2006], isothermal gas flow in porous medium [Uściłowska and Kołodziej 2006], thermoelasticity of functionally graded materials [Wang and Qin 2008], nonlinear elliptic problems [Li and Zhu 2009], determination of effective thermal conductivity of unidirectional composites with linearly temperature-dependent conductivity of constituents [Kołodziej and Uściłowska 2012], two-dimensional nonlinear elasticity [Al-Gahtani 2012], elastoplastic torsion of prismatic rods [Kołodziej and Gorzelańczyk 2012], dynamic response of von Karman nonlinear plate model [Uściłowska and Berendt 2013] and some inverse problems [Kołodziej et al. 2013; Mierzwiczak and Kołodziej 2011]. Balakrishnan and Ramachandran [2001] solved nonlinear Poisson problems by means of the method of fundamental solutions and radial basis functions called the oscillatory radial basis functions.

Application of the MFS to a Laplace equation with a nonlinear boundary condition was presented by Karageorghis and Fairweather [1989], who considered nonlinear plane potential problems. Steady-state heat conduction with temperature-dependent thermal conductivity and mixed boundary conditions involving radiation was investigated in [Karageorghis and Lesnic 2008a]. In that paper, the classical Kirchhoff transformation was employed. In this way, the governing equation was transformed to the Laplace equation and the only nonlinearity in the new boundary value problem was included in nonlinear boundary conditions. The nonlinear system of algebraic equations was then solved by a standard procedure. The same numerical algorithm was applied for steady-state nonlinear heat conduction in composite materials [Karageorghis and Lesnic 2008b]. A similar approach with the MFS was used for the water wave problem [Kołodziej and Mierzwiczak 2008; Mollazadeh et al. 2011; Wu and Tsay 2009; Wu et al. 2006; 2008].

A linearization scheme for an inhomogeneous term in terms of a dependent variable and the first or second derivative with respect to time, resulting in a Helmholtz-type equation (for which the fundamental

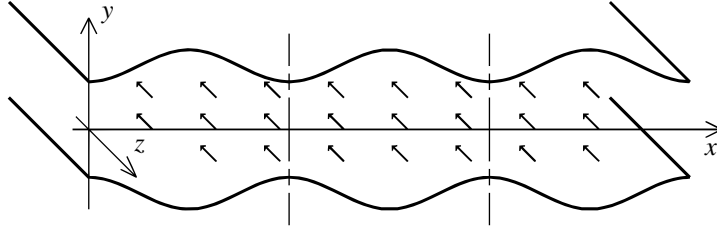


Figure 1. Geometry of the considered problem.

solution is known), was proposed in [Fallahi 2012; Fallahi and Hosami 2011]. Consequently, the particular solutions are no longer needed and the MFS can be directly applied to the linearized equation. In [Tri et al. 2011; 2012], the perturbation technique was combined with the MFS in order to solve a nonlinear Poisson-type equation. The nonlinear problem was transformed into a sequence of inhomogeneous linear problems that can be solved by the MFS and the RBF. The homotopy analysis method combined with the MFS was applied to solve a nonlinear Poisson-type problem in [Tsai 2012]. The Eulerian–Lagrangian method in combination with the MFS was used by Young et al. [2008] in order to solve the nonlinear unsteady Burgers equation. In [Young et al. 2009], unsteady Navier–Stokes equations were transformed into simple advection-diffusion and Poisson equations by the operator-splitting scheme. The obtained advection-diffusion equations and pressure Poisson equation were then solved using the MFS together with the Eulerian–Lagrangian method and the method of particular solution. Feng et al. [2013] solved potential flow for predicting ship motion responses in the frequency domain. The MFS was also successfully applied to nonlinear functionally graded materials [Li et al. 2014; Marin and Lesnic 2007]. Moreover, there are examples of using the MFS in combination with the hybrid finite-element model for solving nonlinear Poisson-type problems [Wang et al. 2012].

In this paper, power-law fluid flow between corrugated plates is investigated by employing the MFS and the RBF. This nonlinear problem is transformed into a sequence of linear inhomogeneous problems using the Picard iteration method. Then the method of particular solution is applied at each iteration step. The RBF and monomials are used in order to interpolate the right-hand side of the inhomogeneous equation and to obtain the particular solution while the MFS is employed to obtain the general solution.

3. Statement of the problem

The geometry of the considered problem is illustrated in Figure 1. The flow is limited by two symmetrical, corrugated plates. The fluid flows between these plates in the direction parallel to the z axis.

The upper and lower walls (plates) can be represented by

$$y = \pm \left[h + \varepsilon \cdot \cos\left(\frac{2\pi x}{2\lambda}\right) \right], \quad (3-1)$$

where h denotes average distance between the plate and the x axis, ε is corrugation amplitude and λ denotes length of the repeating part of the considered region Ω .

After introducing dimensionless quantities

$$X = \frac{x}{\lambda}, \quad Y = \frac{y}{\lambda}, \quad H = \frac{h}{\lambda}, \quad E = \frac{\varepsilon}{\lambda}, \quad L = \frac{\lambda}{\lambda} = 1, \quad (3-2)$$

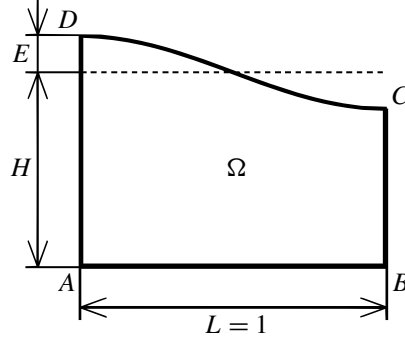


Figure 2. The repeating part of the considered region Ω with characteristic dimensionless quantities.

(3-1) takes the form

$$Y = \pm[H + E \cdot \cos(\pi X)]. \quad (3-3)$$

The repeating part of the considered region Ω with characteristic dimensionless quantities is depicted in Figure 2.

The following equation can be written in the Cartesian coordinate system for steady, fully developed, laminar, axial flow of a power-law fluid:

$$\frac{\partial}{\partial x} \left(\eta(\gamma) \frac{\partial w(x, y)}{\partial x} \right) + \frac{\partial}{\partial y} \left(\eta(\gamma) \frac{\partial w(x, y)}{\partial y} \right) = \frac{dp}{dz}, \quad (3-4)$$

where $w(x, y)$ is axial velocity (velocity of the fluid has only one component), $\frac{dp}{dz}$ is the constant pressure gradient, $\eta(\gamma)$ is the viscosity function (which in the literature is also called apparent viscosity) and

$$\gamma = \sqrt{\left(\frac{\partial w(x, y)}{\partial x} \right)^2 + \left(\frac{\partial w(x, y)}{\partial y} \right)^2}. \quad (3-5)$$

The viscosity function for the power-law fluid takes the form

$$\eta(\gamma) = K \cdot \gamma^{m-1}, \quad (3-6)$$

where K is the consistency factor and m is the power-law index. For $m < 1$, the fluid shows shear-thinning (pseudoplastic) behavior, and for $m > 1$, the fluid shows shear-thickening (dilatant) behavior. If $m = 1$, the fluid shows Newtonian behavior.

For the considered region Ω , the following boundary conditions are formulated:

$$\frac{\partial w(x, y)}{\partial y} = 0 \quad \text{on AB} \quad (\text{symmetry condition}), \quad (3-7)$$

$$\frac{\partial w(x, y)}{\partial x} = 0 \quad \text{on BC and DA} \quad (\text{symmetry condition}), \quad (3-8)$$

$$w(x, y) = 0 \quad \text{on CD} \quad (\text{nonslip condition}). \quad (3-9)$$

Introducing dimensionless quantities (3-2) as well as dimensionless velocity

$$W(X, Y) = \frac{w(x, y)}{\frac{\lambda^2 dp}{\mu_r dz}} \quad (3-10)$$

(where μ_r is reference viscosity) and dimensionless viscosity function

$$E(\chi) = \frac{\eta(\gamma)}{\mu_r}, \quad (3-11)$$

(3-4) takes the form

$$\frac{\partial}{\partial X} \left(E(\chi) \frac{\partial W(X, Y)}{\partial X} \right) + \frac{\partial}{\partial Y} \left(E(\chi) \frac{\partial W(X, Y)}{\partial Y} \right) = -1, \quad (3-12)$$

where

$$\chi = \sqrt{\left(\frac{\partial W(X, Y)}{\partial X} \right)^2 + \left(\frac{\partial W(X, Y)}{\partial Y} \right)^2}. \quad (3-13)$$

Dimensionless viscosity function $E(\chi)$ for the power-law fluid can be represented by

$$E(\chi) = B_1 \cdot \chi^{m-1}, \quad (3-14)$$

where B_1 is a dimensionless consistency factor defined as

$$B_1 = \frac{K}{\mu_r} \left(\frac{K}{\mu_r} \frac{dp}{dz} \right)^{m-1}. \quad (3-15)$$

Finally after some mathematical operations, the considered problem is defined by the governing equation

$$\nabla^2 W(X, Y) = -\frac{1}{E(\chi)} \left(1 + \frac{\partial E(\chi)}{\partial X} \frac{\partial W(X, Y)}{\partial X} + \frac{\partial E(\chi)}{\partial Y} \frac{\partial W(X, Y)}{\partial Y} \right) \quad (3-16)$$

with the boundary conditions

$$\frac{\partial W(X, Y)}{\partial Y} = 0 \quad \text{on AB}, \quad (3-17)$$

$$\frac{\partial W(X, Y)}{\partial X} = 0 \quad \text{on BC and DA}, \quad (3-18)$$

$$W(X, Y) = 0 \quad \text{on CD}. \quad (3-19)$$

4. The proposed method of solution

In this paper, the Picard iteration method is used in order to solve the nonlinear equation (3-16). Then the nonlinear governing equation (3-16) is transformed into a sequence of inhomogeneous problems in which the value of velocity from the previous iteration step is used on the right-hand side of the equation. At the i -th iteration step, the inhomogeneous problem is described by

$$\nabla^2 W^{[i]}(X, Y) = -\frac{1}{E^{[i-1]}(\chi)} \left(1 + \frac{\partial E^{[i-1]}(\chi)}{\partial X} \frac{\partial W^{[i-1]}(X, Y)}{\partial X} + \frac{\partial E^{[i-1]}(\chi)}{\partial Y} \frac{\partial W^{[i-1]}(X, Y)}{\partial Y} \right). \quad (4-1)$$

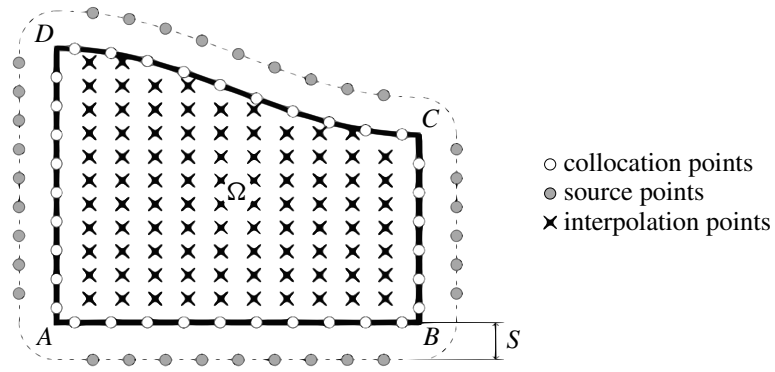


Figure 3. Distribution of the collocation points, the source points and the interpolation points.

The first approximation is obtained for a Newtonian fluid ($B_1 = 1$ and $m = 1$). Then the problem is described by the governing equation

$$\nabla^2 W^{[1]}(X, Y) = -1 \quad (4-2)$$

with boundary conditions (3-17)–(3-19). In order to solve the above equation, the following additional function is introduced:

$$\Phi(X, Y) = W^{[1]}(X, Y) + \frac{1}{4}(X^2 + Y^2 - 1). \quad (4-3)$$

Then (4-2) is transformed into the Laplace equation

$$\nabla^2 \Phi(X, Y) = 0. \quad (4-4)$$

The boundary conditions formulated for the additional function $\Phi(X, Y)$ take the forms

$$\frac{\partial \Phi(X, Y)}{\partial Y} = \frac{1}{2}Y \quad \text{on AB}, \quad (4-5)$$

$$\frac{\partial \Phi(X, Y)}{\partial X} = \frac{1}{2}X \quad \text{on BC and DA}, \quad (4-6)$$

$$\Phi(X, Y) = \frac{1}{4}(X^2 + Y^2 - 1) \quad \text{on CD}. \quad (4-7)$$

The problem described by (4-4) with boundary conditions (4-5)–(4-7) in the considered region Ω can easily be solved using the MFS.

In this method, the approximate solution is assumed to be a linear combination of fundamental solutions. The fundamental solution for the Laplace operator is given by

$$f_S(r_j) = \ln r_j, \quad (4-8)$$

where r_j is the distance between the point (X, Y) and the j -th source point (X_j, Y_j) :

$$r_j = \sqrt{(X - X_j)^2 + (Y - Y_j)^2}. \quad (4-9)$$

The source points are located outside the considered region Ω on the pseudoboundary at a distance S from the domain boundary as shown in Figure 3.

The approximate solution of the problem described by (4-4) and boundary conditions (4-5)–(4-7) takes the form

$$\Phi(X, Y) = \sum_{j=1}^{N_S} c_j^{[1]} \ln r_j, \quad (4-10)$$

where N_S is the number of source points. The unknown coefficients $c_j^{[1]}$ ($j = 1, \dots, N_S$) are calculated using the boundary collocation technique (by fulfilling boundary conditions at N_C collocation points) [Kołodziej and Zieliński 2009].

Thus, the solution of the original problem described by the governing equation (4-2) and boundary conditions (3-17)–(3-19) can be written as

$$W^{[1]}(X, Y) = \sum_{j=1}^{N_S} c_j^{[1]} \ln r_j - \frac{1}{4}(X^2 + Y^2 - 1). \quad (4-11)$$

At subsequent iteration steps, the problem described by the inhomogeneous equation (4-1) with boundary conditions (3-17)–(3-19) is solved using the method of particular solutions. In this method, the solution of the considered problem consists of two parts:

$$W^{[i]}(X, Y) = W_g^{[i]}(X, Y) + W_p^{[i]}(X, Y), \quad (4-12)$$

where $W_g^{[i]}(X, Y)$ is the general solution and $W_p^{[i]}(X, Y)$ is the particular solution.

The right-hand side of (4-1) at the i -th iteration step can be denoted by

$$b^{[i]}(X, Y) = -\frac{1}{E^{[i-1]}(\chi)} \left(1 + \frac{\partial E^{[i-1]}(\chi)}{\partial X} \frac{\partial W^{[i-1]}(X, Y)}{\partial X} + \frac{\partial E^{[i-1]}(\chi)}{\partial Y} \frac{\partial W^{[i-1]}(X, Y)}{\partial Y} \right). \quad (4-13)$$

The particular solution is obtained by interpolation of the right-hand side of (4-1) using the RBF and monomials:

$$\sum_{m=1}^{N_m} \alpha_m^{[i]} \varphi(r_m) + \sum_{k=1}^{N_k} \beta_k^{[i]} p_k(X, Y) = b^{[i]}(X, Y), \quad (4-14)$$

where N_m is the number of interpolation points, N_k is the number of monomials, $\varphi(r_m)$ is the form of the RBF, $p_k(X, Y)$ is the form of the k -th monomial and

$$r_m = \sqrt{(X - X_m)^2 + (Y - Y_m)^2} \quad (4-15)$$

is the distance between the point (X, Y) and the m -th interpolation point (X_m, Y_m) . The unknown coefficients $\alpha_m^{[i]}$ ($m = 1, \dots, N_m$) and $\beta_k^{[i]}$ ($k = 1, \dots, N_k$) are calculated by solving the set of equations

$$\left\{ \begin{array}{l} \sum_{m=1}^{N_m} \alpha_m^{[i]} \varphi(r_{m \text{ int}}) + \sum_{k=1}^{N_k} \beta_k^{[i]} p_k(X_{\text{int}}, Y_{\text{int}}) = b(X_{\text{int}}, Y_{\text{int}}), \quad 1 \leq \text{int} \leq N_m, \\ \sum_{m=1}^{N_m} \alpha_m^{[i]} p_k(X_m, Y_m) = 0, \quad 1 \leq k \leq N_k. \end{array} \right. \quad (4-16)$$

k	$p_k(X, Y)$	$\hat{p}_k(X, Y)$
1	1	$\frac{1}{4}(X^2 + Y^2)$
2	X	$\frac{1}{8}(X(X^2 + Y^2))$
3	Y	$\frac{1}{8}(Y(X^2 + Y^2))$
4	$X \cdot Y$	$\frac{1}{12}(XY(X^2 + Y^2))$
5	X^2	$\frac{1}{14}(X^4 + X^2Y^2 - \frac{1}{6}Y^4)$
6	Y^2	$\frac{1}{14}(Y^4 + X^2Y^2 - \frac{1}{6}X^4)$

Table 1. Forms of the monomials and their particular solutions for the Laplace operator.

The particular solution is represented by

$$W_p^{[i]}(X, Y) = \sum_{m=1}^{N_m} \alpha_m^{[i]} \hat{\varphi}(r_m) + \sum_{k=1}^{N_k} \beta_k^{[i]} \hat{p}_k(X, Y), \quad (4-17)$$

where $\hat{\varphi}(r_m)$ is the particular solution that corresponds to the m -th RBF and $\hat{p}_k(X, Y)$ is the particular solution related to the k -th monomial.

In this paper, the multiquadric function (MQ) is used as the RBF:

$$\varphi(r_m) = \sqrt{r_m^2 + c^2}, \quad (4-18)$$

where c is the shape parameter. The particular solution corresponding to the MQ for the Laplace operator takes the form

$$\hat{\varphi}(r_m) = -\frac{1}{3}c^3 \ln\left(\sqrt{r_m^2 + c^2} + c\right) + \frac{1}{9}(4c^2 + r_m^2)\sqrt{r_m^2 + c^2}. \quad (4-19)$$

The forms of monomials and their particular solutions used in the paper are presented in Table 1.

The general solution is a solution of the Laplace equation

$$\nabla^2 W_g^{[i]}(X, Y) = 0 \quad (4-20)$$

and can be easily found by the MFS in the form

$$W_g^{[i]}(X, Y) = \sum_{j=1}^{N_s} d_j^{[i]} \ln r_j. \quad (4-21)$$

The distance between the point (X, Y) and the j -th source point is defined by (4-9). The unknown coefficients $d_j^{[i]}$ ($j = 1, \dots, N_s$) are calculated using the boundary collocation technique.

Thus, the whole solution of the considered problem at the i -th iteration step takes the form

$$W^{[i]}(X, Y) = \sum_{j=1}^{N_s} d_j^{[i]} \ln r_j + \sum_{m=1}^{N_m} \alpha_m^{[i]} \hat{\varphi}(r_m) + \sum_{k=1}^{N_k} \beta_k^{[i]} \hat{p}_k(X, Y). \quad (4-22)$$

The same numerical procedure was successfully applied for other problems and can be found, e.g., in [Golberg et al. 1998].

Step 1	Input parameters of the considered region: H , E and m .
Step 2	Input parameters of the method: N_C , N_S , S , N_m , N_k , c and tolerance of the convergence error tol.
Step 3	Calculate the first approximation (for a Newtonian fluid): $W^{[1]}(X, Y) = \sum_{j=1}^{N_S} c_j^{[1]} \ln r_j - \frac{1}{4}(X^2 + Y^2 - 1).$
Step 4	Take $i = 2$.
Step 5	Interpolate the right-hand side of (4-1): calculate unknown coefficients of the particular solution $\alpha_m^{[i]}$ and $\beta_k^{[i]}$.
Step 6	Fulfill boundary conditions: calculate unknown coefficients of the general solution $d_j^{[i]}$.
Step 7	Calculate the whole solution at the i -th iteration step at selected control points: $W^{[i]}(X, Y) = \sum_{j=1}^{N_S} d_j^{[i]} \ln r_j + \sum_{m=1}^{N_m} \alpha_m^{[i]} \hat{\phi}(r_m) + \sum_{k=1}^{N_k} \beta_k^{[i]} \hat{p}_k(X, Y).$
Step 8	Check the condition for stopping of the iteration process: If $\ W^{[i]}(X, Y) - W^{[i-1]}(X, Y)\ < \text{tol}$, then STOP. Else, take $i = i + 1$ and go to Step 5.
Step 9	Calculate average velocity W_{av} and product of the friction factor and Reynolds number $f\text{Re}$.

Table 2. Numerical algorithm of the proposed method of solution.

The dimensionless average velocity is defined as

$$W_{\text{av}} = \frac{\int_{\Omega} W(X, Y) d\Omega}{\int_{\Omega} d\Omega} = \frac{\int_0^1 \int_0^{H+E \cos(\pi X)} W(X, Y) dY dX}{\int_0^1 \int_0^{H+E \cos(\pi X)} dY dX} = \frac{\int_0^1 \int_0^{H+E \cos(\pi X)} W(X, Y) dY dX}{H}. \quad (4-23)$$

The above quantity is calculated numerically using the obtained approximate solution (4-22) and the trapezoidal rule.

For noncircular ducts, the friction factor can be defined as

$$f = \left(-\frac{dp}{dz} \right) \frac{2D_h}{w_{\text{av}}^2 \rho}, \quad (4-24)$$

where D_h is hydraulic diameter, w_{av} is dimensional average velocity and ρ is fluid density.

Reynolds number Re for noncircular ducts is given by

$$\text{Re} = \frac{\rho w_{\text{av}} D_h}{\mu_r}. \quad (4-25)$$

Let us introduce dimensionless hydraulic diameter

$$\tilde{D}_h = \frac{D_h}{\lambda}, \quad (4-26)$$

which is defined as

$$\tilde{D}_h = \frac{4\tilde{A}}{\tilde{P}}, \quad (4-27)$$

where

$$\tilde{A} = \int_0^1 \int_0^{H+E \cos(\pi X)} dY dX = H \quad (4-28)$$

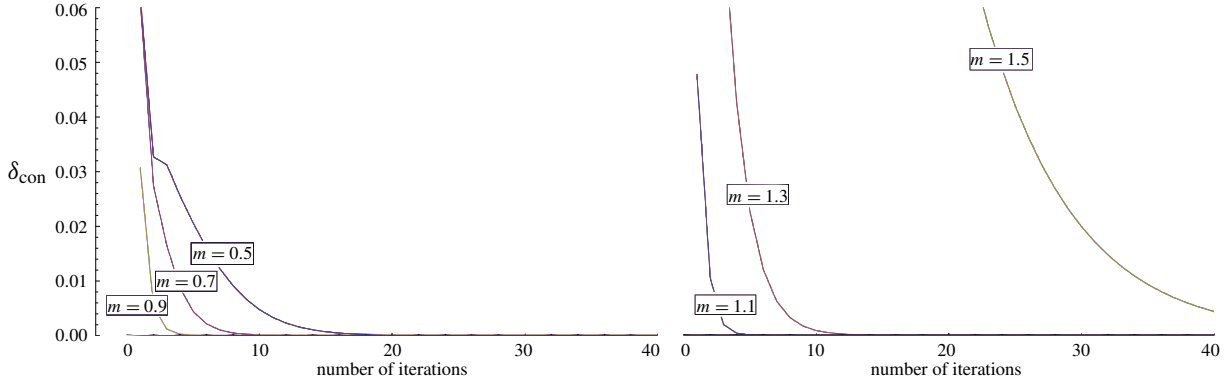


Figure 4. Convergence of the iteration process: (left) for power-law index below 1 and (right) for power-law index above 1.

is the dimensionless area of the considered region Ω and

$$\tilde{P} = \int_0^1 \sqrt{1 + [E\pi \sin(\pi X)]^2} dX. \tag{4-29}$$

is the dimensionless wetted perimeter. The above integral is calculated numerically using the trapezoidal rule.

Thus, the product of the friction factor and Reynolds number can be expressed by

$$fRe = \frac{32\tilde{A}^2}{W_{av}\tilde{P}^2}. \tag{4-30}$$

In order to summarize this part of the paper, i.e., the proposed method of solution, the numerical algorithm of the method is presented in Table 2.

5. Results

In the first numerical experiment, convergence of the iteration process is investigated. In Figure 4, the maximal error of the convergence of the iteration process at subsequent iteration steps is presented. The error of the convergence of the iteration process is defined as

$$\delta_{con} = \|W^{[i]}(X, Y) - W^{[i-1]}(X, Y)\|. \tag{5-1}$$

It can be observed that, if power-law index m is less than 1, the convergence process is faster for greater values of m (Figure 4, left). If m is greater than 1, in turn, the convergence process is faster for smaller values of m (Figure 4, right). In general, the convergence process is faster if m is closer to 1. However, the convergence for all the presented values of the power-law index is satisfactory.

The effect of corrugation amplitude E on the error of the convergence of the iteration process δ_{con} is shown in Table 3. The error δ_{con} at subsequent steps for different values of E varies in the same range. This implies that E has very little effect on the convergence of the proposed iteration process.

In Figure 5, equivelocity lines for different values of corrugation amplitude E are presented. It can be observed that, with increasing value of corrugation amplitude, equivelocity lines move in the direction

Iteration step	$E = 0.2$	$E = 0.4$	$E = 0.6$
1	$9.7009 \cdot 10^{-2}$	$7.3963 \cdot 10^{-2}$	$8.4669 \cdot 10^{-2}$
2	$2.8207 \cdot 10^{-2}$	$3.4205 \cdot 10^{-2}$	$3.5555 \cdot 10^{-2}$
3	$1.6416 \cdot 10^{-2}$	$1.6635 \cdot 10^{-2}$	$1.6297 \cdot 10^{-2}$
4	$6.5646 \cdot 10^{-3}$	$8.1569 \cdot 10^{-3}$	$7.6351 \cdot 10^{-3}$
5	$3.3554 \cdot 10^{-3}$	$3.9547 \cdot 10^{-3}$	$3.5712 \cdot 10^{-3}$
6	$1.4004 \cdot 10^{-3}$	$1.8884 \cdot 10^{-3}$	$1.6563 \cdot 10^{-3}$
7	$6.6425 \cdot 10^{-4}$	$8.8845 \cdot 10^{-4}$	$7.6053 \cdot 10^{-4}$
8	$2.7702 \cdot 10^{-4}$	$4.1252 \cdot 10^{-4}$	$3.4597 \cdot 10^{-4}$
9	$1.2521 \cdot 10^{-4}$	$1.8939 \cdot 10^{-4}$	$1.5600 \cdot 10^{-4}$
10	$5.2102 \cdot 10^{-5}$	$8.6167 \cdot 10^{-5}$	$6.9937 \cdot 10^{-5}$

Table 3. The error of the convergence of the iteration process for different values of corrugation amplitude E in subsequent iteration steps.

of the bottom-left corner of the considered region Ω where the value of fluid velocity is maximal. Thus, the value of velocity (also the maximal value) decreases with increasing values of E .

Equivelocity lines for different values of power-law index m are shown in Figure 6. As shown, the density of equivelocity lines increases and the value of fluid velocity increases with increasing m .

Figure 7 presents average velocity W_{av} for various values of power-law index m and corrugation amplitude E . It can be observed that W_{av} decreases with increasing E (it can be observed also in Figure 5). The value of W_{av} for the same E increases with increasing m . For steady, fully developed, laminar flow of a Newtonian fluid between parallel plates, $W_{av} = \frac{1}{3}$. One can observe that, for pseudoplastic fluids

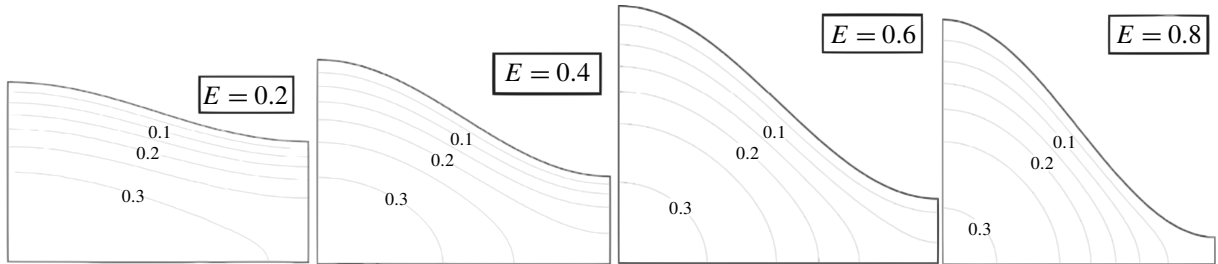


Figure 5. Equivelocity lines for different values of corrugation amplitude.

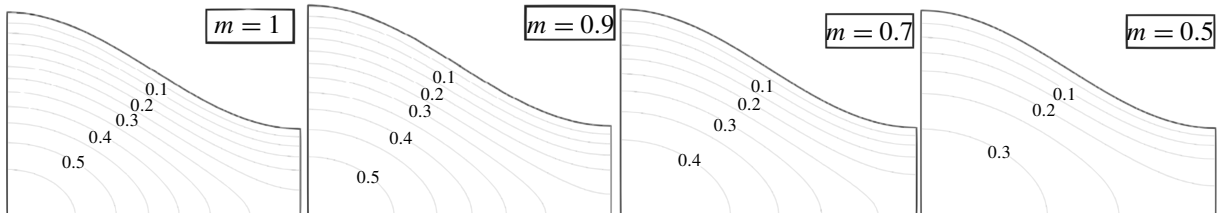


Figure 6. Equivelocity lines for different values of power-law index m .

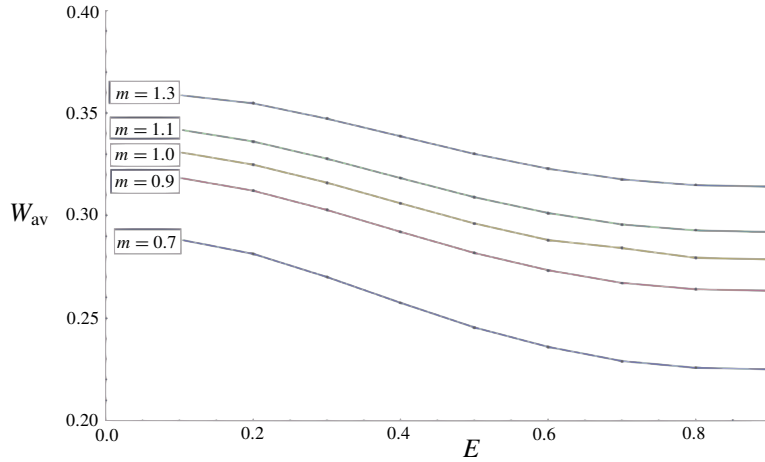


Figure 7. Average velocity W_{av} for different values of corrugation amplitude E and different values of power-law index m .

($m < 1$), W_{av} is always less than for Newtonian flow between parallel plates. In the case of dilatant fluids ($m > 1$), W_{av} is greater than for Newtonian flow between parallel plates but only for smaller values of E .

In Figure 8, the effect of corrugation amplitude E and power-law index m on the product of the friction factor and Reynolds number fRe is illustrated. For the same E , fRe increases with decreasing m . For the same m , fRe decreases with increasing E . For steady, fully developed, laminar flow of a Newtonian fluid between parallel plates, $fRe = 96$. It can be observed that fRe is always less than for the case of Newtonian flow between parallel plates for dilatant fluids $m > 1$, and for pseudoplastic fluids ($m < 1$), fRe is greater than for the case of Newtonian flow between parallel plates only for smaller values of E .

Dimensionless average velocity W_{av} for different dimensionless consistency factors B_1 and different values of dimensionless corrugation amplitude E is shown in Figure 9. It can be seen that W_{av} decreases with increasing B_1 .

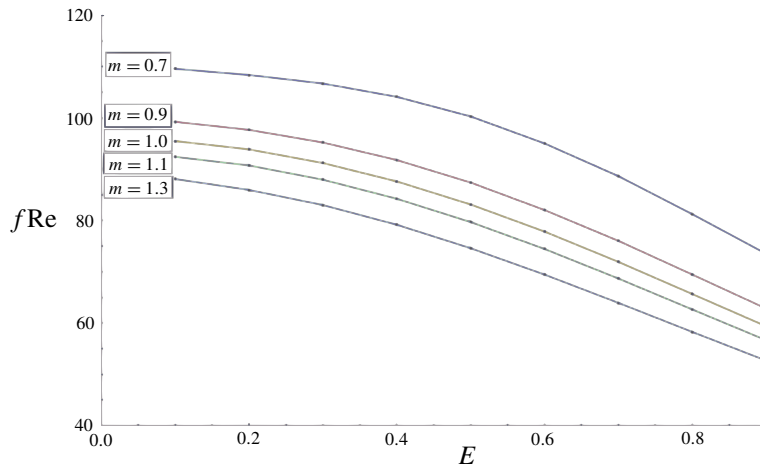


Figure 8. Product of friction factor and Reynolds number fRe for different values of corrugation amplitude E and different values of power-law index m .

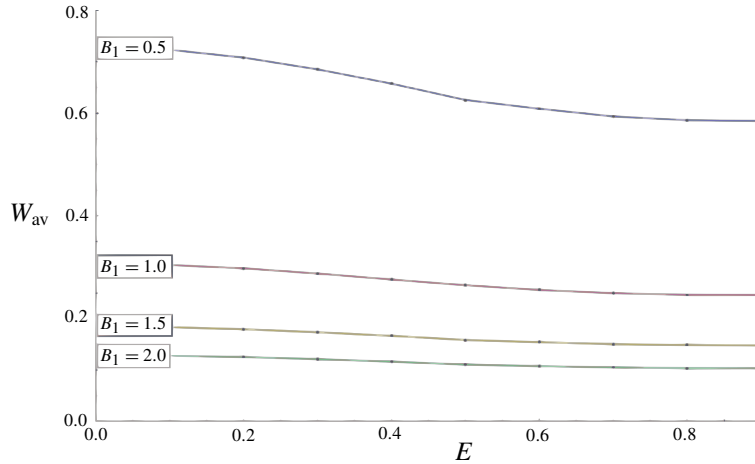


Figure 9. Average velocity W_{av} for different values of corrugation amplitude E and different values of dimensionless consistency factor B_1 .

Figure 10 presents the product of the friction factor and Reynolds number fRe for different dimensionless consistency factors B_1 and different values of dimensionless corrugation amplitude E . It can be observed that fRe increases with increasing B_1 .

6. Conclusions

On the basis of the performed numerical experiments, the following conclusions can be drawn:

- (1) The application of the MFS in combination with the RBF for the problem of fully developed, laminar flow of a power-law fluid between corrugated plates gives satisfactory results.
- (2) Amplitude of corrugation E has little effect on the iteration process convergence.
- (3) Satisfactory convergence is obtained faster if power-law index m is closer to 1.

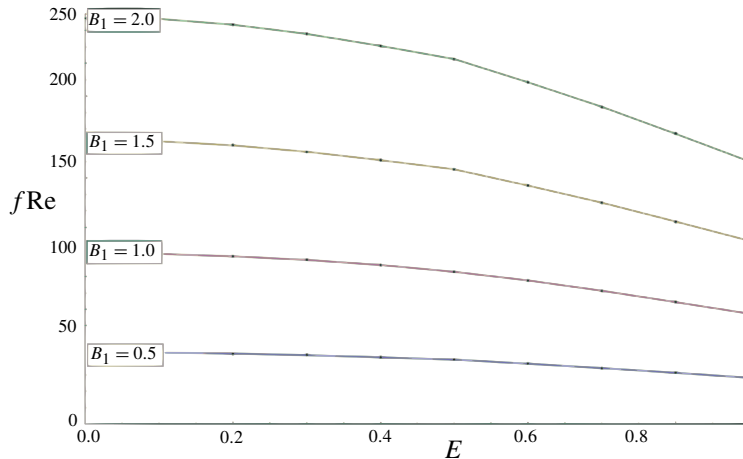


Figure 10. Product of friction factor and Reynolds number fRe for different values of corrugation amplitude E and different values of dimensionless consistency factor B_1 .

- (4) Average velocity W_{av} and the product of the friction factor and Reynolds number fRe decrease with increasing E .
- (5) Average velocity W_{av} for a power-law fluid takes lower values than average velocity for a Newtonian fluid ($B_1 = 1$ and $m = 1$). Average velocity W_{av} increases with increasing m and decreases with increasing value of dimensionless consistency factor B_1 .
- (6) Product fRe is greater for a power-law fluid than a Newtonian fluid and decreases with increasing E . Product fRe decreases with increasing m and increases with increasing B_1 .
- (7) For pseudoplastic fluids ($m < 1$), W_{av} is less than for Newtonian flow between parallel plates and fRe is greater than in the case of Newtonian flow between parallel plates only for smaller values of E .
- (8) For dilatant fluids ($m > 1$), W_{av} is greater than for Newtonian flow between parallel plates but only for smaller E and fRe is less than for the case of Newtonian flow between parallel plates.

Acknowledgements

This work was supported by the grants 02/21/DSMK/3457 from the Polish Ministry of Science and Higher Education (Grabski) and 2012/07/B/ST8/03449 from the National Science Center (Kołodziej).

References

- [Al-Gahtani 2012] H. J. Al-Gahtani, “DRM—MFS for two-dimensional finite elasticity”, *Eng. Anal. Bound. Elem.* **36**:10 (2012), 1473–1477.
- [Amano 1998] K. Amano, “A charge simulation method for numerical conformal mapping onto circular and radial slit domains”, *SIAM J. Sci. Comput.* **19**:4 (1998), 1169–1187.
- [Astarita and Marrucci 1974] G. Astarita and G. Marrucci, *Principles of non-Newtonian fluid mechanics*, McGraw-Hill, Maidenhead, UK, 1974.
- [Balakrishnan and Ramachandran 1999] K. Balakrishnan and P. A. Ramachandran, “A particular solution Trefftz method for non-linear Poisson problems in heat and mass transfer”, *J. Comput. Phys.* **150**:1 (1999), 239–267.
- [Balakrishnan and Ramachandran 2001] K. Balakrishnan and P. A. Ramachandran, “Osculatory interpolation in the method of fundamental solution for nonlinear Poisson problems”, *J. Comput. Phys.* **172**:1 (2001), 1–18.
- [Balakrishnan et al. 2002] K. Balakrishnan, R. Sureshkumar, and P. A. Ramachandran, “An operator splitting-radial basis function method for the solution of transient nonlinear Poisson problems”, *Comput. Math. Appl.* **43**:3–5 (2002), 289–304.
- [Bogomolny 1985] A. Bogomolny, “Fundamental solutions method for elliptic boundary value problems”, *SIAM J. Numer. Anal.* **22**:4 (1985), 644–669.
- [Burgess and Mahajerin 1984] G. Burgess and E. Mahajerin, “A comparison of the boundary element and superposition methods”, *Comput. Struct.* **19**:5–6 (1984), 697–705.
- [Burgess and Mahajerin 1987] G. Burgess and E. Mahajerin, “The fundamental collocation method applied to the nonlinear Poisson equation in two dimensions”, *Comput. Struct.* **27**:6 (1987), 763–767.
- [Chen 1995] C. S. Chen, “The method of fundamental solutions for non-linear thermal explosions”, *Commun. Numer. Methods Eng.* **11**:8 (1995), 675–681.
- [Chhabra and Richardson 2008] R. P. Chhabra and J. F. Richardson, *Non-Newtonian flow and applied rheology: engineering applications*, 2nd ed., Butterworth-Heinemann, Oxford, 2008.
- [Fairweather and Karageorghis 1998] G. Fairweather and A. Karageorghis, “The method of fundamental solutions for elliptic boundary value problems”, *Adv. Comput. Math.* **9**:1–2 (1998), 69–95.

- [Fairweather et al. 2003] G. Fairweather, A. Karageorghis, and P. A. Martin, “The method of fundamental solutions for scattering and radiation problems”, *Eng. Anal. Bound. Elem.* **27**:7 (2003), 759–769.
- [Fallahi 2012] M. Fallahi, “The quasi-linear method of fundamental solution applied to non-linear wave equations”, *Eng. Anal. Bound. Elem.* **36**:8 (2012), 1183–1188.
- [Fallahi and Hosami 2011] M. Fallahi and M. Hosami, “The quasi-linear method of fundamental solution applied to transient non-linear Poisson problems”, *Eng. Anal. Bound. Elem.* **35**:3 (2011), 550–554.
- [Feng et al. 2013] P.-y. Feng, N. Ma, and X.-c. Gu, “Application of method of fundamental solutions in solving potential flow problems for ship motion prediction”, *J. Shanghai Jiaotong Univ. (Sci.)* **18**:2 (2013), 153–158.
- [Golberg et al. 1998] M. A. Golberg, C. S. Chen, H. Bowman, and H. Power, “Some comments on the use of Radial Basis Functions in the Dual Reciprocity Method”, *Comput. Mech.* **21**:2 (1998), 141–148.
- [Hu and Yeh 2009] H.-P. Hu and R.-H. Yeh, “Theoretical study of the laminar flow in a channel with moving bars”, *J. Fluid. Eng. (ASME)* **131**:11 (2009), 111102.
- [Irgens 2014] F. Irgens, *Rheology and non-Newtonian fluids*, Springer, Heidelberg, 2014.
- [Johnson 1987] D. Johnson, “Plate blending by a boundary point method”, *Comput. Struct.* **26**:4 (1987), 673–680.
- [Karageorghis and Fairweather 1989] A. Karageorghis and G. Fairweather, “The method of fundamental solutions for the solution of nonlinear plane potential problems”, *IMA J. Numer. Anal.* **9**:2 (1989), 231–242.
- [Karageorghis and Lesnic 2008a] A. Karageorghis and D. Lesnic, “The method of fundamental solutions for steady-state heat conduction in nonlinear materials”, *Commun. Comput. Phys.* **4**:4 (2008), 911–928.
- [Karageorghis and Lesnic 2008b] A. Karageorghis and D. Lesnic, “Steady-state nonlinear heat conduction in composite materials using the method of fundamental solutions”, *Comput. Methods Appl. Mech. Eng.* **197**:33–40 (2008), 3122–3137.
- [Karageorghis et al. 2011] A. Karageorghis, D. Lesnic, and L. Marin, “A survey of applications of the MFS to inverse problems”, *Inverse Probl. Sci. Eng.* **19**:3 (2011), 309–336.
- [Klekiel and Kołodziej 2006] T. Klekiel and J. A. Kołodziej, “Trefftz method for large deflection of plates with application of evolutionary algorithms”, *CAMES* **13**:3 (2006), 407–416.
- [Kołodziej and Gorzelańczyk 2012] J. A. Kołodziej and P. Gorzelańczyk, “Application of method of fundamental solutions for elasto-plastic torsion of prismatic rods”, *Eng. Anal. Bound. Elem.* **36**:2 (2012), 81–86.
- [Kołodziej and Mierzwiczak 2008] J. A. Kołodziej and M. Mierzwiczak, “The application of method of fundamental solutions to a simulation of the two-dimensional sloshing phenomenon”, *J. Mech. Mater. Struct.* **3**:6 (2008), 1087–1095.
- [Kołodziej and Uściłowska 2012] J. A. Kołodziej and A. Uściłowska, “Application of MFS for determination of effective thermal conductivity of unidirectional composites with linearly temperature dependent conductivity of constituents”, *Eng. Anal. Bound. Elem.* **36**:3 (2012), 293–302.
- [Kołodziej and Zieliński 2009] J. A. Kołodziej and A. P. Zieliński, *Boundary collocation techniques and their application in engineering*, WIT, Southampton, UK, 2009.
- [Kołodziej et al. 2013] J. A. Kołodziej, M. A. Jankowska, and M. Mierzwiczak, “Meshless methods for inverse problem related to the determination of elastoplastic properties from the torsional experiment”, *Int. J. Solids Struct.* **50**:25–26 (2013), 4217–4225.
- [Kostic 1993] M. Kostic, “Influence of viscosity function simplification on non-Newtonian velocity and shear-rate profiles in rectangular ducts”, *Int. Commun. Heat Mass* **20**:4 (1993), 515–525.
- [Kupradze and Aleksidze 1964] V. D. Kupradze and M. A. Aleksidze, “Метод функциональных уравнений для приближенного решения некоторых граничных задач”, *Ž. Vyčisl. Mat. i Mat. Fiz.* **4** (1964), 683–715. Translated as “The method of functional equations for the approximate solution of certain boundary value problems” in *USSR Comput. Math. Math. Phys.* **4**:4 (1964), 82–126.
- [Li and Zhu 2009] X. Li and J. Zhu, “The method of fundamental solutions for nonlinear elliptic problems”, *Eng. Anal. Bound. Elem.* **33**:3 (2009), 322–329.
- [Li et al. 2014] M. Li, C. S. Chen, C. C. Chu, and D. L. Young, “Transient 3D heat conduction in functionally graded materials by the method of fundamental solutions”, *Eng. Anal. Bound. Elem.* **45** (2014), 62–67.

- [Lima et al. 2000] J. A. Lima, L. M. Pereira, E. N. Macedo, C. L. Chaves, and J. N. N. Quaresma, “Hybrid solution for the laminar flow of power-law fluids inside rectangular ducts”, *Comput. Mech.* **26** (2000), 490–496.
- [Liu et al. 1988] T.-J. Liu, H.-M. Lin, and C.-N. Hong, “Comparison of two numerical methods for the solution of non-Newtonian flow in ducts”, *Int. J. Numer. Methods Fluids* **8**:7 (1988), 845–861.
- [Madhav and Malin 1997] M. T. Madhav and M. R. Malin, “The numerical simulation of fully developed duct flows”, *Appl. Math. Model.* **21**:8 (1997), 503–507.
- [Marin and Lesnic 2007] L. Marin and D. Lesnic, “The method of fundamental solutions for nonlinear functionally graded materials”, *Int. J. Solids Struct.* **44** (2007), 6878–6890.
- [Mathon and Johnston 1977] R. Mathon and R. L. Johnston, “The approximate solution of elliptic boundary-value problems by fundamental solutions”, *SIAM J. Numer. Anal.* **14**:4 (1977), 638–650.
- [de Mey 1978] G. de Mey, “Integral equation for potential problems with the source function not located on the boundary”, *Comput. Struct.* **8**:1 (1978), 113–115.
- [Mierzwiczak and Kołodziej 2011] M. Mierzwiczak and J. A. Kołodziej, “The determination temperature-dependent thermal conductivity as inverse steady heat conduction problem”, *Int. J. Heat Mass Transf.* **54**:4 (2011), 790–796.
- [Mollazadeh et al. 2011] M. Mollazadeh, M. J. Khanjani, and A. Tavakoli, “Applicability of the method of fundamental solutions to interaction of fully nonlinear water waves with a semi-infinite floating ice plate”, *Cold Reg. Sci. Technol.* **69**:1 (2011), 52–58.
- [Ng and Wang 2010] C.-O. Ng and C.-Y. Wang, “Darcy–Brinkman flow through a corrugated channel”, *Transp. Porous Media* **85**:2 (2010), 605–618.
- [Palit and Fenner 1972] K. Palit and R. T. Fenner, “Finite element analysis of slow non-Newtonian channel flow”, *AIChE J.* **18**:3 (1972), 628–633.
- [Schechter 1961] R. S. Schechter, “On the steady flow of a non-Newtonian fluid in cylinder”, *AIChE J.* **7**:3 (1961), 445–448.
- [Sparrow and Loeffler 1959] E. M. Sparrow and A. L. Loeffler, Jr., “Longitudinal laminar flow between cylinders arranged in regular array”, *AIChE J.* **5**:3 (1959), 325–330.
- [Syrjälä 1995] S. Syrjälä, “Finite-element analysis of fully developed laminar flow of power-law non-Newtonian fluid in a rectangular duct”, *Int. Commun. Heat Mass* **22**:4 (1995), 549–557.
- [Tien et al. 2012] W.-K. Tien, R.-H. Yeh, and J.-C. Hsiao, “Numerical analysis of laminar flow and heat transfer in internally finned tubes”, *Head Transf. Eng.* **33**:11 (2012), 957–971.
- [Tri et al. 2011] A. Tri, H. Zahrouni, and M. Potier-Ferry, “Perturbation technique and method of fundamental solution to solve nonlinear Poisson problems”, *Eng. Anal. Bound. Elem.* **35**:3 (2011), 273–278.
- [Tri et al. 2012] A. Tri, H. Zahrouni, and M. Potier-Ferry, “High order continuation algorithm and meshless procedures to solve nonlinear Poisson problems”, *Eng. Anal. Bound. Elem.* **36**:11 (2012), 1705–1714.
- [Tsai 2012] C.-C. Tsai, “Homotopy method of fundamental solutions for solving certain nonlinear partial differential equations”, *Eng. Anal. Bound. Elem.* **36**:8 (2012), 1226–1234.
- [Uściłowska and Berendt 2013] A. Uściłowska and D. Berendt, “An implementation of the method of fundamental solutions for the dynamic response of von Karman nonlinear plate model”, *Int. J. Comput. Methods* **10**:2 (2013), 1341005.
- [Uściłowska and Kołodziej 2006] A. Uściłowska and J. A. Kołodziej, “Solution of the nonlinear equation for isothermal gas flows in porous medium by Trefftz method”, *CAMES* **13**:3 (2006), 445–456.
- [Wang 1976] C. Y. Wang, “Parallel flow between corrugated plates”, *J. Eng. Mech. (ASCE)* **102**:6 (1976), 1088–1099.
- [Wang 1994] C. Y. Wang, “Flow in a channel with longitudinal ribs”, *J. Fluid. Eng. (ASME)* **116**:2 (1994), 233–237.
- [Wang and Qin 2006] H. Wang and Q.-H. Qin, “A meshless method for generalized linear or nonlinear Poisson-type problems”, *Eng. Anal. Bound. Elem.* **30**:6 (2006), 515–521.
- [Wang and Qin 2008] H. Wang and Q.-H. Qin, “Meshless approach for thermo-mechanical analysis of functionally graded materials”, *Eng. Anal. Bound. Elem.* **32**:9 (2008), 704–712.
- [Wang et al. 2005] H. Wang, Q.-H. Qin, and Y.-L. Kang, “A new meshless method for steady-state heat conduction problems in anisotropic and inhomogeneous media”, *Arch. Appl. Mech.* **74**:8 (2005), 563–579.

- [Wang et al. 2006] H. Wang, Q.-H. Qin, and Y.-L. Kang, “A meshless model for transient heat conduction in functionally graded materials”, *Comput. Mech.* **38**:1 (2006), 51–60.
- [Wang et al. 2012] H. Wang, Q.-H. Qin, and X.-P. Liang, “Solving the nonlinear Poisson-type problems with F-Trefftz hybrid finite element model”, *Eng. Anal. Bound. Elem.* **36**:1 (2012), 39–46.
- [Wearing and Sheikh 1988] J. L. Wearing and M. A. Sheikh, “A regular indirect boundary element method for thermal analysis”, *Int. J. Numer. Methods Eng.* **25**:2 (1988), 495–515.
- [Wheeler and Wissler 1965] J. A. Wheeler and E. H. Wissler, “The friction factor–Reynolds number relation for steady flow of pseudoplastic fluids through rectangular ducts, I: Theory”, *AIChE J.* **11**:2 (1965), 207–212.
- [Wu and Tsay 2009] N.-J. Wu and T.-K. Tsay, “Applicability of the method of fundamental solutions to 3-D wave–body interaction with fully nonlinear free surface”, *J. Eng. Math.* **63**:1 (2009), 61–78.
- [Wu et al. 2006] N.-J. Wu, T.-K. Tsay, and D. L. Young, “Meshless numerical simulation for fully nonlinear water waves”, *Int. J. Numer. Methods Fluids* **50**:2 (2006), 219–234.
- [Wu et al. 2008] N.-J. Wu, T.-K. Tsay, and D. L. Young, “Computation of nonlinear free-surface flows by a meshless numerical method”, *J. Waterw. Port Coast. Ocean Eng. (ASCE)* **134**:2 (2008), 97–103.
- [Yin and Fung 1971] F. C. P. Yin and Y. C. Fung, “Comparison of theory and experiment in peristaltic transport”, *J. Fluid Mech.* **47**:1 (1971), 93–112.
- [Young et al. 2008] D. L. Young, C. M. Fan, S. P. Hu, and S. N. Atluri, “The Eulerian–Lagrangian method of fundamental solutions for two-dimensional unsteady Burgers’ equations”, *Eng. Anal. Bound. Elem.* **32**:5 (2008), 395–412.
- [Young et al. 2009] D. L. Young, Y. C. Lin, C. M. Fan, and C. L. Chiu, “The method of fundamental solutions for solving incompressible Navier–Stokes problems”, *Eng. Anal. Bound. Elem.* **33**:8–9 (2009), 1031–1044.
- [Zarling 1976] J. P. Zarling, “An analysis of laminar flow and pressure drop in complex shaped ducts”, *J. Fluid. Eng. (ASME)* **96**:4 (1976), 702–706.
- [Zimmerer et al. 2002] C. Zimmerer, P. Gschwind, G. Gaiser, and V. Kottke, “Comparison of heat and mass transfer in different heat exchanger geometries with corrugated walls”, *Exp. Therm. Fluid Sci.* **26**:2–4 (2002), 269–273.

Received 17 Aug 2014. Revised 20 Mar 2015. Accepted 6 Apr 2015.

JAKUB KRZYSZTOF GRABSKI: jakub.grabski@put.poznan.pl

Institute of Applied Mechanics, Poznań University of Technology, Jana Pawła II 24, 60-965 Poznań, Poland

JAN ADAM KOŁODZIEJ: jan.kolodziej@put.poznan.pl

Institute of Applied Mechanics, Poznań University of Technology, Jana Pawła II 24, 60-965 Poznań, Poland

A STUDY OF ELASTIC-PLASTIC DEFORMATION IN THE PLATE WITH THE INCREMENTAL THEORY AND THE MESHLESS METHODS

MALGORZATA A. JANKOWSKA AND JAN ADAM KOŁODZIEJ

The paper concerns an application of the successive-approximation iteration process together with the meshless methods, i.e., the method of fundamental solutions (MFS) and the method of particular solutions (MPS), for the analysis of strains and stresses in the plate with some kind of narrowing subjected to uniaxial tension. The elastoplastic boundary-value problem is based on the incremental theory of plasticity with the stress-strain relation given in the form proposed by Chakrabarty. In the iteration procedure a sequence of the successive distributions of the plastic strain increments corresponding to the appropriate increments of load is produced. A final set of the plastic strain increments is further used to obtain the total plastic strains. Furthermore, the solution of the elastoplastic boundary-value problem can be simultaneously taken into account when the stress state of the plate is required. Such approach is designated here to identify the regions of elastic and plastic behavior of the material.

1. Introduction

The most popular and commonly used method for solving the elastoplastic problems is the finite element method (FEM). There are many papers on this subject (see, e.g., [Berezhnoĭ and Paĭmushin 2011; Bilotta and Casciaro 2007; Cui et al. 2009; Liu et al. 2013; 2012]) as well as the available monographs (see, e.g., [Belytschko et al. 2000; Crisfield 1997; Kojić and Bathe 2005; Owen and Hinton 1980]). A numerical method that is much less employed for this class of problems is the boundary element method (BEM). Nevertheless, the number of publications on this topic is quite extensive and new ones are still emerging [Deng et al. 2011; Gao and Davies 2000; Ochiai 2011]. We can also distinguish a coupling of these two approaches in, e.g., [Boumaiza and Aour 2014; Dong and Bonnet 1998; Oysu and Fenner 2006]. Note that all these methods require some kind of mesh to be prepared, and hence they are called mesh methods. As an alternative approach for the mesh methods, the mesh-free methods have been developed in the last decades. The meshless methods have been also applied for solving some elastic-plastic problems [Boudaia et al. 2009; Dai et al. 2006; Liu et al. 2011; Pozo et al. 2009; Yeon and Youn 2005]. Nowadays, many different variants of these methods are studied. We have, e.g., the element-free Galerkin method, the meshless local Petrov–Galerkin method, the point interpolation method, the finite point method, the finite difference method with arbitrary irregular grids, and so forth [Liu 2003]. The method of fundamental solutions (MFS) and the method of particular solutions (MPS), subsequently used by the authors, are both the meshfree methods. The main idea of the MFS is that an approximate solution of

The work of Jankowska was supported by the Poznan University of Technology (Poland) through Grants No. 02/21/DSPB/3453 and 02/21/DSPB/3463. The work of Kołodziej was supported by Grant No. 2012/07/B/ST8/03449 founded by the Polish National Science Center (NCN).

Keywords: meshless methods, method of fundamental solutions, successive-approximation iteration process, elastic-plastic deformation, incremental theory.

a given problem is formulated as a linear combination of fundamental solutions related to a governing equation that is linear and homogeneous. Hence, if the appropriate fundamental solutions are known, we obtain an approximate solution that satisfies a governing differential equation and only boundary conditions are approximately met. On the other hand, the MPS can be applied for the boundary value problems with linear nonhomogeneous governing equations. As is described in detail in, e.g., [Chen et al. 2014], a solution of such a problem is a sum of so-called homogeneous solution and particular solution. Nowadays, there is a number of review papers that report on an application of the MFS for solving some elliptic problems [Fairweather and Karageorghis 1998], wave scattering problems [Fairweather et al. 2003] and inverse problems [Karageorghis et al. 2011]. On the other hand, there are still few papers that conduct a review on the usage of the MFS for solving nonlinear problems. An application of the method considered for nonlinear problems is quite popular in the area of fluid mechanics and there are many papers that take into account this issue. Namely, for a governing equation given in a form of Burgers' equation we have [Young et al. 2008], similarly as for the Navier–Stokes equation [Young et al. 2009] and for nonlinear water waves [Feng et al. 2013; Mollazadeh et al. 2011]. A solution of a boundary value problem governed by a nonlinear Poisson equation is presented in, e.g., [Balakrishnan and Ramachandran 1999; 2001; Balakrishnan et al. 2002; Burgess and Mahajerin 1987; Fallahi and Hosami 2011; Shanazari and Fallahi 2010; Tri et al. 2011; Tsai 2012; Wang and Qin. 2006; Wang et al. 2012]. Further, in [Chen 1995] the nonlinear thermal explosion problem by solving some nonlinear equation is taken into consideration. An application of the MFS for nonlinear functionally graded materials is given in [Li et al. 2014; Marin and Lesnic 2007; Wang and Qin. 2008; Wang et al. 2005], while the nonlinear heat conduction problems solved by the MFS are presented in [Karageorghis and Fairweather 1989; Karageorghis and Lesnic 2008]. Finally, nonlinear plate problems as well as an application of the MFS for nonlinear elasticity is reported in [Al-Gahtani 2012; Li and Zhu 2009; Uscilowska and Berendt 2013]. For the authors' best knowledge there are few papers such that the MFS with the MPS are applied to study elastic-plastic deformation. These articles deal with the torsion problem [Kołodziej et al. 2013] and the plane problem for the stress state of a plate subjected to uniaxial extension [Jankowska and Kołodziej 2015].

Subsequent considerations are directed forward further popularization and dissemination of the meshless methods for solving some nonlinear boundary-value problems with a special attention that is paid to elastoplastic problems. The authors based their research on the approach proposed in [Mendelson 1968]. It takes into account the incremental theory of plasticity together with the associated flow rule given by the Prandtl–Reuss relation and the von Mises yield criterion to formulate the appropriate elastoplastic plane stress problem (see Section 2). The appropriate boundary conditions concern a problem of uniaxial tension of a plate with a narrowing located in the middle of it (see also [Jankowska and Kołodziej 2014; Jankowska and Kołodziej 2013]). Then, for the nonlinear stress-strain relationship, we apply a model presented by Chakrabarty in [Chakrabarty 1987]. In Section 3 a new approach to the successive-approximation iteration process [Mendelson 1968] is proposed. It employs a combination of the meshless methods (the MFS-MPS) and the finite difference schemes (required for the approximation of values of partial derivatives present in the right-hand side function of the problem). In the appropriate algorithm, a sequence of the successive distributions of the plastic strain increments, corresponding to a given increment of load, is produced. A final set of the plastic strain increments can be used to obtain the total plastic strains. Then, the solution of the boundary-value problem let us determine the stress state of

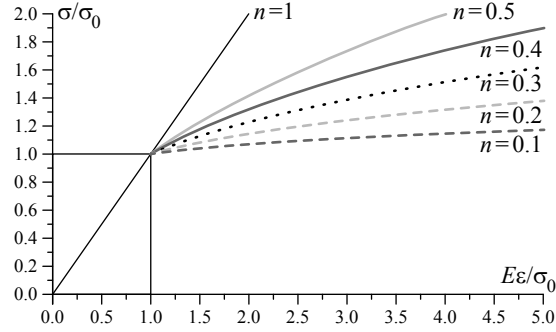


Figure 1. The stress-strain curve for the model proposed by Chakrabarty [1987] with selected values of n .

the plate. In Section 4, the optimal values of the method's parameters are proposed and the regions of the elastic and plastic behavior of the material are shown. The approach enables to compute the equivalent plastic strains and also related equivalent stresses in any point of the domain. It is due to the fact that the approximate solution is a linear combination of fundamental solutions and particular solutions, i.e., a continuous function with continuous derivatives. To conclude, some final remarks and further plans are summarized in Section 5.

2. Problem formulation

2.1. Assumptions about the elastic-plastic constitutive model and the complete stress-strain relations.

The consideration given in the paper concerns some plane elastoplastic problem formulated for a plate with a narrowing subjected to external loads related to the uniaxial stress σ_B . We assume that the material is homogenous, isotropic and strains hardens isotropically. The material properties such as the Young modulus E and the Poisson ratio ν are independent of the temperature and body forces are not considered. For the nonlinear stress-strain relationship we employ a model proposed by Chakrabarty [1987]. It is given by the equations

$$\sigma/\sigma_0 = \begin{cases} \varepsilon/\varepsilon_0, & \varepsilon/\varepsilon_0 \leq 1, \\ (\varepsilon/\varepsilon_0)^n, & \varepsilon/\varepsilon_0 \geq 1. \end{cases} \quad (1)$$

Note that the curve in the plastic range is expressed by a simple power law (see also Figure 1) with a dimensionless constant n such that its value is generally less than 0.5. The material is assumed to have a definite yield point for the stress σ_0 with the corresponding yield strain $\varepsilon_0 = \sigma_0/E$, where E is the Young modulus. Furthermore, the slope of the stress-strain curve changes discontinuously at the yield point (except for the case of $n = 1$).

The subsequent considerations are presented with the incremental theory of plasticity applied (see, e.g., [Mendelson 1968]). Hence, we assume some loading path to a given state of stress and the total plastic strain. The total loading path is divided into N increments of load. When the load is increased by a small amount, it produces additional plastic strain $\Delta\varepsilon_{ij}^p$. Following, e.g., [Mendelson 1968], the total strain ε_{ij} can be written as

$$\varepsilon_{ij} = \varepsilon_{ij}^e + \varepsilon_{ij}^p + \Delta\varepsilon_{ij}^p, \quad (2)$$

where ε_{ij}^e is the elastic component of the strain, ε_{ij}^p is the accumulated plastic strain up to (but not including) the current increment of load and $\Delta\varepsilon_{ij}^p$ is the increment of plastic strain due to the current increment of load. If we assume that the elastic strain tensor is given by the Hooke's law for isotropic material and the plastic strains have been computed for the first $k-1$ increments of load, then the total strain at the end of the k -th increment of load can be given as follows:

$$\varepsilon_{ij} = \frac{1+\nu}{E}\sigma_{ij} - \frac{\nu}{E}\sigma_{ss}\delta_{ij} + \sum_{m=1}^{k-1} \Delta\varepsilon_{ij,m}^p + \Delta\varepsilon_{ij}^p. \quad (3)$$

In the above equation we know the sum and the problem is how to calculate the plastic strain increment $\Delta\varepsilon_{ij}^p$ (for the current, i.e., the k -th increment of load) and the corresponding stress. Hence, subsequently for the equation (3) we use the stress-strain relation (1), the associated flow rule given by the Prandtl–Reuss relation (4)₁ with the von Mises yield criterion (4)₂. The equivalent stress σ_{eq} , the equivalent plastic strain increment $\Delta\varepsilon_{ij}^p$ and the deviatoric component S_{ij} of the stress tensor are given by the equations

$$\Delta\varepsilon_{ij}^p = \frac{3}{2} \frac{\Delta\varepsilon_{\text{eq}}^p}{\sigma_{\text{eq}}} S_{ij}, \quad \sigma_{\text{eq}} = \sqrt{\frac{3}{2} S_{ij} S_{ij}}, \quad \Delta\varepsilon_{\text{eq}}^p = \sqrt{\frac{2}{3} \Delta\varepsilon_{ij}^p \Delta\varepsilon_{ij}^p}, \quad S_{ij} = \sigma_{ij} - \frac{1}{3}\sigma_{ss}\delta_{ij}. \quad (4)$$

2.2. Plane elastic-plastic boundary-value problem. Now we formulate the boundary-value problem describing the stress state of the plate that is subjected to uniaxial extension related to the stress σ_B . However, before that we expand the equations (3)–(4) with the assumption that the generalized plane stress problem is considered. We obtain the formulas for the components of the total strain (3) as

$$\varepsilon_{xx} = \varepsilon_{xx}^e + \varepsilon_{xx}^p + \Delta\varepsilon_{xx}^p, \quad \varepsilon_{yy} = \varepsilon_{yy}^e + \varepsilon_{yy}^p + \Delta\varepsilon_{yy}^p, \quad \varepsilon_{xy} = \varepsilon_{xy}^e + \varepsilon_{xy}^p + \Delta\varepsilon_{xy}^p, \quad (5)$$

where

$$\varepsilon_{xx}^e = \frac{1}{E}(\sigma_{xx} - \mu\sigma_{yy}), \quad \varepsilon_{yy}^e = \frac{1}{E}(\sigma_{yy} - \mu\sigma_{xx}), \quad \varepsilon_{xy}^e = \frac{1}{2G}\sigma_{xy}, \quad (6)$$

$$\varepsilon_{xx}^p = \sum_{m=1}^{k-1} \Delta\varepsilon_{xx,m}^p, \quad \varepsilon_{yy}^p = \sum_{m=1}^{k-1} \Delta\varepsilon_{yy,m}^p, \quad \varepsilon_{xy}^p = \sum_{m=1}^{k-1} \Delta\varepsilon_{xy,m}^p. \quad (7)$$

Then, the expanded formulas for the Prandtl–Reuss relations (4)₁ with the equivalent stress (4)₂ and the equivalent plastic strain increments (4)₃ are of the form (see also [Mendelson 1968])

$$\Delta\varepsilon_{xx}^p = \frac{1}{2} \frac{\Delta\varepsilon_{\text{eq}}^p}{\sigma_{\text{eq}}} (2\sigma_{xx} - \sigma_{yy}), \quad \Delta\varepsilon_{yy}^p = \frac{1}{2} \frac{\Delta\varepsilon_{\text{eq}}^p}{\sigma_{\text{eq}}} (2\sigma_{yy} - \sigma_{xx}), \quad \Delta\varepsilon_{xy}^p = \frac{3}{2} \frac{\Delta\varepsilon_{\text{eq}}^p}{\sigma_{\text{eq}}} \sigma_{xy}, \quad (8)$$

and

$$\sigma_{\text{eq}} = \sqrt{\sigma_{xx}^2 + \sigma_{yy}^2 - \sigma_{xx}\sigma_{yy} + 3\sigma_{xy}^2}, \quad \Delta\varepsilon_{\text{eq}}^p = \frac{2}{\sqrt{3}} \sqrt{(\Delta\varepsilon_{xx}^p)^2 + (\Delta\varepsilon_{yy}^p)^2 + \Delta\varepsilon_{xx}^p \Delta\varepsilon_{yy}^p + (\Delta\varepsilon_{xy}^p)^2}. \quad (9)$$

Subsequently, we take into consideration the boundary-value problem as proposed in [Mendelson 1968]. For its formulation the components of the total strain (5) with the relations (6)–(7) are substituted into the compatibility and equilibrium equations for the plane problems (see, e.g., [Mendelson 1968];

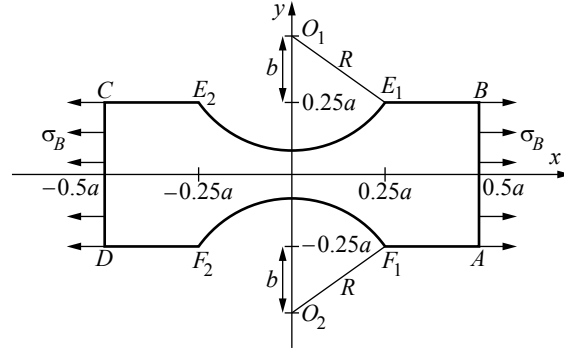


Figure 2. A plate with a narrowing subjected to uniaxial extension related to the stress σ_B (reprinted from [Jankowska and Kołodziej 2015] with permission from Elsevier).

Timoshenko and Goodier 1951]). Then, with the Airy stress function $\psi = \psi(x, y)$ (see also [Timoshenko and Goodier 1951]) such that

$$\sigma_{xx} = \frac{\partial^2 \psi}{\partial y^2}(x, y), \quad \sigma_{yy} = \frac{\partial^2 \psi}{\partial x^2}(x, y), \quad \sigma_{xy} = -\frac{\partial^2 \psi}{\partial x \partial y}(x, y), \quad (10)$$

we obtain the governing equation of the problem considered

$$\nabla^4 \psi(x, y) = -(g(x, y) + \Delta g(x, y)), \quad (11)$$

where

$$g(x, y) = E \left(\frac{\partial^2 \varepsilon_{xx}^p}{\partial y^2} + \frac{\partial^2 \varepsilon_{yy}^p}{\partial x^2} - 2 \frac{\partial^2 \varepsilon_{xy}^p}{\partial x \partial y} \right), \quad (12)$$

$$\Delta g(x, y) = E \left(\frac{\partial^2 (\Delta \varepsilon_{xx}^p)}{\partial y^2} + \frac{\partial^2 (\Delta \varepsilon_{yy}^p)}{\partial x^2} - 2 \frac{\partial^2 (\Delta \varepsilon_{xy}^p)}{\partial x \partial y} \right).$$

In order to formulate the boundary conditions of the problem, we introduce the geometry of the plate (see Figure 2). It is characterized by the narrowing that occurs in the middle of it and is present along a half of its length. It is specified by the characteristic length a and the distance b such that the appropriate parts of the boundary, i.e., $E_1 E_2$, $F_1 F_2$, are arcs of circles with centers $O_1(0, a/4 + b)$, $O_2(0, -a/4 - b)$ and a radius $R = \sqrt{b^2 + a^2/16}$. The appropriate boundary conditions imposed according to the sides of the plate are given as

$$\Gamma_{AB} \text{ and } \Gamma_{DC} : \quad \psi_{yy} = \sigma_B, \quad \psi_{xy} = 0, \quad (13a)$$

$$\Gamma_{E_1 B}, \Gamma_{E_2 C} \text{ and } \Gamma_{F_1 A}, \Gamma_{F_2 D} : \quad \psi_{xx} = 0, \quad \psi_{xy} = 0, \quad (13b)$$

$$\Gamma_{E_1 E_2}, \Gamma_{F_1 F_2} : \quad \psi_{yy} n_x - \psi_{xy} n_y = 0, \quad \psi_{xx} n_y - \psi_{xy} n_x = 0, \quad (13c)$$

where n_x, n_y are components of a unit vector \mathbf{n} defined at a given point of the boundary, normal to the surface and directed outside of the plate.

Note that in the equations (13a)–(13c) and later in the paper, we use the abbreviated notation for partial derivatives, i.e., $\psi_{xx} = \partial^2 \psi / \partial x^2$, $\psi_{yy} = \partial^2 \psi / \partial y^2$ and $\psi_{xy} = \partial^2 \psi / \partial x \partial y$, respectively.

Subsequently, we solve the elastic-plastic boundary-value problem given in the nondimensional form. Hence, with new coordinates defined by

$$X = x/a, \quad Y = y/a, \quad \Psi = \psi/(a^2\sigma_0), \quad (14)$$

the governing equation (11) with (12) is of the form

$$\nabla^4\Psi = \tilde{b}(X, Y), \quad (15)$$

with the boundary conditions

$$\Gamma_{AB} \text{ and } \Gamma_{DC} : \quad \Psi_{YY} = \tilde{\sigma}_B, \quad \Psi_{XY} = 0, \quad (16a)$$

$$\Gamma_{E_1B}, \Gamma_{E_2C} \text{ and } \Gamma_{F_1A}, \Gamma_{F_2D} : \quad \Psi_{XX} = 0, \quad \Psi_{XY} = 0, \quad (16b)$$

$$\Gamma_{E_1E_2}, \Gamma_{F_1F_2} : \quad \Psi_{YY}n_x - \Psi_{XY}n_y = 0, \quad \Psi_{XX}n_y - \Psi_{XY}n_x = 0, \quad (16c)$$

where $\tilde{\sigma}_B = \sigma_B/\sigma_0$ and

$$\tilde{b}(X, Y) = -(\tilde{g}(X, Y) + \Delta\tilde{g}(X, Y)), \quad (17)$$

$$\tilde{g}(X, Y) = \left(\frac{\partial^2 \varepsilon_{XX}^p}{\partial Y^2} + \frac{\partial^2 \varepsilon_{YY}^p}{\partial X^2} - 2 \frac{\partial^2 \varepsilon_{XY}^p}{\partial X \partial Y} \right), \quad (18)$$

$$\Delta\tilde{g}(X, Y) = \left(\frac{\partial^2 (\Delta\varepsilon_{XX}^p)}{\partial Y^2} + \frac{\partial^2 (\Delta\varepsilon_{YY}^p)}{\partial X^2} - 2 \frac{\partial^2 (\Delta\varepsilon_{XY}^p)}{\partial X \partial Y} \right). \quad (19)$$

The dimensionless plastic strains $\varepsilon_{XX}^p = \varepsilon_{xx}^p/\varepsilon_0$, $\varepsilon_{YY}^p = \varepsilon_{yy}^p/\varepsilon_0$ and $\varepsilon_{XY}^p = \varepsilon_{xy}^p/\varepsilon_0$, present in (18), are given by the formulas

$$\varepsilon_{XX}^p = \sum_{m=1}^{k-1} \Delta\varepsilon_{XX,m}^p, \quad \varepsilon_{YY}^p = \sum_{m=1}^{k-1} \Delta\varepsilon_{YY,m}^p, \quad \varepsilon_{XY}^p = \sum_{m=1}^{k-1} \Delta\varepsilon_{XY,m}^p, \quad (20)$$

where the dimensionless increments of plastic strains used in (19)–(20) are defined as $\Delta\varepsilon_{XX}^p = \Delta\varepsilon_{xx}^p/\varepsilon_0$, $\Delta\varepsilon_{YY}^p = \Delta\varepsilon_{yy}^p/\varepsilon_0$ and $\Delta\varepsilon_{XY}^p = \Delta\varepsilon_{xy}^p/\varepsilon_0$, respectively. Further, with the dimensionless Airy stress function $\Psi = \Psi(X, Y)$ applied, the dimensionless total strains and the elastic strains, are of the form

$$\varepsilon_{XX} = \varepsilon_{XX}^e + \varepsilon_{XX}^p + \Delta\varepsilon_{XX}^p, \quad \varepsilon_{YY} = \varepsilon_{YY}^e + \varepsilon_{YY}^p + \Delta\varepsilon_{YY}^p, \quad \varepsilon_{XY} = \varepsilon_{XY}^e + \varepsilon_{XY}^p + \Delta\varepsilon_{XY}^p, \quad (21)$$

$$\varepsilon_{XX}^e = \Psi_{YY} - \mu\Psi_{XX}, \quad \varepsilon_{YY}^e = \Psi_{XX} - \mu\Psi_{YY}, \quad \varepsilon_{XY}^e = -(1 + \mu)\Psi_{XY}, \quad (22)$$

where $\varepsilon_{XX} = \varepsilon_{xx}/\varepsilon_0$, $\varepsilon_{YY} = \varepsilon_{yy}/\varepsilon_0$, $\varepsilon_{XY} = \varepsilon_{xy}/\varepsilon_0$, $\varepsilon_{XX}^e = \varepsilon_{xx}^e/\varepsilon_0$, $\varepsilon_{YY}^e = \varepsilon_{yy}^e/\varepsilon_0$, $\varepsilon_{XY}^e = \varepsilon_{xy}^e/\varepsilon_0$.

Note that for the algorithm proposed in Section 3 that is designed for solving the boundary value equation (15)–(16) with (17)–(19), the dimensionless Prandtl–Reuss relations are also required. Hence, from the formula (8) we obtain

$$\Delta\varepsilon_{XX}^p = \frac{1}{2} \frac{\Delta\tilde{\varepsilon}_{\text{eq}}^p}{\tilde{\sigma}_{\text{eq}}} (2\sigma_{XX} - \sigma_{YY}), \quad \Delta\varepsilon_{YY}^p = \frac{1}{2} \frac{\Delta\tilde{\varepsilon}_{\text{eq}}^p}{\tilde{\sigma}_{\text{eq}}} (2\sigma_{YY} - \sigma_{XX}), \quad \Delta\varepsilon_{XY}^p = \frac{3}{2} \frac{\Delta\tilde{\varepsilon}_{\text{eq}}^p}{\tilde{\sigma}_{\text{eq}}} \sigma_{XY}, \quad (23)$$

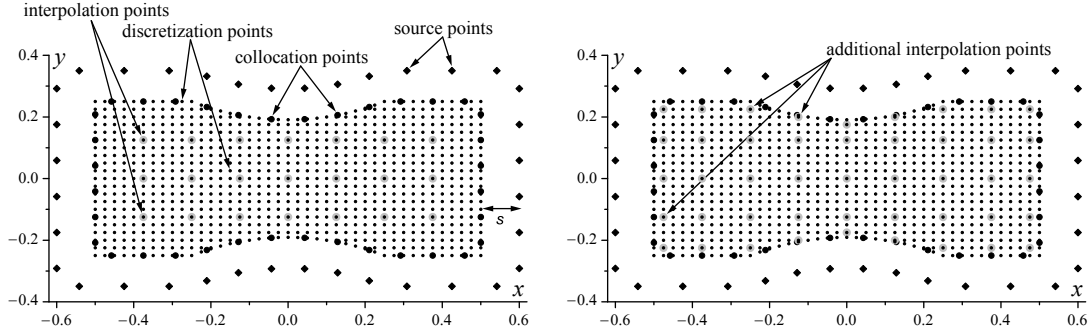


Figure 3. The distribution of the source, collocation, interpolation and discretization points.

where the dimensionless equivalent stress $\tilde{\sigma}_{\text{eq}} = \sigma_{\text{eq}}/\sigma_0$ and the dimensionless equivalent plastic strain increments $\Delta\tilde{\varepsilon}_{\text{eq}}^p$ are of the form

$$\tilde{\sigma}_{\text{eq}} = \sqrt{\sigma_{XX}^2 + \sigma_{YY}^2 - \sigma_{XX}\sigma_{YY} + 3\sigma_{XY}^2}, \quad (24)$$

$$\Delta\tilde{\varepsilon}_{\text{eq}}^p = \frac{2}{\sqrt{3}} \sqrt{(\Delta\varepsilon_{XX}^p)^2 + (\Delta\varepsilon_{YY}^p)^2 + \Delta\varepsilon_{XX}^p \Delta\varepsilon_{YY}^p + (\Delta\varepsilon_{XY}^p)^2}. \quad (25)$$

The dimensionless stress components used in (24) are defined as $\sigma_{XX} = \sigma_{xx}/\sigma_0$, $\sigma_{YY} = \sigma_{yy}/\sigma_0$, $\sigma_{XY} = \sigma_{xy}/\sigma_0$.

3. The successive-approximation iteration process and the meshless methods

Subsequently, we propose two algorithms that concern the solution of the boundary-value equation (15)–(16) with (17)–(19). The first one deals with a case when the whole region of the plate corresponds to the elastic behavior of the material. We propose the iteration process that proceeds until (for a given increment of load) the first points such that the plastic behavior of the material occurs. After that we can start the other two nested iteration processes described in detail in the second algorithm. The procedure proposed there let us determine the distribution of the plastic strain increments corresponding to a given conditions of loading. Moreover, the elastic and plastic strains and the stress state at each point of the plate can be also computed.

Note that both algorithms make use of the meshless methods (in each iteration step), i.e., the method of fundamental solutions and the method of particular solutions that is applied only in the Algorithm 2. Due to this reason we first generate some sets of points [Chen et al. 2014] that are required for the meshless methods (see also Figure 3, left). We denote by N_s the number of source points (X_{si}, Y_{si}) , $i = 1, 2, \dots, N_s$, that are located outside of the problem domain in a distance s from the boundary. For the numerical experiments they are uniformly distributed on a fictitious boundary similar to the physical one. We also choose the total number N_c of collocation points, (X_i, Y_i) , $i = 1, 2, \dots, N_c$. These points should be located as uniform as possible on the physical domain. Then, for the interpolation procedure of the right-hand side function (17), we select N_i interpolation points, (X_i, Y_i) , $i = 1, 2, \dots, N_i$, that are located inside of the computational domain. They used to be uniformly distributed similarly as the source and collocation points.

Special requirements of the subsequent algorithms make it essential to choose another set of uniformly distributed points, so-called, discretization points, (X_i, Y_i) , $i = 1, 2, \dots, Nd$. This set of points includes all the interpolation points together with some appropriate points located on the boundary (see Figure 3, left). The discretization points are further used for computation of values of partial derivatives present in (18)–(19) at the interpolation points. Note that the distances between two neighboring interpolation points does not have to be very small for the MPS. In fact the number of these points should not be also too large (because it can lead to an ill-conditioned matrix of coefficients further used in the MPS). On the other hand, the accuracy of a finite difference approximation increases when the distance between the points involved in a finite difference formula becomes small enough. Hence, we introduce the number iMd of additional intermediate discretization points that are located between each two interpolation points (see Figure 3, left). All these discretization points are involved in the finite difference approximation. Note that we also increase a number of the interpolation points in such a way that we add to the set considered some selected discretization points located near the boundary (see Figure 3, right). This approach is essential due to the fact that the material starts exhibiting the plastic behavior on the boundary and inside the plate in the neighborhood of the narrowing.

Now, with the assumptions and notations introduced above, the computational procedure can be formulated in the following way.

Algorithm 1 (elastic case). *Assumptions and preliminary steps.* We start from the assumption that the whole region of the plate corresponds to the elastic behavior of the material. Hence, for each iteration step we take $\tilde{b}(X, Y) \equiv 0$ in the governing equation (15). Then, we choose some loading path to a given state of stress, i.e., we take $m = 1, 2, \dots, k_p$ that corresponds to related values of stress $\tilde{\sigma}_B = \tilde{\sigma}_{B1}, \tilde{\sigma}_{B2}, \dots, \tilde{\sigma}_{Bk_p}$, respectively. The iteration step k_p is the last one performed during the algorithm's execution. For $m = k_p$ the material starts exhibiting the plastic behavior.

Step 1. Take $m = 1$ ($\tilde{\sigma}_B = \tilde{\sigma}_{B1}$).

Step 2. For a given value of m ($\tilde{\sigma}_{Bm}$), compute the approximate solution of the boundary value equation (15)–(16) using the MFS. We obtain

$$\Psi(X, Y) \approx \sum_{i=1}^{Ns} c_i \phi_{1i}(X, Y) + \sum_{i=1}^{Ns} d_i \phi_{2i}(X, Y), \quad (26)$$

where the functions $\phi_1 = \phi_1(X, Y)$, $\phi_2 = \phi_2(X, Y)$ are the fundamental solutions related to the homogeneous biharmonic equation $\nabla^4 \Psi = 0$. We have

$$\phi_{1i} = \phi_{1i}(X, Y) = \ln r_i, \quad \phi_{2i} = \phi_{2i}(X, Y) = r_i^2 \ln r_i, \quad r_i = \sqrt{(X - X_{si})^2 + (Y - Y_{si})^2}. \quad (27)$$

Unknown values of the coefficients c_i, d_i , $i = 1, 2, \dots, Ns$, in (26), can be found, if we solve a linear system of equations (28) obtained by collocating the boundary conditions. We get

$$G_{1l}(\Psi(X_j, Y_j)) = g_{1l}(X_j, Y_j), \quad G_{2l}(\Psi(X_j, Y_j)) = g_{2l}(X_j, Y_j), \quad (28)$$

for $l = 1, 2, \dots, Nl$, $j = 1, 2, \dots, Nc(l)$, where Ψ is of the form (26), G_{1l}, G_{2l} are the differential operators acting on Ψ , $g_{1l} = g_{1l}(X, Y)$, $g_{2l} = g_{2l}(X, Y)$ are given functions, Nl denotes the number of characteristic parts of the boundary and $Nc(l)$ denotes the number of collocation points located on a given part l of the boundary.

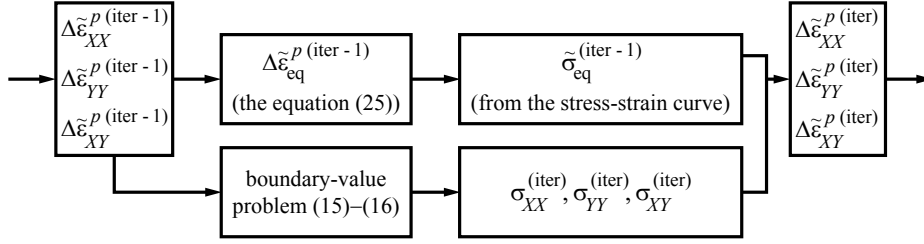


Figure 4. The block diagram [Mendelson 1968] that shows how to compute successive approximations of the plastic strain increments.

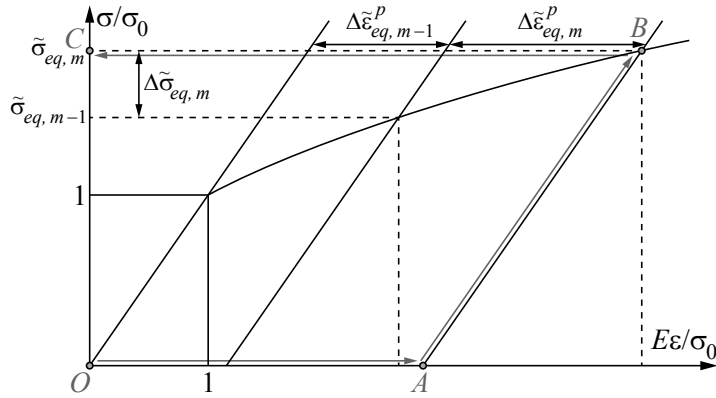


Figure 5. The stress-strain curve with the path $OABC$ [Mendelson 1968] that allows to obtain the equivalent stress $\tilde{\sigma}_{eq}$ from the equivalent plastic strain increment $\Delta \tilde{\varepsilon}_{eq}^p$.

Step 3. Compute the equivalent stress $\tilde{\sigma}_{eq,m}$ (the equation (24)) at each discretization point. Then, check if there exist one or more interpolation points such that $\tilde{\sigma}_{eq,m} > 1$. If so, then finish the execution of the Algorithm 1 and start the Algorithm 2. Else, take $m = m + 1$ ($\tilde{\sigma}_B = \tilde{\sigma}_{Bm}$), go back to Step 2 and continue the iteration process.

Algorithm 2 (elastic-plastic case). *Assumptions and preliminary steps.* On the basis of the results obtained with the Algorithm 1, the elastic-plastic behavior of the material is now considered. Hence, the right-hand side function in the governing equation (15) is no longer equal to zero. The Algorithm 2 consists of two nested iteration processes. In the case of the main iteration process we continue the loading path started by the Algorithm 1, i.e., we take $m = k_p, k_p + 1, \dots$, that corresponds to the stress $\tilde{\sigma}_B = \tilde{\sigma}_{Bk_p}, \tilde{\sigma}_{Bk_p+1}, \dots$, respectively. Note that since for the last iteration step k_p in the Algorithm 1 the elastic-plastic behavior of the material has been detected, then we repeat computations taking $m = k_p$ ($\tilde{\sigma}_B = \tilde{\sigma}_{Bk_p}$) and some initial distribution for the unknown plastic strain increments (further referred by $iter = 0$). Generally, for a given stress $\tilde{\sigma}_{Bm}$, we start the internal iteration process, taking $iter = 1, 2, \dots$. We compute successive approximations $\Delta \varepsilon_{XX}^{p(iter)}, \Delta \varepsilon_{YY}^{p(iter)}, \Delta \varepsilon_{XY}^{p(iter)}$ for the plastic strain increments until a desired accuracy is achieved.

Main iteration process:

Step 1-1. Take $m = k_p$ ($\tilde{\sigma}_B = \tilde{\sigma}_{Bk_p}$).

Step 1-2. For a given value of m ($\tilde{\sigma}_{Bm}$), perform some preliminary steps, before the internal iteration process starts. An initial distribution of plastic strain increments is denoted as $\text{iter} = 0$.

If $m = k_p$, then

- (a) take $\varepsilon_{XX}^p = \varepsilon_{YY}^p = \varepsilon_{XY}^p = 0$ and $\tilde{g}(X_i, Y_i) = 0$, $i = 1, 2, \dots, Ni$;
- (b) choose some initial distribution for the plastic strain increments $\Delta\varepsilon_{XX}^{p(0)}$, $\Delta\varepsilon_{YY}^{p(0)}$, $\Delta\varepsilon_{XY}^{p(0)}$ for all discretization points such that $\tilde{\sigma}_{\text{eq},k_p} > 1$ (the Algorithm 1); for the remaining discretization points, take $\Delta\varepsilon_{XX}^{p(0)} = \Delta\varepsilon_{YY}^{p(0)} = \Delta\varepsilon_{XY}^{p(0)} = 0$.

Else, if $m > k_p$, then

- (a) use a final distribution of the plastic strain increments obtained for the stress $\tilde{\sigma}_{Bm-1}$ to compute current values of ε_{XX}^p , ε_{YY}^p , ε_{XY}^p (the equation (20)) for all interpolation points such that $\tilde{\sigma}_{\text{eq},m-1} > 1$; otherwise, take $\varepsilon_{XX}^p = \varepsilon_{YY}^p = \varepsilon_{XY}^p = 0$;
- (b) compute current values of the function $\tilde{g}(X_i, Y_i)$ (the equation (18)) at all interpolation points such that $\tilde{\sigma}_{\text{eq},m-1} > 1$ (see also the remarks on the finite difference (FD) approximation of the partial derivatives given below); otherwise, take $\tilde{g}(X_i, Y_i) = 0$;
- (c) choose some initial distribution for the plastic strain increments $\Delta\varepsilon_{XX}^{p(0)}$, $\Delta\varepsilon_{YY}^{p(0)}$, $\Delta\varepsilon_{XY}^{p(0)}$ for all discretization points such that $\tilde{\sigma}_{\text{eq},m-1} > 1$; otherwise, take $\Delta\varepsilon_{XX}^{p(0)} = \Delta\varepsilon_{YY}^{p(0)} = \Delta\varepsilon_{XY}^{p(0)} = 0$.

End If

Internal iteration process:

Step 2-1. Take $\text{iter} = 1$.

Step 2-2. Based on a given distribution of the plastic strain increments $\Delta\varepsilon_{XX}^{p(\text{iter}-1)}$, $\Delta\varepsilon_{YY}^{p(\text{iter}-1)}$, $\Delta\varepsilon_{XY}^{p(\text{iter}-1)}$ compute values of the function $\Delta\tilde{g}^{(\text{iter}-1)}(X_i, Y_i)$, $i = 1, 2, \dots, Ni$ (the equation (19); see also the remarks on the FD approximation of the partial derivatives).

Step 2-3. Compute values of the right-hand side function of the governing equation (15), i.e., $\tilde{b}^{(\text{iter}-1)}(X_i, Y_i)$, $i = 1, 2, \dots, Ni$ (the equation (17)).

Step 2-4. Compute the approximate solution of the inhomogeneous boundary value equation (15)–(16) using the MPS together with the MFS (see, e.g., [Chen et al. 2014]).

We represent the solution in a decomposed form as a sum of a particular solution $\Psi_p^{(\text{iter})}(X, Y)$ (see Step 2-4-1) and a general solution $\Psi_h^{(\text{iter})}(X, Y)$ (see Step 2-4-2), i.e.,

$$\Psi^{(\text{iter})}(X, Y) = \Psi_h^{(\text{iter})}(X, Y) + \Psi_p^{(\text{iter})}(X, Y). \quad (29)$$

Step 2-4-1. Compute the particular solution.

The particular solution satisfies the governing equation (15) in the domain, although it does not necessarily satisfy the boundary conditions. We can obtain the approximate particular solution if we interpolate the right-hand side function given in (15) at the interpolation points using radial basis functions (RBFs) φ_k and some polynomial functions p_j (for details see, e.g., [Chen et al. 2014; Jankowska and Kołodziej 2015]). Note that we take the multiquadric (MQ) as RBFs. We have

$$\varphi_k = \sqrt{(X - X_k)^2 + (Y - Y_k)^2 + c^2}, \quad (30)$$

where c is a shape parameter. Hence, we obtain

$$\tilde{b}^{(\text{iter}-1)}(X, Y) \approx \sum_{k=1}^{Ni} \alpha_k \varphi_k(X, Y) + \sum_{j=1}^L \beta_j p_j(X, Y), \quad (31)$$

where L , $0 \leq L \leq 6$, denotes the number of polynomials $p_j = p_j(X, Y)$ in (31). Note that α_k , β_j in (31) are unknown coefficients to be determined. They can be obtained by solving the linear system of equations of the form

$$\begin{aligned} \sum_{k=1}^{Ni} \alpha_k \varphi_k(X_i, Y_i) + \sum_{j=1}^L \beta_j p_j(X_i, Y_i) &= \tilde{b}^{(\text{iter}-1)}(X_i, Y_i), \quad i = 1, 2, \dots, Ni, \\ \sum_{j=1}^{Ni} \alpha_j p_k(X_j, Y_j) &= 0, \quad k = 1, 2, \dots, L. \end{aligned} \quad (32)$$

When the constants α_k and β_j are computed, the approximate particular solution $\Psi_p^{(\text{iter})}(X, Y)$ is of the following form:

$$\Psi_p^{(\text{iter})}(X, Y) \approx \sum_{k=1}^{Ni} \alpha_k \psi_k(X, Y) + \sum_{j=1}^L \beta_j q_j(X, Y), \quad (33)$$

where ψ_k and q_j are the particular solutions corresponding to the functions φ_k and p_j , respectively. Note that they are associated with the operator ∇^4 of the governing equation such that the following equations are satisfied $\nabla^4 \psi_k(X, Y) = \varphi_k(X, Y)$ and $\nabla^4 q_j(X, Y) = p_j(X, Y)$ (for details see, e.g., [Chen et al. 2014; Jankowska and Kołodziej 2015]).

Step 2-4-2. Compute the general solution.

The general solution $\Psi_h^{(\text{iter})}(X, Y)$ satisfies the homogeneous governing equation of the form $\nabla^4 \Psi_h^{(\text{iter})}(X, Y) = 0$ with the modified boundary conditions

$$\begin{aligned} G_{1l}(\Psi_h^{(\text{iter})}(X, Y)) &= g_{1l}(X, Y) - G_{1l}(\Psi_p^{(\text{iter})}(X, Y)), \\ G_{2l}(\Psi_h^{(\text{iter})}(X, Y)) &= g_{2l}(X, Y) - G_{2l}(\Psi_p^{(\text{iter})}(X, Y)), \end{aligned} \quad (34)$$

for $l = 1, 2, \dots, Nl$. The above boundary value problem can be solved with the MFS. The approximate general solution is of the form

$$\Psi_h^{(\text{iter})}(X, Y) \approx \sum_{i=1}^{Ns} c_i \phi_{1i}(X, Y) + \sum_{i=1}^{Ns} d_i \phi_{2i}(X, Y), \quad (35)$$

where the unknown values of coefficients c_i , d_i , $i = 1, 2, \dots, Ns$, present in (35), can be obtained, if we solve a linear system of collocation equations (compare Step 2 of the Algorithm 1).

Step 2-5. Since the solution $\Psi^{(\text{iter})}$ is known, compute $\tilde{\sigma}_{\text{eq},m}^{(\text{iter})}$ (the equation (24)) at all discretization points.

Note that Steps 2-2 to 2-4 describe how to compute the approximate solution of the inhomogeneous boundary-value equation (15)–(16) based on the plastic strain increments obtained in the previous iteration step. The successive approximations of the plastic strain increments can be found with the approach proposed in [Mendelson 1968] in the following way.

Step 2-6. Compute a new distribution of the plastic strain increments at all discretization points. For all discretization points such that $\tilde{\sigma}_{\text{eq},m}^{(\text{iter}-1)} > 1$, apply a method presented in a block diagram (see Figure 4). This approach uses the stresses σ_{XX} , σ_{YY} , σ_{XY} obtained with the solution $\Psi^{(\text{iter})}$ together with the equivalent plastic strain increment $\Delta\tilde{\varepsilon}_{\text{eq}}^{p(\text{iter}-1)}$ (the equation (25)) and the corresponding equivalent stress $\tilde{\sigma}_{\text{eq}}^{(\text{iter}-1)}$ determined from the stress-strain curve (see Figure 5) to find a new distribution $\Delta\varepsilon_{XX}^{p(\text{iter})}$, $\Delta\varepsilon_{YY}^{p(\text{iter})}$, $\Delta\varepsilon_{XY}^{p(\text{iter})}$ of the plastic strain increments with the Prandtl–Reuss relations (23).

For the remaining discretization points, take $\Delta\varepsilon_{XX}^{p(\text{iter})} = \Delta\varepsilon_{YY}^{p(\text{iter})} = \Delta\varepsilon_{XY}^{p(\text{iter})} = 0$.

Step 2-7. Take two successive distributions of the plastic strain increments to compute the maximum distance d between two approximate solutions and the root mean square error $\delta^{(\text{iter})}$ of the boundary conditions fulfillment at Nt test points located on the boundary at each iteration step, i.e.,

$$d = \max\{d_{XX}, d_{YY}, d_{XY}\}, \quad \delta^{(\text{iter})} = \sqrt{\sum_{i=1}^{Nt} [\sigma_b(X_i, Y_i) - \sigma_a^{(\text{iter})}(X_i, Y_i)]^2 / Nt}, \quad (36)$$

where

$$d_{ij} = \sqrt{\sum_{k=1}^{Ni} [\Delta\varepsilon_{ij}^{p(\text{iter})}(X_k, Y_k) - \Delta\varepsilon_{ij}^{p(\text{iter}-1)}(X_k, Y_k)]^2 / Ni}. \quad (37)$$

σ_b denotes an exact value of the stress at a given test point on the boundary and σ_a represents the approximate value of the stress computed with the method proposed. Choose a tolerance value TOL. If $d \leq \text{TOL}$ and the root mean square error $\delta^{(\text{iter})}$ provides a sufficient accuracy of the result, then stop the internal iteration process and go further to Step 1-3. Else, take $\text{iter} = \text{iter} + 1$ and go back to Step 2-2.

Note that if the distance d is increasing for successive iterations, then the iteration process is not convergent and it is stopped. Similarly as in the case when the maximum number of iterations is exceeded before the accuracy is achieved.

Step 1-3. Take $m = m + 1$, go back to Step 1-2 and continue the main iteration process.

Finite difference approximation of partial derivatives. We can approximate values of all partial derivatives of the plastic strain increments that are needed in (19) for the function $\Delta\tilde{g}(X, Y)$ with the finite difference formulas (see, e.g., [Anderson et al. 1984; Orkisz 1998; Li and Wang 2003]). Then, values of the partial derivatives of the accumulated plastic strains that are required in (18) for the function $\tilde{g}(X, Y)$ can be easily obtained. The simplest method assumes the differentiation of the equations (20) and then the computation of the sums of the appropriate partial derivatives of the plastic strain increments. Note that values of the partial derivatives present in (19) are computed for the plastic strain increments corresponding to the interpolation points but for the appropriate finite difference equations we take the plastic strain increments that correspond to the discretization points. Such an approach increases an accuracy of the finite difference approximation. That is why, throughout the Algorithm 2, we compute values of the plastic strain increments at all discretization points.

The discretization points used in finite difference formulas are presented in Figures 3 and 6. We denote by O a given interpolation point. Furthermore, A_1, A_2, A_3 and B_1, B_2, B_3 represent the neighboring discretization points lying on the same line as the point O along the x -axis. Similarly, C_1, C_2, C_3 and D_1, D_2, D_3 are the neighboring discretization points lying along the y -axis. We can also distinguish another set of uniformly distributed discretization points E, F, G, H (see Figure 6, left). The distance between two points along the x -axis is equal to h and the distance between two points along the y -axis is represented by k . Subsequently, we refer to these distances as mesh increments.

Let P stands for any interpolation or discretization point considered. Subsequently, we denote by u_P a value of the appropriate increment of plastic strains $\Delta\varepsilon_{XX}^P$, $\Delta\varepsilon_{YY}^P$ or $\Delta\varepsilon_{XY}^P$ at the point P , respectively. For the great majority of the interpolation points, values of the appropriate partial derivatives can be approximated with the central finite difference formulas (see also Figure 6, left) given as

$$\frac{\partial^2 u_O}{\partial x^2} \approx \frac{u_{B1} - 2u_O + u_{A1}}{h^2}, \quad \frac{\partial^2 u_O}{\partial y^2} \approx \frac{u_{D1} - 2u_O + u_{C1}}{k^2}, \quad \frac{\partial^2 u_O}{\partial x \partial y} \approx \frac{u_E - u_F - u_G + u_H}{4hk}. \quad (38)$$

Nevertheless, since the plate is of irregular domain, then for some selected interpolation points located near the boundary, we have to use special formulas for the finite difference approximation. These formulas take into account different mesh increments. Such a general case is presented in Figure 6, right. As we can see, for given values of h and k , the distances between some neighboring points along the x and y axes can be smaller. In general, they can be determined by the coefficients (positive and less or equal to 1) denoted and defined as $\alpha_1 = |A_1 O|/h$, $\beta_1 = |B_1 O|/h$, $\gamma_1 = |C_1 O|/k$ and $\eta_1 = |D_1 O|/k$ (see Figure 6, right), respectively.

A choice of the appropriate finite difference formula depends on a position of the interpolation point with respect to the boundary. In most cases, each interpolation point has all their neighboring discretization points, i.e., $A_1, B_1, C_1, D_1, E, F, G, H$, even if some mesh increments are smaller than h and k . Then, we can use the following central finite difference formulas:

$$\frac{\partial^2 u_O}{\partial x^2} \approx \frac{2(\alpha_1 u_{B1} - (\alpha_1 + \beta_1)u_O + \beta_1 u_{A1})}{\alpha_1 \beta_1 (\alpha_1 + \beta_1) h^2}, \quad \frac{\partial^2 u_O}{\partial y^2} \approx \frac{2(\gamma_1 u_{D1} - (\gamma_1 + \eta_1)u_O + \eta_1 u_{C1})}{\gamma_1 \eta_1 (\gamma_1 + \eta_1) k^2}, \quad (39)$$

$$\frac{\partial^2 u_O}{\partial x \partial y} \approx \frac{1}{2h} \left(\frac{\partial u_{B1}}{\partial y} - \frac{\partial u_{A1}}{\partial y} \right). \quad (40)$$

Note that values of the partial derivatives of the first order present in (40) can be approximated with the central finite difference formula (41)₁, where P denotes a given discretization point (e.g., A_1, B_1 in (40)) and the notation $|_P$ indicates that the appropriate value is chosen with respect to the point P . We have

$$\frac{\partial u_P}{\partial y} \approx \frac{u_{D1}|_P - u_{C1}|_P}{(\gamma_1|_P + \eta_1|_P)k}, \quad \frac{\partial u_P}{\partial y} \approx \frac{3u_P - 4u_{C1}|_P + u_{C2}|_P}{2k}, \quad \frac{\partial u_P}{\partial y} \approx \frac{-3u_P + 4u_{D1}|_P - u_{D2}|_P}{2k}. \quad (41)$$

Finally, we consider the case when a given interpolation point (located very close to the boundary of the narrowed region) does not have some of its neighboring discretization points. We deal with such a situation rarely. If a number of uniformly distributed interpolation points is large, then a distance between a given interpolation point and some corresponding (located on the boundary) discretization point that should be also considered is equal or close to zero (see Section 3 and Figure 3). In such a case we do not include this point in the set of all discretization points used for further computations. Hence, for the

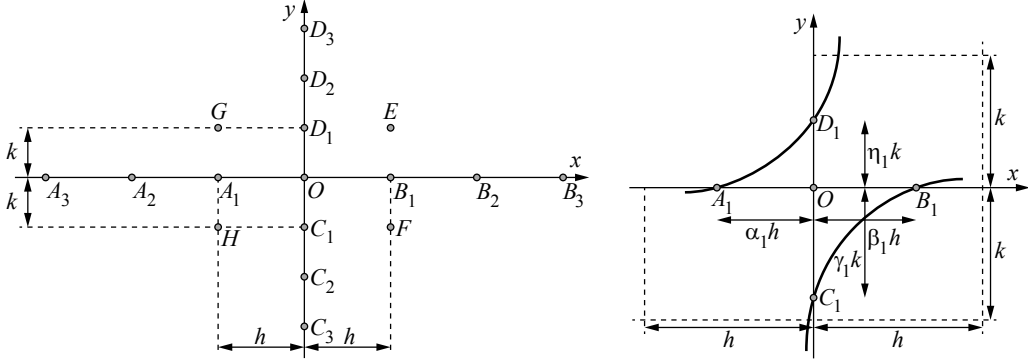


Figure 6. The distribution of the discretization points used in the finite difference formulas.

approximation of the second order derivatives with respect to x and y , we can use the backward (42)₁, (43)₁ or forward (42)₂, (43)₂ finite difference formulas given as follows:

$$\frac{\partial^2 u_O}{\partial x^2} \approx \frac{2u_O - 5u_{A_1} + 4u_{A_2} - u_{A_3}}{h^2}, \quad \frac{\partial^2 u_O}{\partial x^2} \approx \frac{2u_O - 5u_{B_1} + 4u_{B_2} - u_{B_3}}{h^2}, \quad (42)$$

$$\frac{\partial^2 u_O}{\partial y^2} \approx \frac{2u_O - 5u_{C_1} + 4u_{C_2} - u_{C_3}}{k^2}, \quad \frac{\partial^2 u_O}{\partial y^2} \approx \frac{2u_O - 5u_{D_1} + 4u_{D_2} - u_{D_3}}{k^2}. \quad (43)$$

Similarly, in the case of the mixed second order partial derivative, we can apply the following backward (44)₁ or forward (44)₂ finite differences:

$$\frac{\partial^2 u_O}{\partial x \partial y} \approx \frac{1}{2h} \left(3 \frac{\partial u_O}{\partial y} - 4 \frac{\partial u_{A_1}}{\partial y} + \frac{\partial u_{A_2}}{\partial y} \right), \quad \frac{\partial^2 u_O}{\partial x \partial y} \approx \frac{1}{2h} \left(-3 \frac{\partial u_O}{\partial y} + 4 \frac{\partial u_{B_1}}{\partial y} - \frac{\partial u_{B_2}}{\partial y} \right). \quad (44)$$

Depending on the existence and the location of the neighboring discretization points, for the approximation of the first order partial derivatives present in (44) we can choose the appropriate formula from (41).

Note that for the approximation of the partial derivatives proposed above, we take the finite difference formulas of the second order. The only exception are the finite differences (39) and (41)₁. They are of the first order accuracy due to the mesh increments that are smaller than h and k . However, for $\alpha_1 = \beta_1 = 1$ in (39)₁ and $\gamma_1 = \eta_1 = 1$ in (39)₂, the appropriate finite difference formulas reduce to the forms (38)₁ and (38)₂ of the second order accuracy, respectively. Similarly, the equation (41)₁ becomes for $\gamma_1 = \eta_1 = 1$ the central finite difference of the second order.

4. Numerical experiments

For the problem considered we choose the plate with two different depths of the narrowing. We refer to them as: 1-A (if $a = 1$, $b = 0.5$) and 1-B (if $a = 1$, $b = 0.25$), respectively. We choose $n = 0.5$ for the parameter of the elastic-plastic model (1) and we take the following material parameters: $E = 2 \times 10^{11}$ [Pa], $\nu = 0.3$, $\sigma_0 = 2 \times 10^8$ [Pa], $\varepsilon_0 = 1 \times 10^{-3}$. Further, for these two boundary-value problems we choose the loading paths to the state of stress $\tilde{\sigma}_B$. The algorithm proposed in Section 3 produces a sequence of results for each successive value of $\tilde{\sigma}_{B_m}$, if the appropriate step size is chosen as $h_{\tilde{\sigma}_B} = \tilde{\sigma}_{B_m} - \tilde{\sigma}_{B_{m-1}} = 0.0125$. The first interpolation points such that the plastic deformation occurs can be detected for $\tilde{\sigma}_B = 0.6375$ in the case of the geometry 1-A and $\tilde{\sigma}_B = 0.475$ in the case of the geometry 1-B.

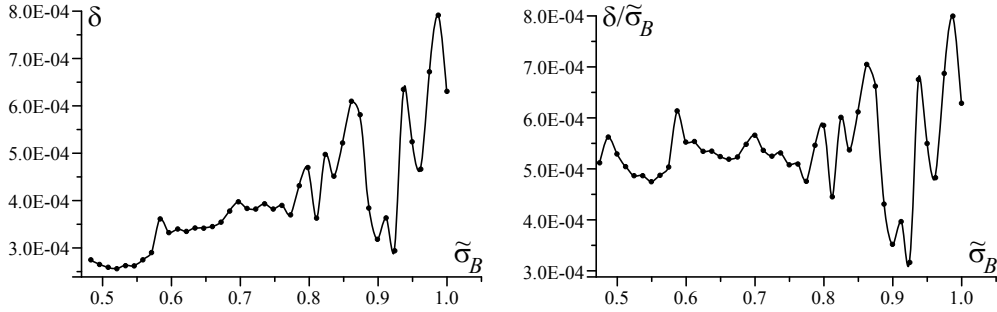


Figure 7. The root mean square error (left) and the root mean square error normalized with $\tilde{\sigma}_B$ (right) of the boundary conditions fulfillment obtained for the plate of the geometry 1-B after a constant number of eight iteration steps.

The parameters of the meshless methods were chosen so that the acceptable and small root mean square error of the solution could be achieved. Subsequently, we denote by Mc , Ms and Mi the number of collocation, source and interpolation points located on the shorter side of the plate (e.g., AB or CD). Furthermore, iMd is the number of additional intermediate discretization points placed between each two interpolation points (see Figure 3). We have $Mi = 11$, $iMd = 4$, $s = 0.2$ and $c = 0.1$. We also take $Mc = 80$, $Ms = 80$ for the geometry 1-A and $Mc = 60$, $Ms = 60$ for the geometry 1-B, respectively. For these values of parameters the distance between two neighboring interpolation points along the x and y axes is equal to 4.1667×10^{-2} and the mesh increments for the finite difference approximation are given by $h = k = 8.3333 \times 10^{-3}$.

The optimal computational procedure preferred by the authors assumes that the number of iteration steps required to obtain the solution related to succeeding stresses $\tilde{\sigma}_{Bk}$ is chosen so that the root mean

Geometry	1-A	1-B
Side of plate / Boundary condition	δ	δ
$(\Gamma_{AB}, \Gamma_{DC}) \Psi_{YY} = \tilde{\sigma}_B$	6.220×10^{-4}	3.601×10^{-4}
$(\Gamma_{E_1B}, \Gamma_{E_2C}, \Gamma_{F_1A}, \Gamma_{F_2D}) \Psi_{XX} = 0$	2.777×10^{-3}	7.253×10^{-4}
$(\Gamma_{AB}, \Gamma_{DC}, \Gamma_{E_1B}, \Gamma_{E_2C}, \Gamma_{F_1A}, \Gamma_{F_2D}) \Psi_{XY} = 0$	2.287×10^{-3}	2.174×10^{-4}
$(\Gamma_{E_1E_2}) \Psi_{YY}n_x - \Psi_{XY}n_y = 0$	4.020×10^{-3}	2.880×10^{-4}
$(\Gamma_{E_1E_2}) \Psi_{XX}n_y - \Psi_{XY}n_x = 0$	1.637×10^{-3}	6.977×10^{-4}
$(\Gamma_{F_1F_2}) \Psi_{YY}n_x - \Psi_{XY}n_y = 0$	4.019×10^{-3}	2.880×10^{-4}
$(\Gamma_{F_1F_2}) \Psi_{XX}n_y - \Psi_{XY}n_x = 0$	1.636×10^{-3}	6.977×10^{-4}
(Γ) Total	2.496×10^{-3}	4.691×10^{-4}
Final distance d	4.825×10^{-4}	4.018×10^{-3}

Table 1. Values of the root mean square error δ of the boundary conditions fulfillment for the different boundary conditions corresponding to the appropriate sides of the plate, the final distance d between to two last successive distributions of the plastic strain increments obtained with the algorithm proposed for $\tilde{\sigma}_B = 0.8$ and the geometries 1-A and 1-B. Eight iterations in total were used in each case.

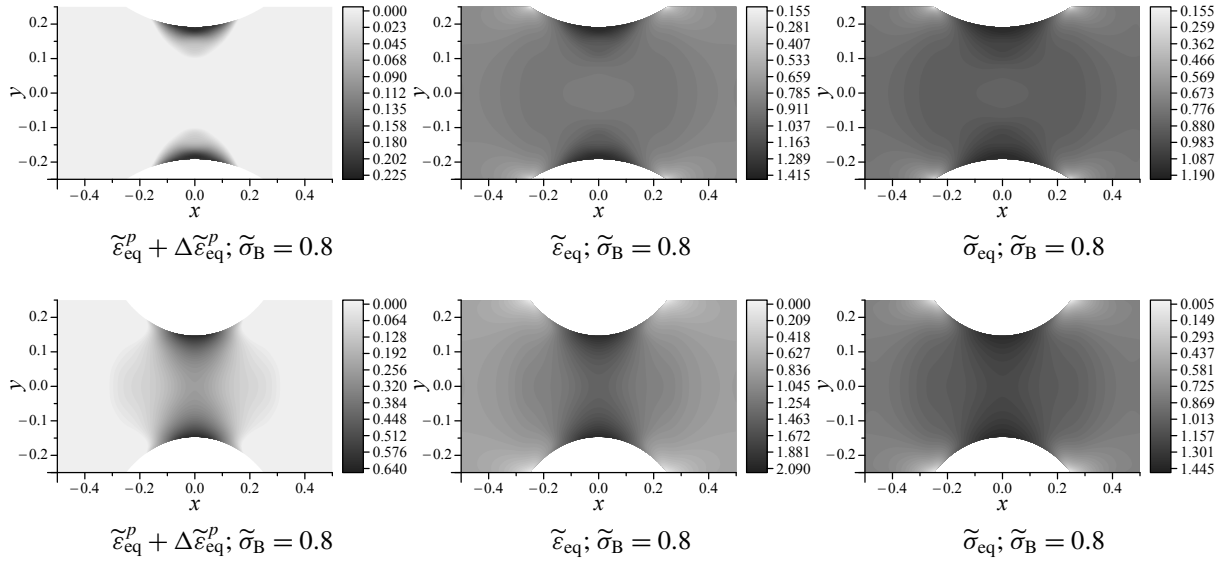


Figure 8. The comparison of the equivalent plastic strains $\tilde{\varepsilon}_{\text{eq}}^p + \Delta\tilde{\varepsilon}_{\text{eq}}^p$ (left), the equivalent total strains $\tilde{\varepsilon}_{\text{eq}}$ (middle) and the equivalent stress $\tilde{\sigma}_{\text{eq}}$ (right) in the plate of the geometry 1-A (top) and 1-B (bottom), respectively.

square error and a given tolerance imposed on the iteration process are sufficiently small. Nevertheless, since the accuracy of the solution is acceptable also for the constant number of iterations, we always perform eight iteration steps. Note that all computations were performed with the C++ libraries for the floating-point conversions in the double extended precision format (dedicated for the Intel C++ compiler) as proposed in [Jankowska 2010].

First, we present the accuracy of the approximate solution obtained for different conditions of loading for the plate of the geometry 1-B. As we can see in Figure 7, the root mean square error and the normalized root mean square error of the boundary conditions fulfillment obtained after a constant number of 8 iteration steps remain of the same order. The curve profiles indicate however that for larger values of the stress $\tilde{\sigma}_B$ more iteration steps (or just their different numbers) are required to retain the assumed accuracy.

In Table 1 we can see a comparison of values of the root mean square error of the boundary conditions fulfillment for the different boundary conditions corresponding to the appropriate sides of the plate and the final distance between two last successive distributions of the plastic strain increments. Such results are provided for the loading state related to $\tilde{\sigma}_B = 0.8$ and both geometries 1-A and 1-B. Then, the appropriate distributions of the equivalent plastic strains, the equivalent total strains and the equivalent stress in the plate obtained for the same value of $\tilde{\sigma}_B = 0.8$ and both geometries are presented in Figure 8. The regions of elastic and plastic deformation can be observed there.

5. Conclusions

A method for solving some plane elastoplastic boundary-value problem describing the stress state in the plate subjected to uniaxial extension is proposed. It is based on the successive-approximation iteration

process that is further combined with the meshless methods (the method of fundamental solutions and the method of particular solutions). Due to the special form of the right-hand side function of the governing equation the approximation of some partial derivatives with finite difference formulas is also applied. The authors introduce a new set of auxiliary discretization points that is utilized to control the finite difference approximation accuracy. Such points are not directly used for solving a sequence of nonhomogeneous boundary-value problems involved. Hence, the dimensions of some linear systems of equations that appear in each iteration step due to the meshless methods applied, are as always limited to the number of collocation and interpolations points. Note that the discretization points are uniformly located in the domain (except for the ones that are placed in the neighborhood of the narrowing). However, there is an increasing number of papers that propose an application of irregular grid (cloud) of points for the finite difference approximation (see the generalized finite difference (GFD) methods proposed, e.g., in [Orkisz 1998; Benito et al. 2007]). On the other hand, an application of the meshless methods for the problem considered is easy even in the case of complicated geometries. Furthermore, since the solution, i.e., the stress function, is approximated by linear combinations of fundamental solutions and particular solutions, we can compute values of stresses and strains not only in the interpolation or discretization points but at any point in the domain.

In the opinion of the authors the meshless methods are good alternative to the mesh methods in the case of many scientific problems. So far they were mainly used for solving some linear initial-boundary value problems with the Picard iteration process or the Newton–Raphson method as possible algorithms for nonlinear problems. Recently, several efficient algorithms that can be used together with the meshless methods for solving the nonlinear problems, appeared in the literature. Some of them are based on perturbation techniques that transform a nonlinear problem into a sequence of linear problems (see, e.g., the homotopy analysis method (HAM) described in [Liao 2004; Tsai 2012] and the asymptotic numerical method (ANM) proposed in [Tri et al. 2012]). Furthermore, we can use the Kansa method [1990] by an approximation of a solution with a linear combination of radial basis functions. Such an approach results in a nonlinear system of equations to be solved.

References

- [Al-Gahtani 2012] H. J. Al-Gahtani, “DRM-MFS for two-dimensional finite elasticity”, *Eng. Anal. Bound. Elem.* **36**:10 (2012), 1473–1477.
- [Anderson et al. 1984] D. A. Anderson, J. C. Tannehill, and R. H. Pletcher, *Computational fluid mechanics and heat transfer*, Hemisphere Publishing, Washington, DC, 1984.
- [Balakrishnan and Ramachandran 1999] K. Balakrishnan and P. A. Ramachandran, “A particular solution Trefftz method for non-linear Poisson problems in heat and mass transfer”, *J. Comput. Phys.* **150**:1 (1999), 239–267.
- [Balakrishnan and Ramachandran 2001] K. Balakrishnan and P. A. Ramachandran, “Osculatory interpolation in the method of fundamental solution for nonlinear Poisson problems”, *J. Comput. Phys.* **172**:1 (2001), 1–18.
- [Balakrishnan et al. 2002] K. Balakrishnan, R. Sureshkumar, and P. A. Ramachandran, “An operator splitting-radial basis function method for the solution of transient nonlinear Poisson problems”, *Comput. Math. Appl.* **43**:3-5 (2002), 289–304.
- [Belytschko et al. 2000] T. Belytschko, W. K. Liu, and B. Moran, *Nonlinear finite elements for continua and structures*, Wiley, Chichester, 2000.
- [Benito et al. 2007] J. J. Benito, F. Ureña, and L. Gavete, “Solving parabolic and hyperbolic equations by the generalized finite difference method”, *J. Comput. Appl. Math.* **209**:2 (2007), 208–233.

- [Berezhnoĭ and Paĭmushin 2011] D. V. Berezhnoĭ and V. N. Paĭmushin, “Two formulations of elastoplastic problems and the theoretical determination of the location of neck formation in samples under tension”, *J. Appl. Math. Mech.* **75**:4 (2011), 447–462.
- [Bilotta and Casciaro 2007] A. Bilotta and R. Casciaro, “A high-performance element for the analysis of 2D elastoplastic continua”, *Comput. Methods Appl. Mech. Eng.* **196**:4-6 (2007), 818–828.
- [Boudaia et al. 2009] E. Boudaia, L. Bousshine, H. F. Fihri, and G. D. Saxce, “Modelling of orthogonal cutting by incremental elastoplastic analysis and meshless method”, *C. R. Méc.* **337**:11-12 (2009), 761–767.
- [Boumaiza and Aour 2014] D. Boumaiza and B. Aour, “On the efficiency of the iterative coupling FEM-BEM for solving the elasto-plastic problems”, *Eng. Struct.* **72**:1 (2014), 12–25.
- [Burgess and Mahajerin 1987] G. Burgess and E. Mahajerin, “The fundamental collocation method applied to the nonlinear Poisson equation in two dimensions”, *Comput. Struct.* **27**:6 (1987), 763–767.
- [Chakrabarty 1987] J. Chakrabarty, *Theory of plasticity*, McGraw-Hill, New York, 1987.
- [Chen 1995] C. S. Chen, “The method of fundamental solutions for non-linear thermal explosions”, *Commun. Numer. Methods Eng.* **11**:8 (1995), 675–681.
- [Chen et al. 2014] W. Chen, Z.-J. Fu, and C. S. Chen, *Recent advances in radial basis function collocation methods*, Springer, Heidelberg, 2014.
- [Crisfield 1997] M. A. Crisfield, *Non-linear finite element analysis of solids and structures*, Wiley, Chichester, 1997.
- [Cui et al. 2009] X. Y. Cui, G. R. Liu, G. Y. Li, G. Y. Zhang, and G. Y. Sun, “Analysis of elastic-plastic problems using edge-based smoothed finite element method”, *Int. J. Press. Vessels Pip.* **86**:10 (2009), 711–718.
- [Dai et al. 2006] K. Y. Dai, G. R. Liu, X. Han, and Y. Li, “Inelastic analysis of 2D solids using a weak-form RPIM based on deformation theory”, *Comput. Methods Appl. Mech. Eng.* **195**:33-36 (2006), 4179–4193.
- [Deng et al. 2011] Q. Deng, C. Li, S. Wang, H. Zheng, and X. Ge, “A nonlinear complementarity approach for elastoplastic problems by BEM without internal cells”, *Eng. Anal. Bound. Elem.* **35**:3 (2011), 313–318.
- [Dong and Bonnet 1998] C. Y. Dong and M. Bonnet, “Symmetric-iterative solution of coupled BE and FE discretizations for elastoplastics”, *Comput. Methods Appl. Mech. Eng.* **178**:1-2 (1998), 171–182.
- [Fairweather and Karageorghis 1998] G. Fairweather and A. Karageorghis, “The method of fundamental solutions for elliptic boundary value problems”, *Adv. Comput. Math.* **9**:1-2 (1998), 69–95.
- [Fairweather et al. 2003] G. Fairweather, A. Karageorghis, and P. A. Martin, “The method of fundamental solutions for scattering and radiation problems”, *Eng. Anal. Bound. Elem.* **27**:7 (2003), 759–769.
- [Fallahi and Hosami 2011] M. Fallahi and M. Hosami, “The quasi-linear method of fundamental solution applied to transient non-linear Poisson problems”, *Eng. Anal. Bound. Elem.* **35**:3 (2011), 550–554.
- [Feng et al. 2013] P. Y. Feng, N. Ma, and X. C. Gu, “Application of method of fundamental solutions in solving potential flow problems for ship motion prediction”, *J. Shanghai Jiaotong Univ. Sci.* **18**:2 (2013), 153–158.
- [Gao and Davies 2000] X. W. Gao and T. G. Davies, “An effective boundary element algorithm for 2D and 3D elastoplastic problems”, *Int. J. Solids Struct.* **37**:36 (2000), 4987–5008.
- [Jankowska 2010] M. A. Jankowska, “Remarks on algorithms implemented in some C++ libraries for floating-point conversions and interval arithmetic”, pp. 436–445 in *Parallel processing and applied mathematics*, edited by R. Wyrzykowski et al., Lecture Notes in Computer Science **6068**, Springer, Berlin, 2010.
- [Jankowska and Kołodziej 2013] M. A. Jankowska and J. A. Kołodziej, “The method of fundamental solutions together with the successive-approximation method as an alternative approach to solving some plane elastoplastic problem”, pp. 1 in *COMPLAS 2013 - XII International Conference on Computational Plasticity* (Barcelona, Spain, 2013), edited by E. Onate et al., International Center for Numerical Methods in Engineering (CIMNE), Barcelona, Spain, 2013.
- [Jankowska and Kołodziej 2014] M. A. Jankowska and J. A. Kołodziej, “Application of the method of fundamental solutions for the study of the stress state of the plate subjected to uniaxial tension”, pp. 20–22 in *TRECOP 2014 - International Symposium on Trends in Continuum Physics* (Bedlewo, 2014), edited by B. T. Maruszewski et al., Agencja Reklamowa COMPRINT, Poznan, Poland, 2014.

- [Jankowska and Kołodziej 2015] M. A. Jankowska and J. A. Kołodziej, “On the application of the method of fundamental solutions for the study of the stress state of a plate subjected to elastic–plastic deformation”, *Int. J. Solids Struct.* **67-68** (2015), 139–150.
- [Kansa 1990] E. J. Kansa, “Multiquadrics—a scattered data approximation scheme with applications to computational fluid-dynamics, I: Surface approximations and partial derivative estimates”, *Comput. Math. Appl.* **19**:8-9 (1990), 127–145.
- [Karageorghis and Fairweather 1989] A. Karageorghis and G. Fairweather, “The method of fundamental solutions for the solution of nonlinear plane potential problems”, *IMA J. Numer. Anal.* **9**:2 (1989), 231–242.
- [Karageorghis and Lesnic 2008] A. Karageorghis and D. Lesnic, “Steady-state nonlinear heat conduction in composite materials using the method of fundamental solutions”, *Comput. Methods Appl. Mech. Eng.* **197**:33-40 (2008), 3122–3137.
- [Karageorghis et al. 2011] A. Karageorghis, D. Lesnic, and L. Marin, “A survey of applications of the MFS to inverse problems”, *Inverse Probl. Sci. Eng.* **19**:3 (2011), 309–336.
- [Kojić and Bathe 2005] M. Kojić and K.-J. Bathe, *Inelastic analysis of solids and structures*, Springer, Berlin, 2005.
- [Kołodziej et al. 2013] J. A. Kołodziej, M. A. Jankowska, and M. Mierzwiczak, “Meshless methods for the inverse problem related to the determination of elastoplastic properties from the torsional experiment”, *Int. J. Solids Struct.* **50**:25-26 (2013), 4217–4225.
- [Li and Wang 2003] Z. Li and C. Wang, “A fast finite difference method for solving Navier–Stokes equations on irregular domains”, *Commun. Math. Sci.* **1**:1 (2003), 180–196.
- [Li and Zhu 2009] X. Li and J. Zhu, “The method of fundamental solutions for nonlinear elliptic problems”, *Eng. Anal. Bound. Elem.* **33**:3 (2009), 322–329.
- [Li et al. 2014] M. Li, C. S. Chen, C. C. Chu, and D. L. Young, “Transient 3D heat conduction in functionally graded materials by the method of fundamental solutions”, *Eng. Anal. Bound. Elem.* **45** (2014), 62–67.
- [Liao 2004] S. Liao, *Beyond perturbation: Introduction to the homotopy analysis method*, CRC Series: Modern Mechanics and Mathematics **2**, Chapman & Hall/CRC, Boca Raton, FL, 2004.
- [Liu 2003] G. R. Liu, *Mesh free methods: Moving beyond the finite element method*, CRC Press, Boca Raton, FL, 2003.
- [Liu et al. 2011] H. Liu, Z. Xing, Z. Sun, and J. Bao, “Adaptive multiple scale meshless simulation on springback analysis in sheet metal forming”, *Eng. Anal. Bound. Elem.* **35**:3 (2011), 436–451.
- [Liu et al. 2012] Y. Liu, C. Wang, and Q. Yang, “Stability analysis of soil slope based on deformation reinforcement theory”, *Finite Elem. Anal. Des.* **58** (2012), 10–19.
- [Liu et al. 2013] X. Liu, M. A. Bradford, and R. E. Erkmen, “Non-linear inelastic analysis of steel–concrete composite beams curved in-plan”, *Eng. Struct.* **57** (2013), 484–492.
- [Marin and Lesnic 2007] L. Marin and D. Lesnic, “The method of fundamental solutions for nonlinear functionally graded materials”, *Int. J. Solids Struct.* **44**:21 (2007), 6878–6890.
- [Mendelson 1968] A. Mendelson, *Plasticity: Theory and application*, McMillan, New York, 1968.
- [Mollazadeh et al. 2011] M. Mollazadeh, M. J. Khanjani, and A. Tavakoli, “Applicability of the method of fundamental solutions to interaction of fully nonlinear water waves with a semi-infinite floating ice plate”, *Cold Regions Sci. Technol.* **69**:1 (2011), 52–58.
- [Ochiai 2011] Y. Ochiai, “Three-dimensional thermo-elastoplastic analysis by triple-reciprocity boundary element method”, *Eng. Anal. Bound. Elem.* **35**:3 (2011), 478–488.
- [Orkisz 1998] J. Orkisz, “Finite difference method, III”, pp. 336–432 in *Handbook of computational solid mechanics*, edited by M. Kleiber, Springer, Berlin, 1998.
- [Owen and Hinton 1980] D. R. J. Owen and E. Hinton, *Finite elements in plasticity: Theory and practice*, Pineridge Press, Swansea, 1980.
- [Oysu and Fenner 2006] C. Oysu and R. T. Fenner, “Coupled FEM-BEM for elastoplastic contact problems using lagrange multipliers”, *Appl. Math. Model.* **30**:3 (2006), 231–247.
- [Pozo et al. 2009] L. P. Pozo, F. Perazzo, and A. Angulo, “A meshless FPM model for solving nonlinear material problems with proportional loading based on deformation theory”, *Adv. Eng. Softw.* **40**:11 (2009), 1148–1154.

- [Shanazari and Fallahi 2010] K. Shanazari and M. Fallahi, “A quasi-linear technique applied to the method of fundamental solution”, *Eng. Anal. Bound. Elem.* **34**:4 (2010), 388–392.
- [Timoshenko and Goodier 1951] S. Timoshenko and J. N. Goodier, *Theory of elasticity*, 2nd ed., McGraw-Hill, New York, 1951.
- [Tri et al. 2011] A. Tri, H. Zahrouni, and M. Potier-Ferry, “Perturbation technique and method of fundamental solution to solve nonlinear Poisson problems”, *Eng. Anal. Bound. Elem.* **35**:3 (2011), 273–278.
- [Tri et al. 2012] A. Tri, H. Zahrouni, and M. Potier-Ferry, “High order continuation algorithm and meshless procedures to solve nonlinear Poisson problems”, *Eng. Anal. Bound. Elem.* **36**:11 (2012), 1705–1714.
- [Tsai 2012] C.-C. Tsai, “Homotopy method of fundamental solutions for solving certain nonlinear partial differential equations”, *Eng. Anal. Bound. Elem.* **36**:8 (2012), 1226–1234.
- [Uscilowska and Berendt 2013] A. Uscilowska and D. Berendt, “An implementation of the method of fundamental solutions for the dynamic response of von Karman nonlinear plate model”, *Int. J. Comput. Methods* **10**:2 (2013), 1341005.
- [Wang and Qin. 2006] H. Wang and Q. H. Qin., “A meshless method for generalized linear or nonlinear Poisson-type problems”, *Eng. Anal. Bound. Elem.* **30**:6 (2006), 515–521.
- [Wang and Qin. 2008] H. Wang and Q. H. Qin., “Meshless approach for thermo-mechanical analysis of functionally graded materials”, *Eng. Anal. Bound. Elem.* **32**:9 (2008), 704–712.
- [Wang et al. 2005] H. Wang, Q.-H. Qin., and Y. L. Kang, “A new meshless method for steady-state heat conduction problems in anisotropic and inhomogeneous media”, *Arch. Appl. Mech.* **74**:8 (2005), 563–579.
- [Wang et al. 2012] H. Wang, Q.-H. Qin, and X.-P. Liang, “Solving the nonlinear Poisson-type problems with F-Trefftz hybrid finite element model”, *Eng. Anal. Bound. Elem.* **36**:1 (2012), 39–46.
- [Yeon and Youn 2005] J.-H. Yeon and S. K. Youn, “Meshfree analysis of softening elastoplastic solids using variational multi-scale method”, *Int. J. Solids Struct.* **42**:14 (2005), 4030–4057.
- [Young et al. 2008] D. L. Young, C. M. Fan, S. P. Hu, and S. N. Atluri, “The Eulerian–Lagrangian method of fundamental solutions for two-dimensional unsteady Burgers’ equations”, *Eng. Anal. Bound. Elem.* **32**:5 (2008), 395–412.
- [Young et al. 2009] D. L. Young, Y. C. Lin, C. M. Fan, and C. L. Chiu, “The method of fundamental solutions for solving incompressible Navier–Stokes problems”, *Eng. Anal. Bound. Elem.* **33**:8-9 (2009), 1031–1044.

Received 2 Jan 2015. Revised 29 Jul 2015. Accepted 17 Aug 2015.

MALGORZATA A. JANKOWSKA: malgorzata.jankowska@put.poznan.pl
Institute of Applied Mechanics, Poznan University of Technology, Jana Pawła II 24, 60-965 Poznan, Poland

JAN ADAM KOŁODZIEJ: jan.kolodziej@put.poznan.pl
Institute of Applied Mechanics, Poznan University of Technology, Jana Pawła II 24, 60-965 Poznan, Poland

IMPLEMENTATION OF HAM AND MESHLESS METHOD FOR TORSION OF FUNCTIONALLY GRADED ORTHOTROPIC BARS

ANITA UŚCIŁOWSKA AND AGNIESZKA FRASKA

The aim of this study is implementation of the Homotopy Analysis Method (HAM) and the Method of Fundamental Solution (MFS) for solving a torsion problem of functionally graded orthotropic bars. The boundary value problem is formulated for the Prandtl's stress function, described by partial differential equation of second order with variable coefficients and appropriate boundary conditions. In the solving process the HAM is used to convert nonlinear equation into a linear one with known fundamental solutions. The Method of Fundamental Solutions supported by Radial Basis Functions and Monomials is suggested for calculate this linear boundary value problem. The numerical experiment has been performed to check the accuracy and the convergence of the presented method.

1. Introduction

The torsion problem of bars is an important issue in engineering science. And it is not a new question. Especially twisting of prismatic bars made with homogeneous and isotropic materials have been undertaken by many authors [Kołodziej and Fraska 2005; Nowacki 1970; Naghdi 1994; Timoshenko and Goodier 1970]. In the last time, the case of inhomogeneous and/or anisotropic material is more often discussed in literature [Chen 2011; Horgan and Chan 1998/99; Xu et al. 2010]. It is related to the research on functionally graded materials (FGMs), designed for special engineering applications including aircraft, aerospace, automobile industry and medicine. Functionally graded materials are characterized by the continuous changes of their properties at least in one direction and this feature distinguishes them from the conventional composite materials [Miyamoto et al. 1999]. In fact the concept of FGMs is inspired with materials occurring in nature, such as: bones, skin and bamboo [Jha et al. 2013]. These materials have functionally graded and hierarchical structure and they also have different architecture that results in orthotropic behaviour [Birman and Byrd 2007].

In this work the torsion problem of linear elastic, orthotropic, prismatic bars made with FGMs is investigated. This is a boundary value problem, described by partial differential equation of second order with variable coefficients and appropriate boundary conditions. The problem is formulated for the Prandtl's stress function. Generally, when the shear flexibility moduli are arbitrary functions of cross-sectional coordinates, the analytical solution is not available. In [Ecsedi 2013] non-homogeneous anisotropic (monoclinic) bars were considered, assuming that the shear flexibility moduli are given functions of the Prandtl's stress function of corresponding homogeneous problem. Due this formulation, the obtained analytical solution of the torsion of non-homogeneous monoclinic bar is expressed in terms of the Prandtl's stress functions of a homogeneous monoclinic bar, which has the same cross-section

Keywords: homotopy analysis method, mesh-free methods, method of fundamental solutions, functionally graded materials, orthotropic symmetry, torsion of a prismatic bar.

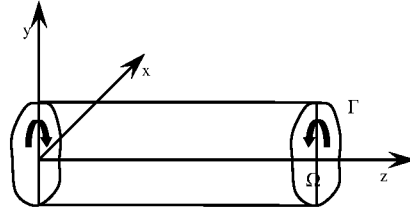


Figure 1. Torsion of prismatic bar of arbitrary cross-section Ω .

as the non-homogenous bar. But, method proposed by Ecsedi is not universal for any kind of function describing the non-homogeneity of a material. In contrast to Ecsedi's paper, the method presented by us is more general because functions describing the shear flexibility moduli are arbitrary functions of cross-sectional coordinates. We propose the Homotopy Analysis Method combined with the meshless method to solve considered problem. Used mesh-free method is the Method of Fundamental Solutions supported by Radial Basis Functions and Monomials. Uściłowska has examined application of this method in case of isotropic non-homogenous rod [Uściłowska 2010]. The MFS is highly effective method if the fundamental solution of considered equation is available. In the solving process the HAM is used to convert considered equation into a linear one with known fundamental solutions. The HAM was proposed in [Liao 1997]. It is a very useful tool for solving nonlinear problems. Moreover applying HAM with auxiliary parameter h , allows to control the convergence. Compared with other method often used to adapt MFS to nonlinear problems, based on Picard iteration, it is undoubted advantage of HAM, because in method of Picard iteration the process of iteration may be divergent [Uściłowska 2008].

2. Problem description

Consider a functionally graded, orthotropic, linearly elastic bar of an arbitrary and uniform cross-section Ω . The axis Oz is parallel to the longitudinal axis of the bar and the bar is twisted by two couples of forces acting on its ends (see Figure 1). It is assumed that there are no body forces and the bar is free from external forces on its lateral surface. There are no normal stresses on the frontal cross-sections also.

In case of orthotropic bar there are two independent material characteristics G_{13} and G_{23} in the torsion equation (see Appendix), where G_{13} is a shear modulus in direction axis x on the plane whose is normal in direction z and adequate G_{23} is a shear modulus in direction y on the plane whose is normal in direction z . We assumed that the shear flexibility moduli G_{13} and G_{23} , are the continuous and differentiable functions depending on geometrical coordinates x and y .

The problem is formulated in terms of the Prandtl's stress function u and it is described by the equation [Lekhnitskii 1977]

$$\frac{\partial}{\partial x} \left(\frac{1}{G_{23}(x, y)} \frac{\partial u}{\partial x} \right) + \frac{\partial}{\partial y} \left(\frac{1}{G_{13}(x, y)} \frac{\partial u}{\partial y} \right) = -2 \text{ for } (x, y) \in \Omega, \quad (1)$$

and the boundary condition

$$u = 0 \text{ for } (x, y) \in \Gamma. \quad (2)$$

The stresses are defined as

$$\sigma_{xz} = \theta \frac{\partial u}{\partial y}, \quad \sigma_{yz} = -\theta \frac{\partial u}{\partial x}, \quad (3)$$

where σ_{xz} and σ_{yz} are stress tensor components, and θ is the twist angle.

3. The numerical algorithm for solving the boundary value problem

The aim of this study is implementation of the Homotopy Analysis Method (HAM) and the Method of Fundamental Solution (MFS) for solving above boundary value problem. For clarity the considered boundary value problem (1)–(2) is rewritten in a general form

$$Au = f \text{ in } \Omega, \quad (4)$$

$$Bu = g \text{ on } \Gamma, \quad (5)$$

where A is the operator of the partial differential equation (PDE), B is the operator of the boundary condition, $u = u(x, y)$ is the unknown function, and f, g are the given functions on the right hand side of the equations. In considered boundary value problem (BVP)

$$A = \frac{\partial}{\partial x} \left(\frac{1}{G_{23}(x, y)} \frac{\partial}{\partial x} \right) + \frac{\partial}{\partial y} \left(\frac{1}{G_{13}(x, y)} \frac{\partial}{\partial y} \right), \quad B = 1, \quad f = -2 \text{ and } g = 0.$$

In the solution procedure the HAM is applied to convert the considered PDE into a set of linear inhomogeneous equations.

In order to apply the HAM, it is required to construct a linear problem

$$L_g u = L_g u_0 \text{ in } \Omega, \quad (6)$$

$$L_b u = L_b u_0 \text{ on } \Gamma, \quad (7)$$

where L_g, L_b — are certain linear operators, here $L_g = \nabla^2, L_b = 1, u_0 = u_0(x, y)$ is the zeroth-order solution.

The proposed homotopy deforms the linear problem (6)–(7) to problem (4)–(5):

$$(1 - \lambda)L_g(U - u_0) = h\lambda(AU - f) \text{ in } \Omega, \quad (8)$$

$$(1 - \lambda)L_b(U - u_0) = h\lambda(BU - g) \text{ on } \Gamma, \quad (9)$$

where λ is the homotopy parameter and $\lambda \in [0, 1]$. The additional parameter h allows controlling the convergence, $h < 0$. The solution of the problem is denoted by $U = U(x, y, \lambda, h)$. When $\lambda = 1$ we obtain the equations (4)–(5) and when $\lambda = 0$ the problem reduces to linear problem (6)–(7) for calculating zeroth-order solution $u_0 = U(x, y, 0, h)$.

This homotopy is assumed to be smooth function and the solution of the problem (8)–(9) can be expanded by the Taylor series

$$U(x, y, \lambda, h) = U(x, y, 0, h) + \sum_{i=1}^{\infty} \frac{\lambda^i}{i!} \frac{\partial^i U(x, y, \lambda, h)}{\partial \lambda^i} \Big|_{\lambda=0} = u_0(x, y) + \sum_{i=1}^{\infty} \frac{\lambda^i}{i!} u_0^{(i)}(x, y), \quad (10)$$

where $u_0^{(i)}(x, y) = \frac{\partial^i U(x, y, \lambda, h)}{\partial \lambda^i} \Big|_{\lambda=0}$.

Therefore, putting $\lambda = 1$, gives us the solution of equations (4)–(5)

$$u(x, y) = U(x, y, 1, h) = u_0(x, y) + \sum_{i=1}^{\infty} \frac{u_0^{(i)}(x, y)}{i!}. \quad (11)$$

Substituting (10) into (8)–(9) and collecting the coefficients of the powers of λ we obtain sequence of linear inhomogeneous PDEs

$$\begin{cases} L_g u_0^{(1)} = h(Au_0 - f) \\ L_g u_0^{(i)} = i(L_g u_0^{(i-1)} + \frac{h}{(i-1)!} \frac{\partial^{i-1}(AU)}{\partial \lambda^{i-1}}|_{\lambda=0}) \end{cases} \text{ for } i = 2, 3, 4, \dots \quad \text{in } \Omega, \quad (12)$$

$$\begin{cases} L_b u_0^{(1)} = h(Bu_0 - g) \\ L_b u_0^{(i)} = 0 \end{cases} \text{ for } i = 2, 3, 4, \dots \quad \text{on } \Gamma. \quad (13)$$

The quantity $\frac{\partial^{i-1}(AU)}{\partial \lambda^{i-1}}|_{\lambda=0}$ given in formula (12) for operator A has the following form $\frac{\partial^{i-1}(AU)}{\partial \lambda^{i-1}}|_{\lambda=0} = A \frac{\partial^{i-1}(U)}{\partial \lambda^{i-1}}|_{\lambda=0} = Au_0^{(i-1)}$.

The solutions $u_0^{(i)}(x, y)$ of BVPs (12)–(13) are the elements of the series (10) and (11).

Now each of linear problems (12)–(13) for $i = 1, 2, 3, \dots$ is solved by means of mesh-free methods that is the MFS supported by approximation by Radial Basis Functions (RBFs).

Let's rewrite the boundary value problem in a general form

$$L_g u_0^{(i)}(x, y) = f^{(i)}(x, y) \text{ in } \Omega, \quad (14)$$

$$L_b u_0^{(i)}(x, y) = g^{(i)}(x, y) \text{ on } \Gamma, \quad (15)$$

where $f^{(i)}, g^{(i)}$ are the right-hand side functions in (12) and (13), for $i = 1, 2, 3, \dots$

In the methods of fundamental solutions, the general solution of the i -th order is decomposed into two parts, a particular solution $u_p^{(i)}$ and a homogeneous solution $u_h^{(i)}$

$$u_0^{(i)} = u_p^{(i)} + u_h^{(i)}. \quad (16)$$

The particular solution fulfils (14) but not necessary the boundary condition (15). In order to obtain a particular solution of (14) the right-hand side function $f^{(i)}$ should be approximated by radial basis function and monomials in the following way:

$$f^{(i)}(x, y, u^{(i-1)}(x, y)) \cong \sum_{k=1}^{N_w} a_k^{(i)} \varphi_k(x, y) + \sum_{l=1}^{N_l} b_l^{(i)} p_l(x, y), \quad (17)$$

where $\varphi_k(x, y) = \varphi(\|(x - x_k^a, y - y_k^a)\|)$ is RBF, points $(x_k^a, y_k^a) \in \Omega \cup \Gamma$, for $k = 1, 2, \dots, N_w$ are the approximation points placed in considered domain, N_w is a number of approximation points, and $p_l(x, y)$ for $l = 1, 2, \dots, N_l$ are monomials, where N_l is a number of monomials. As regards coefficients $a_k^{(i)}$ and $b_k^{(i)}$, these are real numbers determined successively in each iteration.

The approximation formula (17) written for each approximation point in the domain, for $j = 1, \dots, N_w$, has the form

$$f^{(i)}(x_j^a, y_j^a, u^{(i-1)}(x_j^a, y_j^a)) = \sum_{k=1}^{N_w} a_k^{(i)} \varphi_k(x_j^a, y_j^a) + \sum_{l=1}^{N_l} b_l^{(i)} p_l(x_j^a, y_j^a). \quad (18)$$

Additionally, the condition (19) should be satisfied, to guarantee the limitation of the solution

$$\sum_{k=1}^{N_w} a_k^{(i)} p_l(x_k^a, y_k^a) = 0, \text{ for } l = 1, 2, \dots, N_l. \quad (19)$$

The approximate particular solution of (12) is expressed by the equation

$$u_p^{(i)}(x, y) = \sum_{k=1}^{N_w} a_k^{(i)} \phi_k(x, y) + \sum_{l=1}^{N_l} b_l^{(i)} P_l(x, y), \text{ for } (x, y) \in \Omega. \quad (20)$$

The functions $\phi_k(x, y)$ and $P_l(x, y)$ are the particular solutions of the equations

$$L\phi_k(x, y) = \varphi_k(x, y) \text{ for } (x, y) \in \Omega, \quad k = 1, 2, \dots, N_w, \quad (21)$$

$$LP_l(x, y) = p_l(x, y) \text{ for } (x, y) \in \Omega, \quad l = 1, 2, \dots, N_l. \quad (22)$$

In this way the particular solution is obtained. Next stage consists of calculating the homogenous solution on a basis of the dependence

$$u_h^{(i)}(x, y) = \sum_{n=1}^{N_s} c_n^{(i)} f s_n(x, y), \quad (23)$$

where $f s_n(x, y) = \ln \sqrt{(x - x_n^s)^2 + (y - y_n^s)^2}$ is fundamental solution of the Laplace equation, and (x_n^s, y_n^s) , for $n = 1, 2, \dots, N_s$, are the source points placed outside the region Ω , N_s is the number of the source points.

By virtue of (16) the coefficients $c_n^{(i)}$ are calculated from the modified boundary condition

$$\sum_{n=1}^{N_s} c_n^{(i)} f s_n(x_m^b, y_m^b) = -u_p^{(i)}(x_m^b, y_m^b) \text{ for } m = 1, 2, \dots, N_b. \quad (24)$$

The points $(x_m^b, y_m^b) \in \Gamma$ are the boundary points placed on the contour of the region Ω , and N_b is the number of boundary points.

Finally the general solution of the considered problem is calculated from (11).

The procedure is finished if the parameter defined by formula (25) is a small number, of order 10^{-5}

$$d = \|u_0^{(i)}(x, y) - u_0^{(i-1)}(x, y)\| \text{ for } i = 1, 2, \dots \quad (25)$$

At the moment the numerical algorithm for solving the boundary-value problem (12)–(13) is completed.

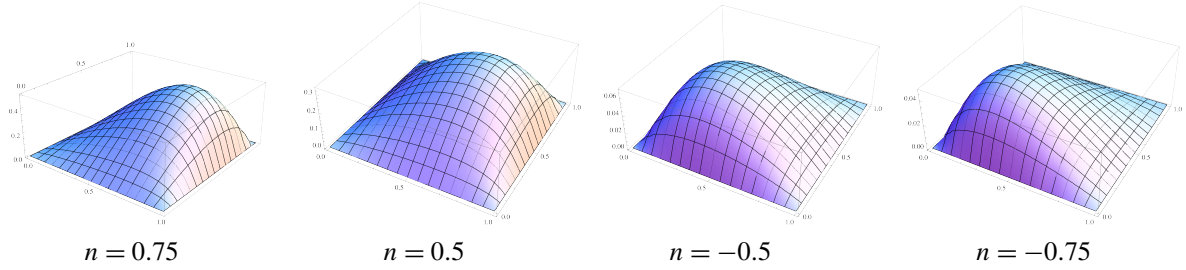


Figure 2. Stress function of an FGM orthotropic bar of square cross-section for $n_1 = n_2 = n$.

4. Numerical experiment

In order to validating the exactness of the proposed algorithm the numerical experiment has been performed. For the convenient of the computer calculations the non-dimensional variables are introduced as

$$X = \frac{x}{a}, \quad Y = \frac{y}{a}, \quad E = \frac{b}{a}, \quad U(X, Y) = \frac{u(x, y)}{a^2 G_0}, \quad F_1(X, Y) = \frac{G_0}{G_{23}(x, y)}, \quad F_2(X, Y) = \frac{G_0}{G_{13}(x, y)} \quad (26)$$

where a, b are characteristic geometrical dimensions of the bar's cross-section and the constant G_0 has dimension of the elastic moduli.

The function used during the tests is the thin plate spline RBF described by the formula

$$\varphi_k(X, Y) = (R_k)^2 \ln(R_k), \quad (27)$$

where $R_k = \sqrt{(X - X_k)^2 + (Y - Y_k)^2}$.

The others parameters of the MFS are following, the tolerance d is equal to 0.00001. The boundary points, the approximation points and the source points are distributed uniformly. The source contour is similar to boundary contour and the distance between them s is 0.2. The number of approximation points $Nw = 441$, the number of boundary points $Nb = 80$, the number of source points $Ns = 80$. The functions describing the inhomogeneity of the material are expressed by the formulas

$$F_1 = e^{-n_1 \pi X}, \quad F_2 = e^{-n_2 \pi Y}. \quad (28)$$

In the example torsion of a bar of a square cross section is considered. The Prandtl stress function in case when n_1 is equal to n_2 is presented in Figure 2. It is easy to observe that the calculated stress function fulfils the boundary condition.

Moreover, if the values of coefficients n_1 and n_2 tend to zero, we approach to homogeneous and isotropic material (see Figure 2). Then analytical solution for the stress function is available and is given by

$$U_a(X, Y) = X(1 - X) - 8 \sum_{k=1,3,\dots}^{\infty} \frac{\sinh(k\pi(1 - Y)) + \sinh(k\pi Y)}{k^3 \pi^3 \sinh(k\pi)} \sin(k\pi X). \quad (29)$$

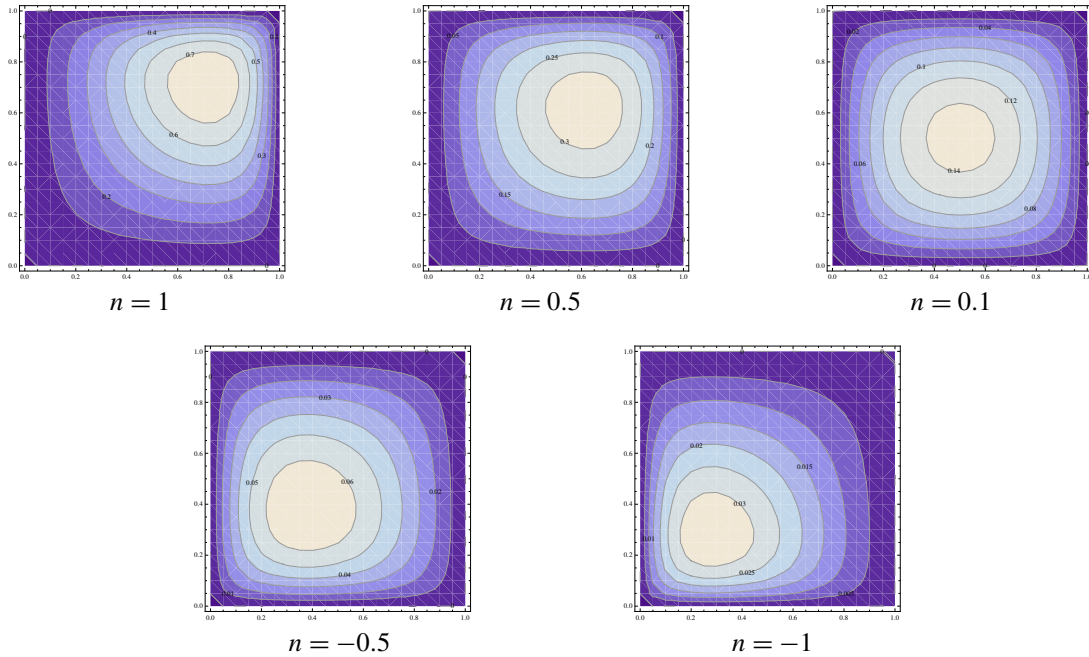


Figure 3. Contour map of the stress function of an FGM orthotropic bar of square cross-section for $n_1 = n_2 = n$.

Comparison of Figure 3, top right, with Figure 4, left, confirms convergence of results to homogeneous and isotropic case if the coefficients n_1 and n_2 tend to zero. This argues the correctness of the results obtained. The absolute value of the difference between the analytical solution for a homogeneous and isotropic bar and the solution calculated for a orthotropic functionally graded bar in the case $n_1 = n_2 = 0$ is presented in Figure 4, right. The largest errors, occurring at the corners, are caused of a deficiency in the numerical method. In the method of fundamental solution the maximal errors are localized in corners

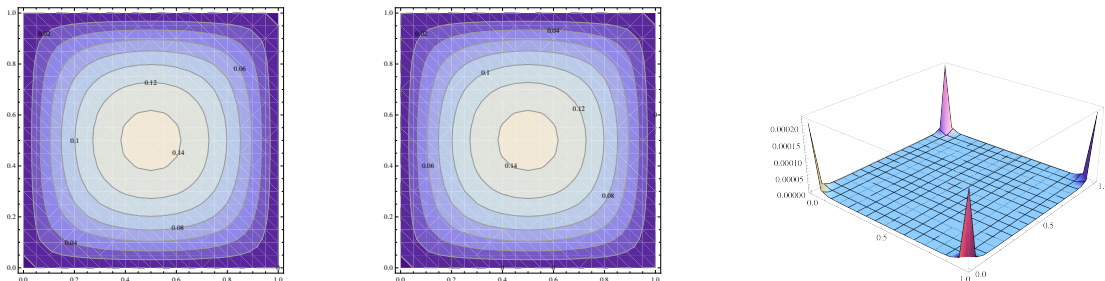


Figure 4. Left: Analytical solution for a homogeneous isotropic bar of square cross-section: — the contour map of the stress function. Middle: Contour map of the stress function of an FGM orthotropic bar for $n_1 = n_2 = 0$. Right: Plot of the absolute value of the difference between the two solutions.

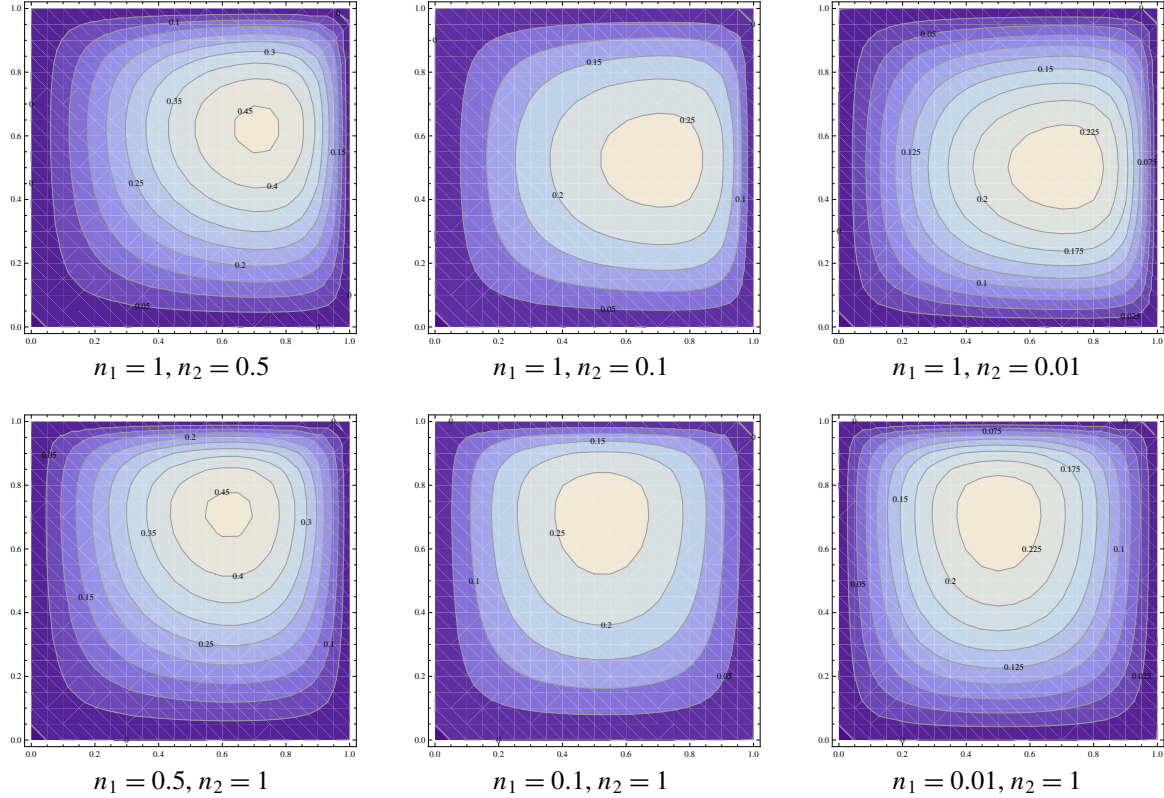


Figure 5. Contour map of the stress function of an FGM orthotropic bar of square cross-section.

of the region. Behind the corners, an error of satisfying the boundary conditions is of order 10^{-5} – 10^{-10} , and error inside the considered region is oscillated among 10^{-8} – 10^{-9} .

Figure 5 shows contour maps of the stress function in case when only one of the coefficients: n_1 or n_2 decreases to zero. This situation refers to functionally graded material with properties of the material changing only in one direction (see the middle and right parts of Figure 5).

Additionally in the method of fundamental solutions obtained approximated solution for the stress function is a continuous function and can be used in the further analysis for instance in stresses calculation. So that on the basis of (3), the resultant of shear stresses is equal to

$$t = \sqrt{t_{xz}^2 + t_{yz}^2}, \quad t_{xz} = \frac{\partial U}{\partial Y}, \quad t_{yz} = -\frac{\partial U}{\partial X}. \quad (30)$$

Here t_{xz} and t_{yz} are shear stresses in non-dimensional form, and

$$t_{xz} = \frac{\sigma_{xz}}{a\theta G_0}, \quad t_{yz} = \frac{\sigma_{yz}}{a\theta G_0}. \quad (31)$$

For example the resultant of shear stresses of the investigated rod in case if coefficients n_1 and n_2 equal to each other, are presented in Figure 6. The maximal values of the shear stresses are obtained on the boundary, in the half-length side of the square. It is a result of a class of considered material. If in

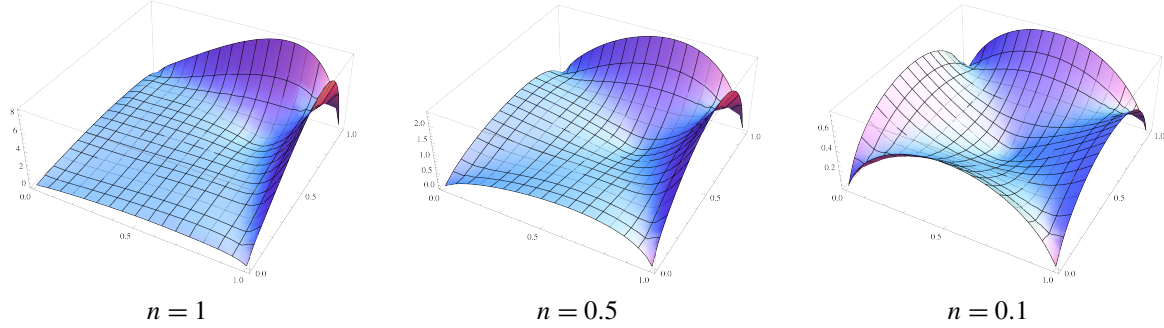


Figure 6. Resultant of the shear stresses of an FGM orthotropic bar for $n_1 = n_2 = n$.

relations (28) exponents n_1 or/and n_2 tends to zero, functions describing elastic moduli limit to constant values. Therefore the properties of this material reflect the properties of homogeneous one and the maximal stresses occur on the boundary.

The other considered example is done for the orthotropic material defined by the characteristics

$$F_1(X) = G_1 e^{-n\pi X}, \quad F_2(X) = G_2 e^{-n\pi X}, \quad (32)$$

where G_1, G_2, n are real numbers. The analytical solution is known for the rectangular region of cross-section with the edges length X_{\max}, Y_{\max} and is given as

$$U_a(X, Y) = \frac{2}{G_1 n \pi} \left(\frac{e^{n\pi/2}}{2 \sinh(n\pi/2)} (e^{n\pi X} - 1) - X e^{n\pi X} \right) - \frac{4}{G_1 \pi^3 (e^{n\pi} - 1)} \sum_{k=1}^{\infty} \frac{e^{n\pi} n^3 \pi + (-1)^k e^{n\pi} (-n^3 \pi + k^2 (-2 + 2e^{n\pi} - n\pi)) + k^2 (2 + e^{n\pi} (-2 + n\pi))}{k(k^2 + n^2)^2} \frac{\sinh(\lambda Y) + \sinh(\lambda(E - Y))}{\sinh(\lambda E)} \sin(k\pi X) \quad (33)$$

where $\lambda = \pi \sqrt{\frac{G_1}{G_2} (k^2 + n^2/4)}$, $E = Y_{\max}/X_{\max}$. For the numerical calculation X_{\max} is taken to be equal to 1.0 and $G_1 = 1.0$. The calculations were made for chosen set of values of material characteristics parameters. The maximum relative error, defined as

$$E_{\max} = \max_{\Omega} \left| \frac{U(X, Y) - U_a(X, Y)}{U_a(X, Y)} \right|, \quad (34)$$

where $\Omega = \{(X, Y) | 0 \leq X \leq X_{\max}, 0 \leq Y \leq Y_{\max}\}$, is presented in Table 1.

As we can observe the error increases with increase of all pointed parameters. The best result is obtained for the case when material parameters tends to the anisotropic material (the lower error for $n = 0.1, G_2 = 2$). Moreover for all values of n and G_2 the best results were achieved for square region (see errors for $Y_{\max} = 1$). And the values of the error included in Table 1 are not high and are of the magnitude acceptable for numerical approach. The detailed results are presented on the example of three versions of the geometry parameter and given in Figures 7, 8 and 9.

Figure 7 consists of Prandtl function calculated for $n = 0.25$ and $G_2 = 2$.

n	G_2	Y_{\max}		
		1	2	3
0.1	2	0.036956	0.075664	0.066276
	3	0.047287	0.081257	0.078933
	4	0.054858	0.089432	0.080912
0.25	2	0.063310	0.070291	0.082494
	3	0.082341	0.093817	0.091832
	4	0.106689	0.100982	0.099155
0.5	2	0.066964	0.074529	0.093456
	3	0.081334	0.090123	0.095321
	4	0.091735	0.098231	0.100028

Table 1. Maximum relative error for a bar of rectangular cross-section.

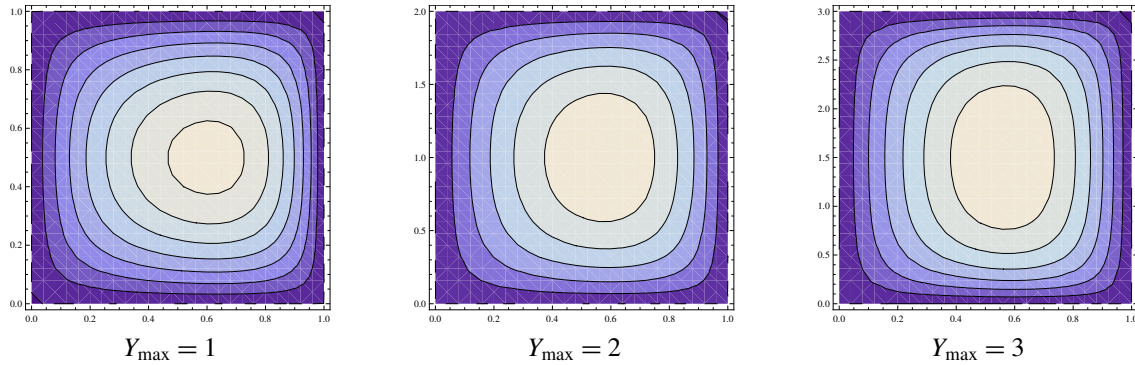


Figure 7. The Prandtl function for $Y_{\max} = 1, 2, 3$.

The assumption that both material characteristics are functions of one variable — X , causes the appearance of one symmetry axes of the bar cross-section. The symmetry axes is the line $Y = Y_{\max}/2$. Using the symmetry property of Prandtl function and the information about the boundary conditions (2) the maximum values of the Prandtl function may be noticed from Figure 8.

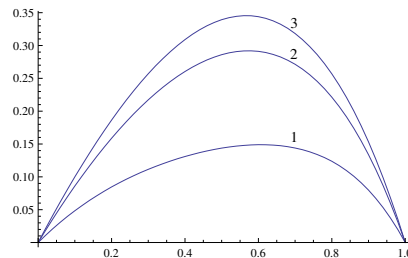


Figure 8. Cross-section of the Prandtl function at $Y = Y_{\max}/2$, for $Y_{\max} = 1, 2, 3$.

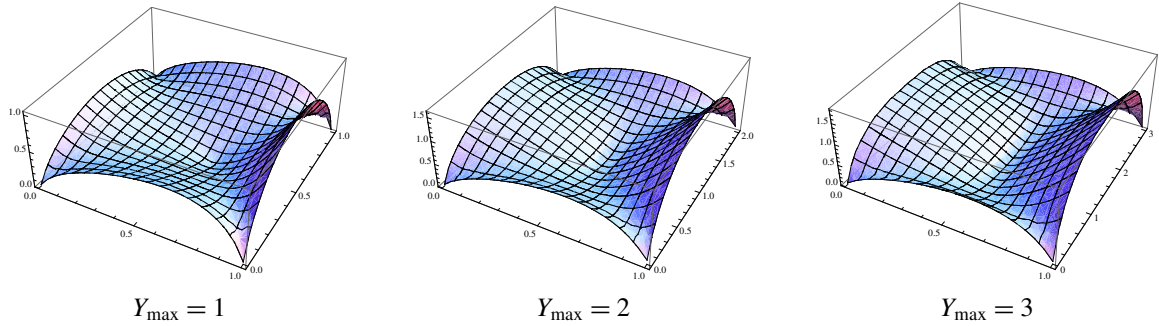


Figure 9. Plots of the shear stress for $Y_{\max} = 1, 2, 3$.

We can observe that the increase of Y_{\max} causes the increase of maximum value achieved by Prandtl function. Moreover for larger values of the Prandtl function becomes steeper. Next figure (Figure 9) consists of plots of shear stresses for considered bar with the rectangular cross-section.

The shear stresses get larger for higher values of geometry parameter Y_{\max} . But for all cases the shear stresses are equal to zero at angles of the bar cross-section. The shear stresses function achieves the local maxima at the middle of each edge of the region Ω . Due to symmetry the solutions on the edges $Y = Y_{\min}$, $Y = Y_{\max}$ are the same, and the maximum value of the shear stress on those edges is the same. On the other pair of edges the shear stress function has different values, so the local maxima are different. One of them (on the edge for $X = X_{\max}$) is the total maximum of the shear stress function.

It is useful to look at the error of the obtained solutions. It is possible to compare the numerically calculated results to the analytical solution (33). The absolute error

$$E_{\text{abs}}(X, Y) = |U(X, Y) - U_a(X, Y)| \quad (35)$$

is plotted on Figure 10. The maximum absolute error appears at point $(0.8, Y_{\max}/2)$ for $Y_{\max} = 1$. The other maximum (local one) is located at $(0.225, Y_{\max}/2)$. For the other presented examples four local maxima appear. For $Y_{\max} = 2$ the local maxima are at points $(0.24, 0.32)$, $(0.24, 1.68)$, $(0.78, 0.32)$, $(0.78, 1.68)$ and the absolute maximum at points $(0.24, 0.32)$, $(0.78, 0.32)$ achieves value 0.0072268255. For the case when $Y_{\max} = 3$ the local maxima are at points $(0.24, 0.36)$, $(0.24, 2.64)$, $(0.78, 0.36)$, $(0.78, 2.64)$ and the absolute maximum at points $(0.24, 0.36)$, $(0.78, 0.36)$ achieves value 0.0067483875. The analysing the error plots gives the conclusion that the applied HAM with FSM is a good tool to solve considered problem with demanded accuracy.

The next considered example is the torsion of the bar of elliptic cross-section. The orthotropic material is defined by the characteristics

$$F_1(X) = G_1 e^{-n\pi X}, \quad F_2(X) = G_2 e^{-n\pi Y}. \quad (36)$$

The influence of the characteristics (36) parameters on the shear stress function is investigated.

First, the special case of ellipse is taken into account, i.e. the circle—ellipse with both axes equal to 1.0.

The range of researched G_1/G_2 parameter is $[1, 3]$. The Prandtl function and shear stress function are plotted in Figure 11 for $G_1/G_2 = 2$.

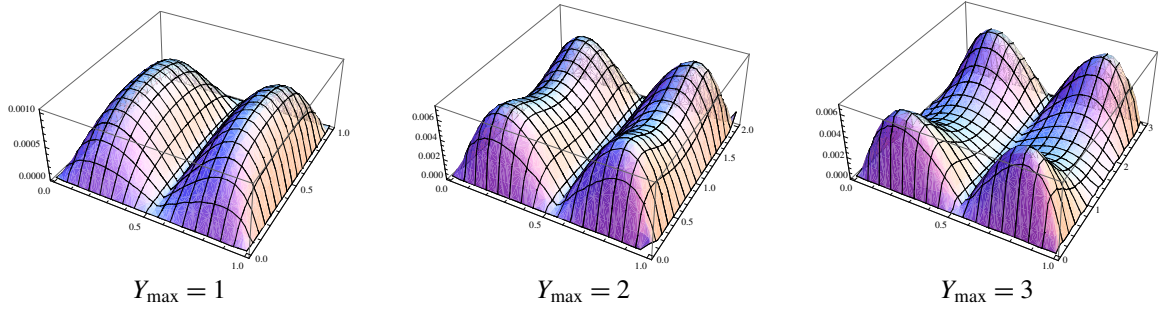


Figure 10. Absolute error of the shear stress for $Y_{\max} = 1, 2, 3$.

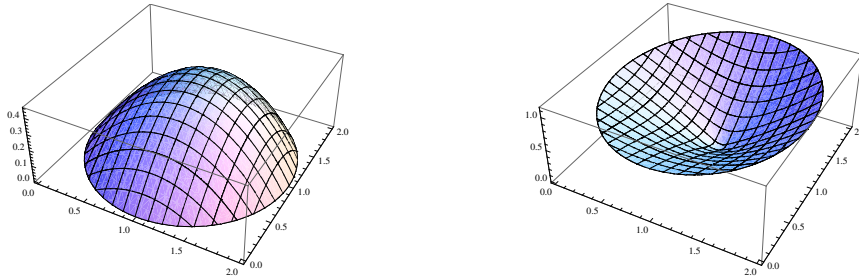


Figure 11. Prandtl function (left) and shear stress (right) for a circular cross-section bar with $G_1/G_2 = 2$.

	U_{\max}	t_{\max}	(X, Y) of t_{\max}
1	0.6844922646	1.6955413372	(1.7289686274, 1.6845471059)
1.5	0.5475682789	1.3554568654	(1.7289686274, 1.6845471059)
2	0.456262953	1.127726558	(1.5877852523, 1.8090169944)
2.5	0.3910543383	0.9650844154	(1.535826795, 1.8443279255)
3	0.3423152275	0.8432450812	(1.4817536741, 1.87630668)

Table 2. Maximum values of the Prandtl function and the shear stress for a circular cross-section bar.

The Prandtl function has one maximum 0.456262953 at point (1.08571, 1.08571). The boundary condition states that the Prandtl function should have value 0.0, and in Figure 11, left, we can see that the boundary condition is fulfilled. Moreover, the shear stress function achieves the minimum value the point (1.08571, 1.08571), which is consistent with physical and mathematical relation of Prandtl and shear stress functions. The maximum value of the shear stress function appears at the boundary, at the point (1.5877852523, 1.8090169944) and has value 1.127726558.

The parameter G_1/G_2 impacts on the maximum value of both the Prandtl function U_{\max} and shear stress t_{\max} . In Table 2 the dependence of U_{\max} and t_{\max} on parameter G_1/G_2 is shown. For the G_1/G_2 greater than 1.0 the dependence possess the nonlinear decreasing character. The maximum of the Prandtl function appears at the same point. The maximum of the stress function is achieved in different point, but these point is always the boundary point.

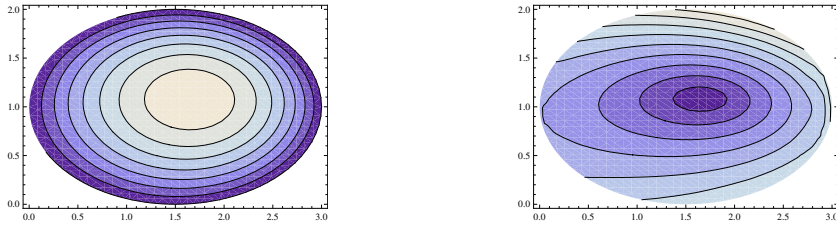


Figure 12. Contour maps of the Prandtl function (left) and the shear stress (right) for an elliptic cross-section bar with $G_1/G_2 = 2$.

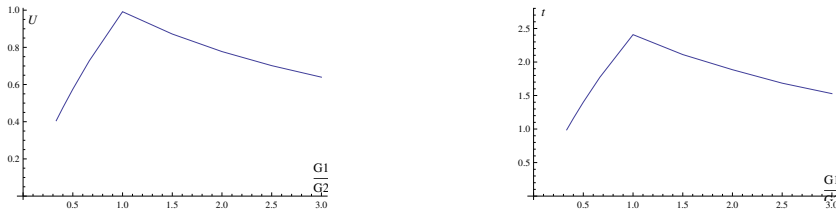


Figure 13. Dependence of the Prandtl function (left) and the shear stress (right) of the elliptic cross-section bar on the parameter G_1/G_2 .

In next example we show the influence of material parameters on the stress function appeared in the torsion of the bar with elliptical cross-section. The ratio of ellipse axis is equal to $3/2$. The range of researched G_1/G_2 parameter is $(0, 3]$. The Prandtl function and the shear stress function are plotted in Figure 12 for $G_1/G_2 = 2$. It is more convenient to use contour plots to observe the minima and maxima of these functions. The maximum of the Prandtl function (Figure 12a) has value of 0.575079 and is places at point $(1.54286, 1.08571)$. At the same point the shear stress function (see Figure 12b) achieves the minimum. The maximum of value 1.40104 is achieved by the shear stress function at point $(1.75308, 1.98566)$, which is the boundary point.

The plots given in Figure 13 present the dependence of the maximum values of Prandtl function and the shear stress on the parameter G_1/G_2 . For both functions the dependence has nonlinear character. In the range of G_1/G_2 in $(0, 1]$ the dependence is increasing function, for G_1/G_2 in $(1, 3]$ is decreasing one.

We have also consider the bar with cross-section of triangle shape. The triangle has the base of unit length and the subtend angle equal to $\pi/2$. The characteristics of the material is given by the formula (36). The top two plots in Figure 14 show the Prandtl and shear stress function for $G_1/G_2 = \frac{1}{2}$. We notice that the maximum of the Prandtl function lays on the triangle height perpendicular to the base and has value 0.0198738. The shear stress function has two maxima. They are achieved at the boundary edges, which are not the base. The other situation for the shear stress appears when parameter G_1/G_2 is greater then 1.0. Next we look at the bottom plots in Figure 14, corresponding to $G_1/G_2 = 2$. The maximum of the Prandtl function lies on the triangle height perpendicular to the base, as well. But the shear stress function has only one maximum, which lies exactly on the middle of base edge.

In Table 3 the values and coordinates of maxima of the Prandtl and the shear stress functions are presented. The functions of maximum value of Prandtl function and the shear stress with respect to the

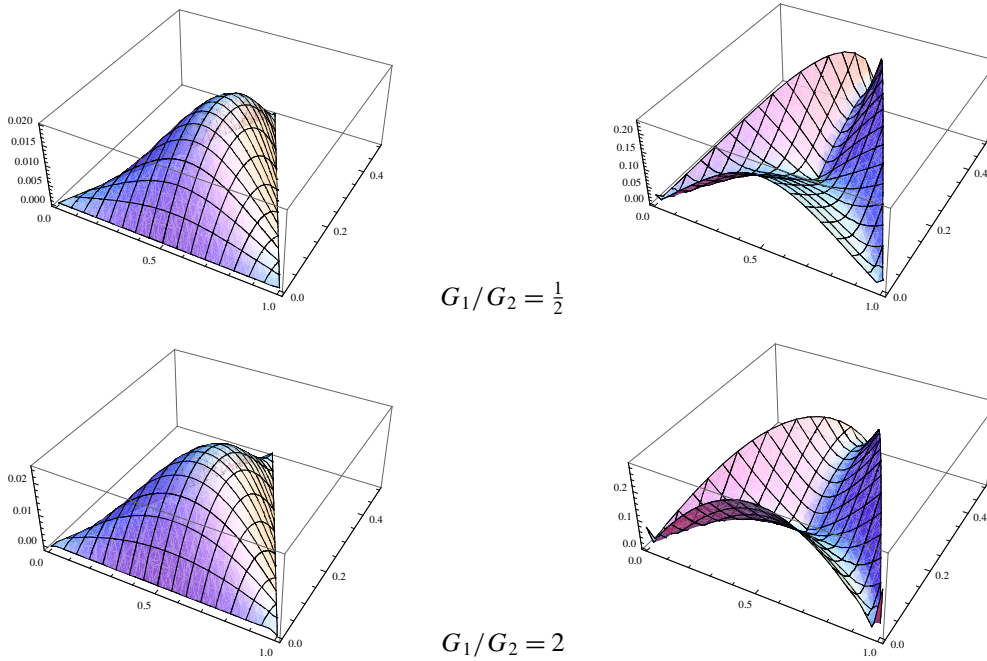


Figure 14. Plots of the Prandtl function (left) and the shear stress (right) for a triangular cross-section bar with $G_1/G_2 = \frac{1}{2}$ (top) and $G_1/G_2 = 2$ (bottom).

G_1/G_2	U_{\max}	(X, Y) for U_{\max}	t_{\max}	(X, Y) for t_{\max}
$\frac{1}{3}$	0.0198738	(0.5, 0.216667)	0.230903	(0.63333, 0.366667)
$\frac{2}{3}$	0.0244673	(0.5, 0.215555)	0.280835	(0.6375, 0.3625)
1	0.0322929	(0.5, 0.2)	0.361319	(0.66667, 0.33333)
$\frac{3}{2}$	0.0277619	(0.5, 0.199999)	0.309816	(0.5, 0.)
2	0.0246664	(0.5, 0.183333)	0.289877	(0.5, 0.)

Table 3. Values and coordinates of the Prandtl and the shear stress function for a triangular cross-section.

parameter G_1/G_2 are nonlinear and increasing for G_1/G_2 in $(0, 1]$, for G_1/G_2 in $[1, 2]$ these functions become decreasing. The points, at which the maximum of Prandtl function appears, are placed on the triangle height perpendicular to the base and distance between these points and the triangle base decreases with increase of parameter G_1/G_2 . The position of points, at which the shear stress has maximum value, depends on G_1/G_2 in following way. For G_1/G_2 in $(0, 1]$ there are exists two maxima, at edges which are not base edge. In this case the position of the maximum points is symmetrical, and the height perpendicular to the triangle base is the axis of symmetry. The position of these points changes with the changes of G_1/G_2 . If tends G_1/G_2 to 0.0 the maximum point coordinates tend to the triangle vertex subtend to the base. When G_1/G_2 achieves 1.0 the maximum points are places exactly at the middles of the edges which are not base. When G_1/G_2 is greater than 1.0 the shear stress function has one maximum, which is exactly in the middle of the triangle base.

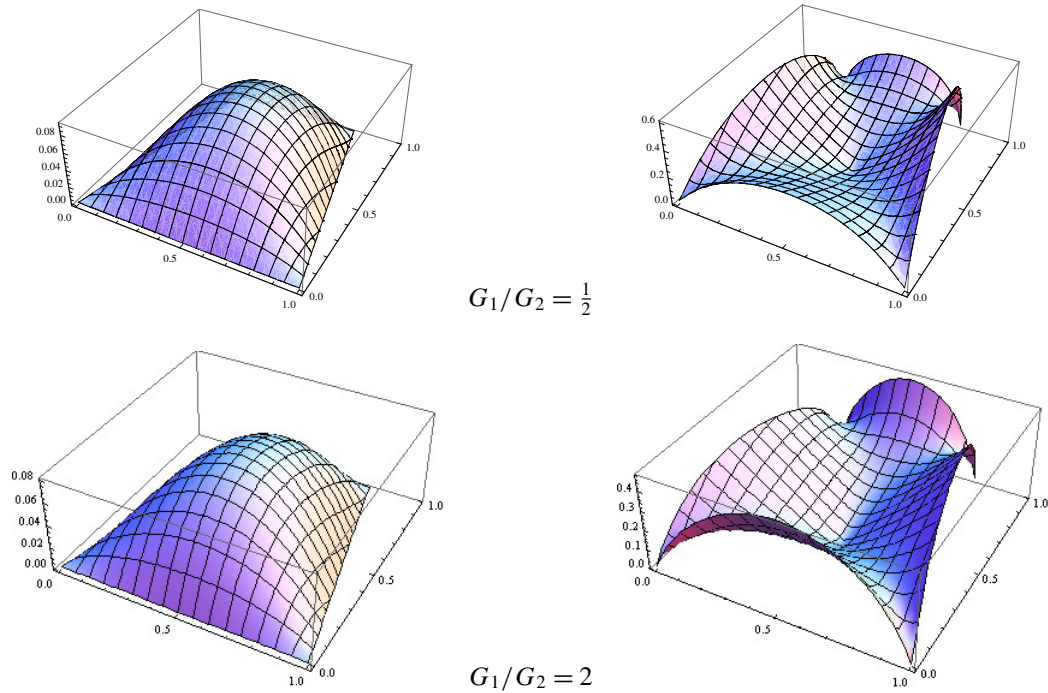


Figure 15. Plots of the Prandtl function (left) and the shear stress (right) for a trapezoidal cross-section bar with $G_1/G_2 = \frac{1}{2}$ (top) and $G_1/G_2 = 2$ (bottom)

The proposed numerical approach can be used for every shape of the bar cross-section. In this paper the rectangular, elliptic and triangular cross-sections have been tested. The other proposal is to take into account trapezoidal bar. The longer base edge of trapezoid has unit length. The geometrical parameter Δx , which is the half of difference of two parallel edges of the trapezoid, is introduced.

First, the orthotropic material is taken as in formula (36) with $G_1 = 1$, $G_2 = 2$, $n = 0.1$. The Prandtl function and the shear stress are shown in the top two plots of Figure 15 for $\Delta x = 0.2$. Due to the symmetry of the considered region, the plotted solutions are the symmetric functions, as well. The maximum value of the Prandtl function appears at the point which is placed on the axis of symmetry. The distance of the maximum point from the longer of parallel edges is equal to 0.514286. The maximum value of the shear stress appears on the boundary. The plot presented in Figure 15, top right, shows two maxima (of value 0.603268) on the nonparallel edges of the trapezoid. The other calculations showed that the shear stress function possess two maxima for G_1/G_2 in the range $(0, 1]$. When tends G_1/G_2 to 0.0 the position of maximum points tends to the vertex at the shorter of parallel edges. For $G_1/G_2 = 1$ maxima are placed at the middle of nonparallel edges.

When $G_1/G_2 = 2$, the Prandtl function (Figure 15, bottom left) possesses a maximum, located on the symmetry axis at the same distance from the longer of parallel edges as for $G_1/G_2 = \frac{1}{2}$. There exists one maximum of the shear stress function (Figure 15, bottom right), placed on the middle of the longer of parallel edges. For the limitary case, when $\Delta x = 0.0$, trapezoid becomes square and the second maximum appears on the parallel edge.

As we showed in some numerically solved examples, the proposed numerical algorithm is a good tool for solving the torsion of the bar made of functionally graded materials. In the numerical experiment we performed validation of the solutions using analytical solutions, known for some special cases. And, we showed that the numerical simulations may be done for testing engineering systems, taking into account values of material, geometry and numerical method parameters of certain ranges.

5. Conclusions

The homotopy analysis method combined with the meshfree method has been implemented for solving the torsion problem of functionally graded bar with orthotropic symmetry. The numerical experiment has been performed to check the accuracy and the convergence of the proposed method. The advantage of the presented algorithm is easy verification of property calculations, because the precision of the obtained numerical results is confirmed by checking the fulfillment of the boundary conditions. Moreover the obtained solution is a continuous function and can be used in the future analysis for instance in calculation of shear stresses. It is necessary to mention that the functions describing the shear flexibility moduli may be arbitrary functions (continuous and differentiable) of cross-sectional coordinates, and it confirms universality of the proposed method. The further analysis is required for other types of radial basis functions and more complicated shapes of cross-sections or the other classes of FGMs.

Acknowledgments

This paper was financially supported by Grant 02/21/DSPB/3453 at Poznan University of Technology. The essence of this work was presented during the conference The International Symposium on Trends in Continuum Physics (TRECOP 2014).

Appendix

The generalized Hooke's law in case of orthotropic symmetry

$$\begin{bmatrix} \epsilon_{xx} \\ \epsilon_{yy} \\ \epsilon_{zz} \\ \epsilon_{yz} \\ \epsilon_{xz} \\ \epsilon_{xy} \end{bmatrix} = \begin{bmatrix} a_{11} & a_{12} & a_{13} & 0 & 0 & 0 \\ a_{12} & a_{22} & a_{23} & 0 & 0 & 0 \\ a_{13} & a_{23} & a_{33} & 0 & 0 & 0 \\ 0 & 0 & 0 & a_{44} & 0 & 0 \\ 0 & 0 & 0 & 0 & a_{55} & 0 \\ 0 & 0 & 0 & 0 & 0 & a_{66} \end{bmatrix} \begin{bmatrix} \sigma_{xx} \\ \sigma_{yy} \\ \sigma_{zz} \\ \sigma_{yz} \\ \sigma_{xz} \\ \sigma_{xy} \end{bmatrix} \quad (\text{A.1})$$

where the elements of the compliance matrix a_{ij} are given in terms of engineering properties by

$$\begin{bmatrix} \epsilon_{xx} \\ \epsilon_{yy} \\ \epsilon_{zz} \\ \epsilon_{yz} \\ \epsilon_{xz} \\ \epsilon_{xy} \end{bmatrix} = \begin{bmatrix} 1/E_1 & \nu_{12}/E_2 & \nu_{13}/E_3 & 0 & 0 & 0 \\ \nu_{12}/E_2 & 1/E_2 & \nu_{23}/E_3 & 0 & 0 & 0 \\ \nu_{13}/E_3 & \nu_{23}/E_3 & 1/E_3 & 0 & 0 & 0 \\ 0 & 0 & 0 & 1/G_{23} & 0 & 0 \\ 0 & 0 & 0 & 0 & 1/G_{13} & 0 \\ 0 & 0 & 0 & 0 & 0 & 1/G_{12} \end{bmatrix} \begin{bmatrix} \sigma_{xx} \\ \sigma_{yy} \\ \sigma_{zz} \\ \sigma_{yz} \\ \sigma_{xz} \\ \sigma_{xy} \end{bmatrix} \quad (\text{A.2})$$

E_1, E_2, E_3 — Young moduli, $\nu_{12}, \nu_{13}, \nu_{23}$ — Poisson ratios, G_{12}, G_{13}, G_{23} — shear moduli.

References

- [Birman and Byrd 2007] V. Birman and L. W. Byrd, “Modeling and analysis of functionally graded materials and structures”, *Applied Mechanics Reviews* **60**:5 (09/01 2007), 195–216.
- [Chen 2011] T. Chen, “A novel class of graded cylinders neutral to host shafts of arbitrary cross-sections under torsion”, *Mechanics Research Communications* **38**:1 (2011), 68–71.
- [Ecsedi 2013] I. Ecsedi, “Some analytical solutions for Saint-Venant torsion of non-homogeneous anisotropic cylindrical bars”, *Mechanics Research Communications* **52** (2013), 95–100.
- [Horgan and Chan 1998/99] C. O. Horgan and A. M. Chan, “Torsion of functionally graded isotropic linearly elastic bars”, *J. Elasticity* **52**:2 (1998/99), 181–199.
- [Jha et al. 2013] D. K. Jha, T. Kant, and R. K. Singh, “A critical review of recent research on functionally graded plates”, *Composite Structures* **96** (2013), 833–849.
- [Kołodziej and Fraska 2005] J. A. Kołodziej and A. Fraska, “Elastic torsion of bars possessing regular polygon in cross-section using BCM”, *Computers & Structures* **84**:1–2 (2005), 78–91.
- [Lekhnitskii 1977] S. G. Lekhnitskii, Теория упругости анизотропного тела, 2nd ed., Nauka, Moscow, 1977. Translated as *Theory of elasticity of an anisotropic body*, Mir, Moscow, 1981.
- [Liao 1997] S.-J. Liao, “Homotopy analysis method: a new analytical technique for nonlinear problems”, *Communications in Nonlinear Science and Numerical Simulation* **2**:2 (1997), 95–100.
- [Miyamoto et al. 1999] Y. Miyamoto, W. A. Kaysser, B. H. Rabin, A. Kawasaki, and R. G. Ford (editors), *Functionally graded materials: design, processing and applications*, Materials Technology Series **5**, Springer, New York, 1999.
- [Naghdi 1994] A. K. Naghdi, “Torsion of rectangular bars with multiple cylindrical reinforcement or cavities”, *Journal of Applied Mechanics* **61**:2 (06/01 1994), 483–487.
- [Nowacki 1970] W. Nowacki, *Teoria sprężystości*, Państwowe Wydawnictwo Naukowe, Warszawa, 1970.
- [Timoshenko and Goodier 1970] S. P. Timoshenko and J. N. Goodier, *Theory of elasticity*, 3rd ed., McGraw-Hill, New York, 1970.
- [Uściłowska 2008] A. Uściłowska, *Rozwiązywanie wybranych zagadnień nieliniowych mechaniki metodą rozwiązań podstawowych*, Wydawnictwo Politechniki Poznańskiej, Poznań, 2008.
- [Uściłowska 2010] A. Uściłowska, “Implementation of the method of fundamental solutions and homotopy analysis method for solving a torsion problem of a rod made of functionally graded material”, *Advanced Materials Research* **123–125** (Aug 2010), 551–554.
- [Xu et al. 2010] R. Xu, J. He, and W. Chen, “Saint-Venant torsion of orthotropic bars with inhomogeneous rectangular cross section”, *Composite Structures* **92**:6 (2010), 1449–1457.

Received 20 Dec 2014. Revised 27 Aug 2015. Accepted 11 Oct 2015.

ANITA UŚCIŁOWSKA: anita.uscilowska@put.poznan.pl

Institute of Materials Technology, Poznan University of Technology, ul. Piotrowo 3, 60-965 Poznań, Poland

AGNIESZKA FRASKA: agnieszka.fraska@put.poznan.pl

Institute of Applied Mechanics, Poznan University of Technology, ul. Jana Pawła II 24, 60-695 Poznań, Poland

THE APPLICATION OF THE METHOD OF FUNDAMENTAL SOLUTIONS IN MODELING AUXETIC MATERIALS

TOMASZ WALCZAK, GRAZYNA SYPNIEWSKA-KAMIŃSKA,
BOGDAN T. MARUSZEWSKI AND KRZYSZTOF W. WOJCIECHOWSKI

The paper presents an application of the method of fundamental solutions to model auxetic materials. The utility of the method has been illustrated by solution of basic elastostatic problem of searching displacements distribution for materials with different auxetic properties. Some remarks on most often difficulties occurring during computational process are also included. The presented numerical examples show that the method of fundamental solutions could be effective numerical tool for researching various properties of auxetic materials.

1. Introduction

Solving many modern engineering problems it requires to use more and more advanced computational methods. Due to high progress in developing those methods in recent years, it was possible to take into account many important and complex problems especially in the field of mechanics, bioengineering or material science. In that domain, where the real problems could be described by differential equations, the main numerical tool to provide computer simulation is the finite element method (FEM) [Zienkiewicz and Taylor 2000]. That method is also most commonly used for describing materials of new properties and their nontrivial behaviors.

In this paper an alternative numerical method has been used to solve elastostatic problems for materials with negative Poisson's ratio as isotropic auxetic materials. The presented method, called Method of Fundamental Solutions (MFS), is a numerical method for solving boundary problems of differential equations, which belongs to the group of meshless methods. That method has been developed by Kupradze and Alexidze [Kupradze 1967; Kupradze and Aleksidze 1964]. Till now, MFS was successfully applied to solve mechanical problems [Bogomolny 1985; Fairweather et al. 2003; Goldberg 1995; Kita 2003; Mathon and Johnston 1977; Poullikkas et al. 2001], and also the elastic ones [Karageorghis and Fairweather 2000; de Medeiros et al. 2004; Poullikkas 1998; Poullikkas et al. 2002]. The main advantage of MFS is a possibility to obtain (with the help of numerical approximation) analytical solution of the problem in the entire considered region. One can obtain the solution by solving just one system of linear equations. That fact simplifies the numerical procedures and calculations and gives a possibility to control the approximation errors on the linear algebra level.

Some papers show that even in three-dimensional cases, the method could be effective and really fast [Maruszewski et al. 2014]. Despite advantages of presented method it is still not commonly used

The paper has been supported by 02/21/DSPB/3463 grant.

Keywords: auxetics, method of fundamental solutions.

in material science field. In a recent authors' publication they proved, that it could be useful tool for searching and modeling of modern materials [Walczak et al. 2014].

In this paper authors focused on modeling the group of materials of unusual mechanical properties, which Poisson's ratio (PR) [Landau and Lifshitz 1986; Alderson et al. 2014] is negative. For common materials PR is positive and if PR is negative, the body shrinks/expands transversally when compressed/stretched. Such kind of materials we call auxetics and they were taken under considerations already in eighties last century [Almgren 1985; Lakes 1987], although their properties [Gilat and Aboudi 2013; Lim 2004; Yang et al. 2013] and structures [Gaspar et al. 2011; Wojciechowski 2003; Chen et al. 2009] are still under intensive studies. In this context, developing of new numerical methods to simulate them and to investigate various models seem to be important and are in particular interest.

The aim of the present paper is to show utility of described method as an excellent tool to investigate uncommon behavior of materials with auxetic properties. It is continuation of authors' study on developing of the MFS [Walczak et al. 2014] and to the best of their knowledge, the MFS method is used in this paper for the first time in such investigations.

The structure of the paper is as follows. Mathematical model with governing equations for the studied model is presented in Section 2. In Section 3 the MFS is briefly sketched, and the fundamental solutions for the basic differential equations of the given problems are presented. Computer simulations are discussed in Section 4, where the utility of the method is illustrated by solving the basic elastostatic problem of searching displacement distribution in materials with different auxetic properties. Moreover, a comparison to existing investigations and method used to consider the above problem has been also presented. Summary and conclusions are presented in Section 5.

2. Mathematical model of the problem

In the paper a three-dimensional problem of equilibrium of a solid has been solved numerically using the method of fundamental solutions (MFS). The body is assumed as homogeneous, isotropic and linearly elastic one. The last assumption, in practice, is satisfied only when small deformations are taken into account. Moreover, we assume that the material properties are constant (i.e., they do not depend on time for instance). The mechanical response of such a solid due to a given loading is unambiguously determined by two material constants. In continuum mechanics the Lamé constants λ and μ are usually used. In literature devoted to the various engineering applications in the role of the two necessary material constants appear rather Young's modulus E and Poisson's ratio (PR) ν . The relationship between those material constants are as follows so:

$$\lambda = \frac{\nu E}{(1 + \nu)(1 - 2\nu)}, \quad \mu = \frac{E}{2(1 + \nu)}. \quad (1)$$

The modulus of elasticity E and the constant μ (i.e., the shear modulus) are always positive. However Poisson's ratio and the Lamé constant λ may be negative, although for most solids they are also positive. In the branch of physics dedicated to auxetic materials, which develops recently rapidly, more popular is associating special features of auxetic solids with the negative values of PR.

Let us denote by Ω the region in space occupied by the body. It is bounded by a surface $\partial\Omega$ which should be piecewise smooth. According to all previously mentioned assumptions, the equilibrium of the considered solid is described by the Cauchy–Navier equations. In the absence of external body forces,

they take the homogeneous form [Poullikkas 1998; Poullikkas et al. 2002]:

$$\mu \nabla \cdot (\nabla \mathbf{u}) + (\lambda + \mu) \nabla (\nabla \cdot \mathbf{u}) = \mathbf{0}, \quad (2)$$

where \mathbf{u} is the displacement vector at the point $\mathbf{x} = (x_1, x_2, x_3)$, and $\mathbf{x} \in \Omega$.

On the surface $\partial\Omega$ we postulate the boundary conditions of mixed type. Let $\partial\Omega_I$ be a part of $\partial\Omega$, on which the Dirichlet boundary conditions are given. Therefore, we can write:

$$\mathbf{u}(\mathbf{x}^B) = \mathbf{f}(\mathbf{x}^B), \quad (3)$$

where $\mathbf{x}^B \in \partial\Omega_I$, and $\mathbf{f}(\mathbf{x}^B)$ is a known vector function.

On the other part of $\partial\Omega$, which we denote by $\partial\Omega_{II}$, the Neumann boundary conditions are postulated. We write them as follows:

$$\mathbf{t}(\mathbf{x}^B) = \mathbf{g}(\mathbf{x}^B), \quad (4)$$

where $\mathbf{x}^B \in \partial\Omega_{II}$, \mathbf{t} is the stress vector, and $\mathbf{g}(\mathbf{x}^B)$ is a known vector function describing external traction. It should be noted, that due to existence and uniqueness of the solution of the formulated boundary problem the following relation is required:

$$\partial\Omega_I \cup \partial\Omega_{II} = \partial\Omega, \quad \partial\Omega_I \cap \partial\Omega_{II} = \emptyset. \quad (5)$$

3. Method of fundamental solutions

The equation of equilibrium (2) together with the boundary conditions (3) and (4) form the boundary value problem. The fundamental solutions of this system are in the form

$$G_{ij}(\mathbf{x}, \mathbf{z}) = \frac{(3 - 4\nu)|\mathbf{x} - \mathbf{z}|^2 \delta_{ij} + (x_i - z_i)(x_j - z_j)}{16\pi\mu(1 - \nu)|\mathbf{x} - \mathbf{z}|^3}, \quad (6)$$

where $|\mathbf{x} - \mathbf{z}|$ is the distance between the points \mathbf{x} and \mathbf{z} . One can observe that

$$G_{ij}(\mathbf{x}, \mathbf{z}) = G_{ji}(\mathbf{x}, \mathbf{z}). \quad (7)$$

The solutions given by (6) satisfy the differential equation (2) at each point of the space, except for one point at which it is not defined. Each fundamental solution represents the displacements at the point \mathbf{x} , that are caused by an unit force acting at the source point \mathbf{z} , namely the displacement at the point \mathbf{x} in the direction of the axis x_j which has been caused by the i -th component of the force is equal to the fundamental solution given by (6) [Poullikkas 1998].

Let us consider N source points \mathbf{z}_k , $k = 1, 2, \dots, N$ placed outside the considered body. Then, one can write the solution of the boundary value problem as the linear combination of the fundamental solutions

$$u_i(\mathbf{x}) = \sum_{k=1}^N a_{kj} G_{ij}(\mathbf{x}, \mathbf{z}_k), \quad i = 1, 2, 3, \quad (8)$$

where $\mathbf{x} \in \Omega \cup \partial\Omega$, $\mathbf{z} \in E^3 - (\Omega \cup \partial\Omega)$, a_{kj} are unknown coefficients. One can easily see, that since the singularities of solutions are placed outside the body, any function of the form (8) satisfies the differential equation (2) in the region Ω . However, it should be noticed, that the boundary conditions (3) and (4) may be satisfied only approximately. To do that, one should define the set of collocation points placed on the

surface $\partial\Omega$, which satisfy the boundary conditions. Let us choose M collocation points. Introducing the linear combinations (8) into the boundary conditions we obtain the system of linear equations with $3N$ unknown coefficients a_{kj} :

$$\mathbf{B} \cdot \mathbf{A} = \mathbf{F}, \quad (9)$$

where \mathbf{A} is the $3N$ -dimensional vector of unknown coefficients a_{kj} , \mathbf{F} is the $3M$ -dimensional vector containing the values of known functions f_i at each collocation point. $3M \times 3N$ -dimensional matrix \mathbf{B} consists of the terms which, after a suitable ordering each of the boundary conditions, are multipliers of the unknown coefficients a_{kj} .

Important advantage of the method of fundamental solutions is that the approximate solutions are differentiable. The accuracy of obtained solutions strongly depends on geometry of the problem and location of source points and collocation points. It is well known that in the case of elliptic differential equations, the biggest errors in approximate solutions of the given boundary value problem occur on the boundary of the considered region [Poullikkas et al. 2001; Karageorghis and Fairweather 2000; de Medeiros et al. 2004; Poullikkas 1998; Poullikkas et al. 2002]. It implies that to find the most accurate solution one should place the sets of the collocation points and the source points, respectively to minimize those errors. Also number of points in those sets is the important method parameter. To find some interesting remarks see [Poullikkas 1998; Poullikkas et al. 2002; Maruszewski et al. 2014; Walczak et al. 2014].

4. Numerical simulations

Let us consider a boundary value problem with the mixed boundary conditions. The solid in the shape of a cube with length of the edge 0.1 m, which is shown in Figure 1, is fixed on its one wall $x_1 = 0$. On the opposite wall there is applied the pressure $p = 100$ MPa. The remaining four walls are free of loadings. It means that considered body is stretched in the direction of x_1 axis. Therefore the boundary value problem can be written as

$$\mu u_{i,kk} + (\lambda + \mu) u_{k,ik} = 0, \quad i = 1, 2, 3, \quad \mathbf{x} \in \Omega, \quad (10)$$

$$\mathbf{u}(\mathbf{x}) = 0, \quad \mathbf{x} \in \partial\Omega_1, \quad (11)$$

$$\mathbf{t}(\mathbf{x}) = 0, \quad \mathbf{x} \in \partial\Omega_3 \cup \Omega_4 \cup \Omega_5 \cup \Omega_6, \quad (12)$$

$$\mathbf{t}(\mathbf{x}) = p \mathbf{e}_1, \quad \mathbf{x} \in \Omega_2, \quad (13)$$

where \mathbf{e}_1 denotes the unit vector of the x_1 axis and $\Omega = (0, 0.1) \times (0, 0.1) \times (0, 0.1)$,

$$\partial\Omega_1 = \{\mathbf{x} : x_1 = 0, 0 \leq x_2 \leq 0.1, 0 \leq x_3 \leq 0.1\},$$

$$\partial\Omega_2 = \{\mathbf{x} : x_1 = 0.1, 0 \leq x_2 \leq 0.1, 0 \leq x_3 \leq 0.1\},$$

$$\partial\Omega_3 = \{\mathbf{x} : x_2 = 0, 0 \leq x_1 \leq 0.1, 0 \leq x_3 \leq 0.1\},$$

$$\partial\Omega_4 = \{\mathbf{x} : x_2 = 0.1, 0 \leq x_1 \leq 0.1, 0 \leq x_3 \leq 0.1\},$$

$$\partial\Omega_5 = \{\mathbf{x} : x_3 = 0, 0 \leq x_1 \leq 0.1, 0 \leq x_2 \leq 0.1\},$$

$$\partial\Omega_6 = \{\mathbf{x} : x_3 = 0.1, 0 \leq x_1 \leq 0.1, 0 \leq x_2 \leq 0.1\}.$$

The subject of the numerical experiments is a set of the cubes, which are made of auxetic materials of which Poisson's ratio is from range $\nu = (-0.9, -0.3)$. The original software written in FORTRAN 95

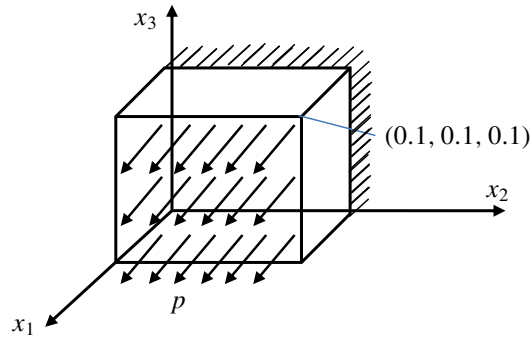


Figure 1. Loads and boundary conditions of considered body.

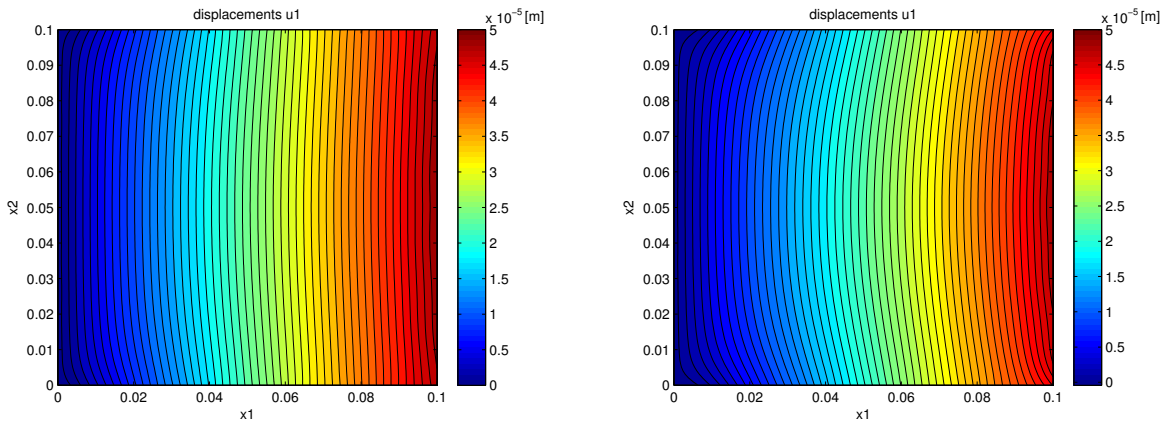


Figure 2. The component u_1 of the displacement vector on the $x_3 = 0.05$ cross-section for the material with $\nu = -0.3$ (left), $\nu = -0.5$ (right).

with implemented MFS was used to simulate behavior of considered group of materials. For each simulation exactly the same number of nodes (collocation points and source points) has been used. One should also notice, that number of applied source points was equal to number of collocation points and was equal to 864 in each considered case. That approach leads always to square main matrix of the system, and authors' experiences show that for mixed boundary conditions it gives the most accurate results.

Often considered problem where MFS is applied is a shape of the surface where the source points are placed. Generally one can find two approaches: one when those points are located on the sphere with the center placed in the middle of considered body having respectively big radius, and the other one when the source points are placed on the surface which shape and distance is very close to that of the considered body. Of course, it is placed outside of the body. In this paper the second way has been applied to all computer simulations (see [Maruszewski et al. 2014]).

In Figure 2 the component u_1 of the displacement vector on the plane $x_3 = 0.05$ is shown for two auxetic materials with $\nu = -0.3$ (left) and $\nu = -0.5$ (right). The observed symmetrical distribution of displacements is consistent with the symmetry of the boundary conditions as well as the load. Fixing only one wall results in the largest displacements close to the opposite one.

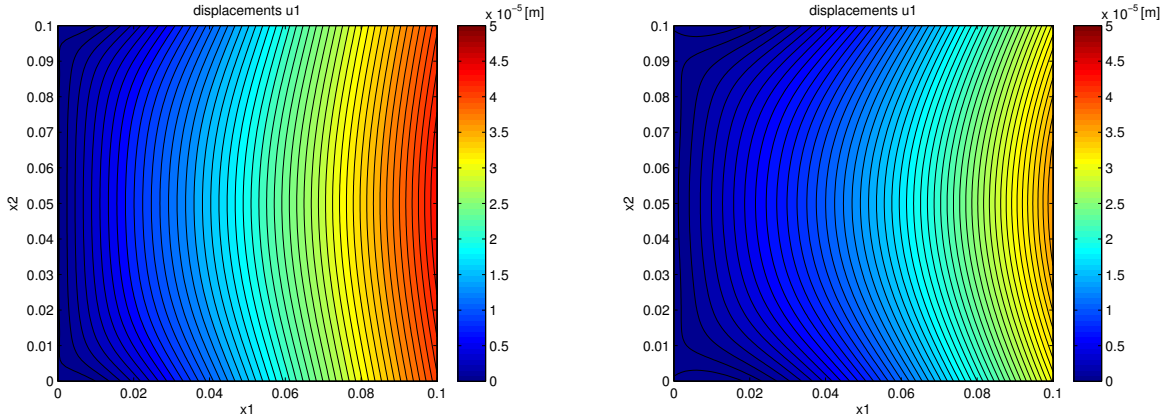


Figure 3. The component u_1 of the displacement vector on the $x_3 = 0.05$ cross-section for the material with $\nu = -0.7$ (left), $\nu = -0.9$ (right).

One can see that these two maps of displacements are similar. The values of the displacement u_1 along the left edge of each half of Figure 2 are zero, which is a consequence of fixing the wall. Positive values of displacements u_1 on the right hand side at both graphs are observed. Stretching state in the direction of x_1 axis and only little difference between values of displacement can also be observed. The situation changes, when we take into account the lower value of Poisson's ratio. In Figure 3 the component u_1 of the displacement vector on the plane $x_3 = 0.05$ is shown for another two auxetic materials with $\nu = -0.7$ (left) and $\nu = -0.9$ (right). One can observe, that there are some irregularities in those distributions occurring near the left corners (close to the fixed wall). Especially, that is visible in the Figure 3 (right), where the regions with different values of displacement component u_1 could be seen. That is not numerical effect, but it corresponds to auxetic nature of the considered body. In classical material this effect doesn't occur.

From the other hand, comparing the map included in Figure 2 to the map in Figure 3 we can observe, that maximal values of the displacement u_1 decrease with decreasing of PR value for considered materials. It should also be noticed, that the lines of the constant displacements are more curved with decreasing of PR value. Analyzing presented maps, one can see, that those lines are less perpendicular to x_1 axis in the case of material with the $\nu = -0.9$ than in the other cases. To visualize in better way the situation, the additional maps were drawn for all cases. In Figure 4 the component u_1 of the displacement vector is shown for materials with $\nu = -0.3$ (left), $\nu = -0.5$ (right), but this time cross-section of the cube was made by the plane $x_1 = x_3$.

Left edge of this map represents the edge of the cube, that is placed along x_2 axis and the right edge is placed along the straight $x_2 = x_3 = 0.1$. One can see that these two maps of displacements are similar to each other. The effect of bending of the lines of constant displacements is also visible what was mentioned earlier, when material has lower value of PR. As can be also seen, the values of displacements u_1 on the fixed walls, are close to zero. Stretching in the direction of x_1 axis, gives positive values of displacements u_1 in whole region of the both graphs. In Figure 5 the component u_1 of the displacement vector is presented for materials with $\nu = -0.7$ (left), $\nu = -0.9$ (right), in cross-section of the cube, that was made by the plane $x_1 = x_3$.

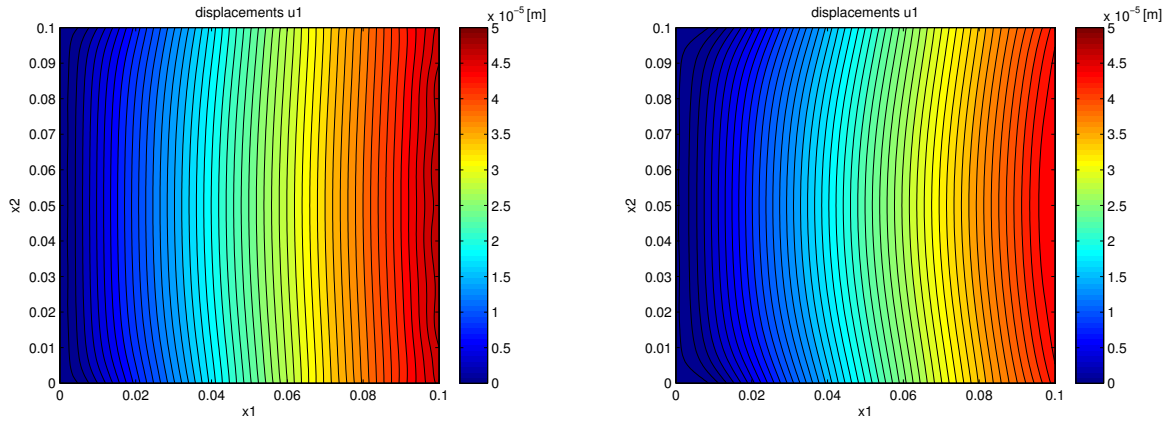


Figure 4. The component u_1 of the displacement vector on the $x_1 = x_3$ cross-section for the material with $\nu = -0.3$ (left), $\nu = -0.5$ (right).

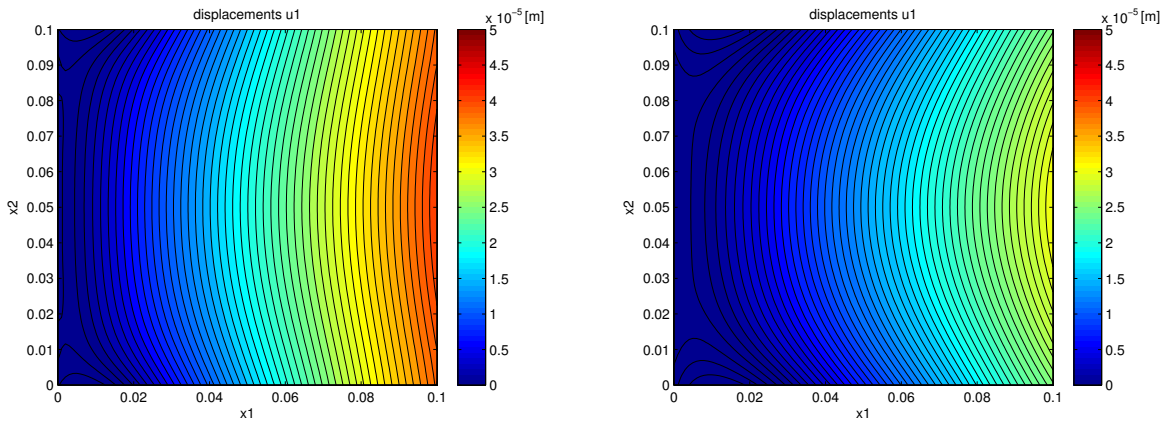


Figure 5. The component u_1 of the displacement vector on the $x_1 = x_3$ cross-section for the material with $\nu = -0.7$ (left), $\nu = -0.9$ (right).

One can see very close similarity between distributions presented in Figure 5 to distributions of displacements shown in Figure 3. For auxetic material with Poisson’s ratio $\nu = -0.7$ and especially for material with $\nu = -0.9$, exactly the same irregularities occur near left boundary. Because cross-section used for creating maps presented in Figure 4 and Figure 5 is diagonal plane for considered cube, it could be seen that the strongest irregularities occur near the cube corners. In comparison to the auxetic materials the classical ones don’t have irregularities in their corners, what one can observe in Figure 6 and Figure 7.

We can also see in Figure 6 and Figure 7 that the isolines representing displacements u_1 for both each of the classical materials are getting parallel with the growth of a distance from fixed walls. The auxetic materials, what is well visible, behave differently.

Generally we can conclude that some interesting effects in auxetics materials could be seen only for lower value of negative Poisson’s ratio (close to -1).

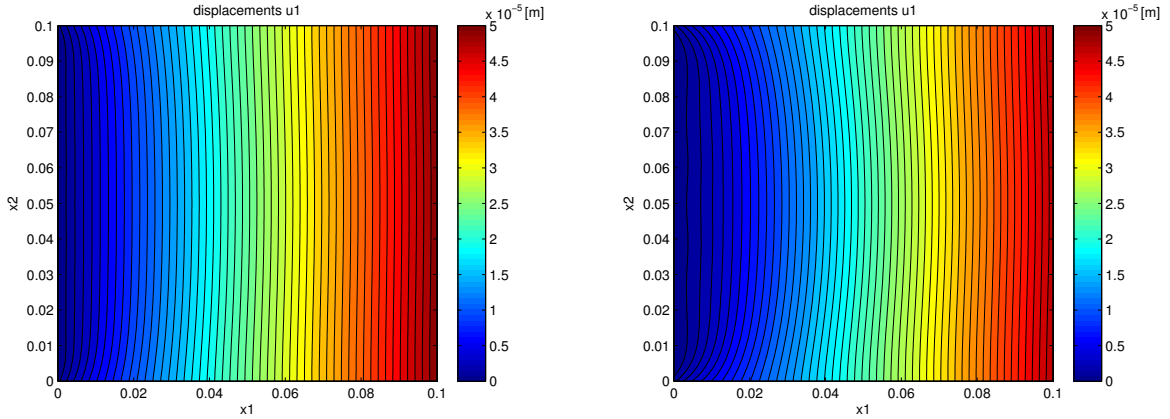


Figure 6. The component u_1 of the displacement vector on the $x_3 = 0.05$ cross-section for the material with $\nu = 0.2$ (left), $\nu = 0.4$ (right).

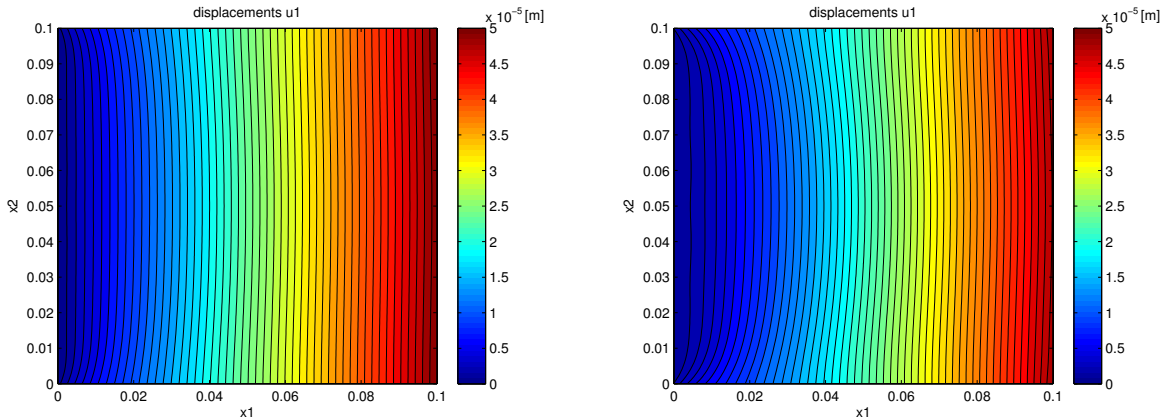


Figure 7. The component u_1 of the displacement vector on the $x_1 = x_3$ cross-section for the material with $\nu = 0.2$ (left), $\nu = 0.4$ (right).

An analysis of the results presented in Figures 2–7 allows us to draw additional important conclusions.

- The results obtained with the help of the fundamental solutions method applied to the basic equations of elasticity (11) of the auxetic continua are practically the same as those obtained by Lakes [1992] who has analyzed de Saint-Venant's principle applied to auxetic elastic materials. It proves that the both methods are equivalent each other. That equivalence results also from the fact that both models do not go beyond the irreversible thermodynamics of continua for normal and auxetic materials. That fact has been shown by Landau and Lifshitz [1986]. Considering the sufficient conditions for a minimum of the Helmholtz free energy in the state of thermodynamic equilibrium, they proved that the value of Poisson's ratio of isotropic materials belongs to the interval $(-1; 0, 5)$.
- From Figures 2–5 it can be seen that if the negative Poisson's ratio is lower, the values of the component $u_{1,1}$ of the displacement gradient are generally smaller.

- Comparing the displacement distribution in the auxetic material to that in the classical one (Figure 5 versus Figure 6 and Figure 7) we see that auxetic occurs faster stiff than normal material if Poisson's ratio decreases.

5. Conclusions

The presented method is effective and fast numerical tool for researching material behavior with different mechanical properties. The biggest advantage of presented method in comparison to FEM is that in the MFS there is no need to define classical mesh of considered body. Numerical procedures used for the mesh generation processes are usually time-consuming ones. In the meshless method one can define only the two sets of points that are not connected to each other. One may also treat it as two clouds of points where one of them is applied to define boundary conditions (collocation points) and the second one should be located just outside the considered body. What is also important (see Section 3) the obtained results have analytical character — of course they are obtained in numerical way, but after solution of just one linear system of equations (9), it is possible to find the displacements field in any point of considered region only using relation (8) and without any additional approximation. It implies the much more effective algorithm to providing numerical simulations especially in three-dimensional cases. Let us underline that all computer simulations have been done during a relative short time (few minutes).

The only problems occurring during the use of the method of fundamental solutions are connected with optimization of parameters like number of collocation points, number of source points or with the choice how source points should be located outside the considered body. It is nontrivial task and it is especially difficult, when one takes into account the boundary value problem with mixed boundary conditions (like in presented example in this paper). Those problems were considered in some publications [Poullikkas 1998; Poullikkas et al. 2002; Maruszewski et al. 2014; Walczak et al. 2014], where authors have tested MFS for such mechanical problems, for which the analytical solutions were known. However, one should notice that the MFS is still under development.

Appendix

To determine the solution of any boundary value problem defined by relations (2)–(4) with use of MFS one should write the system of linear algebraic equations (see (9)). We have assumed the displacement vector in each point $\mathbf{x} \in \Omega \cup \partial\Omega$ as a linear combination defined by (8). To applied Dirichlet's boundary conditions we can rewrite them in the form

$$\begin{aligned} u_1(\mathbf{A}, \mathbf{Z}, \mathbf{x}) &= \sum_{k=1}^N a_{k1} G_{11}(\mathbf{x}, \mathbf{z}_k) + \sum_{k=1}^N a_{k2} G_{12}(\mathbf{x}, \mathbf{z}_k) + \sum_{k=1}^N a_{k3} G_{13}(\mathbf{x}, \mathbf{z}_k), \\ u_2(\mathbf{A}, \mathbf{Z}, \mathbf{x}) &= \sum_{k=1}^N a_{k1} G_{21}(\mathbf{x}, \mathbf{z}_k) + \sum_{k=1}^N a_{k2} G_{22}(\mathbf{x}, \mathbf{z}_k) + \sum_{k=1}^N a_{k3} G_{23}(\mathbf{x}, \mathbf{z}_k), \\ u_3(\mathbf{A}, \mathbf{Z}, \mathbf{x}) &= \sum_{k=1}^N a_{k1} G_{31}(\mathbf{x}, \mathbf{z}_k) + \sum_{k=1}^N a_{k2} G_{32}(\mathbf{x}, \mathbf{z}_k) + \sum_{k=1}^N a_{k3} G_{33}(\mathbf{x}, \mathbf{z}_k), \end{aligned}$$

where G are fundamental solutions (see (6)), the $3N$ -dimensional vector $\mathbf{Z} = [\mathbf{z}_1, \mathbf{z}_2, \dots, \mathbf{z}_N]$ contains

coordinates of N source points $\mathbf{z}_j = [x_1^j, x_2^j, x_3^j] \in \Omega \cup \partial\Omega$, $j = 1, \dots, N$ and $3N$ -dimensional vector $\mathbf{A} = [a_{11}, a_{21}, \dots, a_{N1}, a_{12}, a_{22}, \dots, a_{N2}, a_{13}, a_{23}, \dots, a_{N3}]$ contains unknown coefficients. If Neumann's boundary conditions have been postulated we can write the stress vector components in the form

$$\begin{aligned} t_1(\mathbf{A}, \mathbf{Z}, \mathbf{x}) &= \sum_{k=1}^N a_{k1} T_{11}(\mathbf{x}, \mathbf{z}_k) + \sum_{k=1}^N a_{k2} T_{12}(\mathbf{x}, \mathbf{z}_k) + \sum_{k=1}^N a_{k3} T_{13}(\mathbf{x}, \mathbf{z}_k), \\ t_2(\mathbf{A}, \mathbf{Z}, \mathbf{x}) &= \sum_{k=1}^N a_{k1} T_{21}(\mathbf{x}, \mathbf{z}_k) + \sum_{k=1}^N a_{k2} T_{22}(\mathbf{x}, \mathbf{z}_k) + \sum_{k=1}^N a_{k3} T_{23}(\mathbf{x}, \mathbf{z}_k), \\ t_3(\mathbf{A}, \mathbf{Z}, \mathbf{x}) &= \sum_{k=1}^N a_{k1} T_{31}(\mathbf{x}, \mathbf{z}_k) + \sum_{k=1}^N a_{k2} T_{32}(\mathbf{x}, \mathbf{z}_k) + \sum_{k=1}^N a_{k3} T_{33}(\mathbf{x}, \mathbf{z}_k), \end{aligned}$$

where $T(\mathbf{x}, \mathbf{z})$ are functions analogous to the functions $G(\mathbf{x}, \mathbf{z})$ and should be defined as

$$T_{11}(\mathbf{x}, \mathbf{z}) = \frac{2\mu}{1-2\nu} \left[(1-\nu) \frac{\partial G_{11}}{\partial x_1} + \nu \frac{\partial G_{21}}{\partial x_2} + \nu \frac{\partial G_{31}}{\partial x_3} \right] n_1 + \mu \left(\frac{\partial G_{11}}{\partial x_2} + \frac{\partial G_{21}}{\partial x_1} \right) n_2 + \mu \left(\frac{\partial G_{11}}{\partial x_3} + \frac{\partial G_{31}}{\partial x_1} \right) n_3,$$

$$\begin{aligned} T_{12}(\mathbf{x}, \mathbf{z}) &= \frac{2\mu}{1-2\nu} \left[(1-\nu) \frac{\partial G_{12}}{\partial x_1} + \nu \frac{\partial G_{22}}{\partial x_2} + \nu \frac{\partial G_{32}}{\partial x_3} \right] n_1 + \mu \left(\frac{\partial G_{12}}{\partial x_2} + \frac{\partial G_{22}}{\partial x_1} \right) n_2 + \mu \left(\frac{\partial G_{12}}{\partial x_3} + \frac{\partial G_{32}}{\partial x_1} \right) n_3 \\ &= T_{21}(\mathbf{x}, \mathbf{z}), \end{aligned}$$

$$\begin{aligned} T_{13}(\mathbf{x}, \mathbf{z}) &= \frac{2\mu}{1-2\nu} \left[(1-\nu) \frac{\partial G_{13}}{\partial x_1} + \nu \frac{\partial G_{23}}{\partial x_2} + \nu \frac{\partial G_{33}}{\partial x_3} \right] n_1 + \mu \left(\frac{\partial G_{13}}{\partial x_2} + \frac{\partial G_{23}}{\partial x_1} \right) n_2 + \mu \left(\frac{\partial G_{13}}{\partial x_3} + \frac{\partial G_{33}}{\partial x_1} \right) n_3 \\ &= T_{31}(\mathbf{x}, \mathbf{z}), \end{aligned}$$

$$T_{22}(\mathbf{x}, \mathbf{z}) = \frac{2\mu}{1-2\nu} \left[\nu \frac{\partial G_{12}}{\partial x_1} + (1-\nu) \frac{\partial G_{22}}{\partial x_2} + \nu \frac{\partial G_{32}}{\partial x_3} \right] n_2 + \mu \left(\frac{\partial G_{22}}{\partial x_1} + \frac{\partial G_{12}}{\partial x_2} \right) n_1 + \mu \left(\frac{\partial G_{22}}{\partial x_3} + \frac{\partial G_{32}}{\partial x_2} \right) n_3,$$

$$\begin{aligned} T_{23}(\mathbf{x}, \mathbf{z}) &= \frac{2\mu}{1-2\nu} \left[\nu \frac{\partial G_{13}}{\partial x_1} + (1-\nu) \frac{\partial G_{23}}{\partial x_2} + \nu \frac{\partial G_{33}}{\partial x_3} \right] n_2 + \mu \left(\frac{\partial G_{23}}{\partial x_3} + \frac{\partial G_{33}}{\partial x_2} \right) n_3 + \mu \left(\frac{\partial G_{23}}{\partial x_1} + \frac{\partial G_{13}}{\partial x_2} \right) n_1 \\ &= T_{32}(\mathbf{x}, \mathbf{z}), \end{aligned}$$

$$T_{33}(\mathbf{x}, \mathbf{z}) = \frac{2\mu}{1-2\nu} \left[\nu \frac{\partial G_{13}}{\partial x_1} + \nu \frac{\partial G_{23}}{\partial x_2} + (1-\nu) \frac{\partial G_{33}}{\partial x_3} \right] n_3 + \mu \left(\frac{\partial G_{33}}{\partial x_2} + \frac{\partial G_{23}}{\partial x_3} \right) n_3 + \mu \left(\frac{\partial G_{33}}{\partial x_1} + \frac{\partial G_{13}}{\partial x_3} \right) n_1,$$

where n_1, n_2, n_3 denote the components of the unit vector normal to the surface $\partial\Omega$.

Finally to find the solution of considered problem we should write the linear system of algebraic equations (9) in the following form:

$$\begin{bmatrix}
 G_{11}(\mathbf{x}^1, \mathbf{z}_1) \cdots G_{11}(\mathbf{x}^1, \mathbf{z}_N) & G_{12}(\mathbf{x}^1, \mathbf{z}_1) \cdots G_{12}(\mathbf{x}^1, \mathbf{z}_N) & G_{13}(\mathbf{x}^1, \mathbf{z}_1) \cdots G_{13}(\mathbf{x}^1, \mathbf{z}_N) \\
 G_{21}(\mathbf{x}^1, \mathbf{z}_1) \cdots G_{21}(\mathbf{x}^1, \mathbf{z}_N) & G_{22}(\mathbf{x}^1, \mathbf{z}_1) \cdots G_{22}(\mathbf{x}^1, \mathbf{z}_N) & G_{23}(\mathbf{x}^1, \mathbf{z}_1) \cdots G_{23}(\mathbf{x}^1, \mathbf{z}_N) \\
 G_{31}(\mathbf{x}^1, \mathbf{z}_1) \cdots G_{31}(\mathbf{x}^1, \mathbf{z}_N) & G_{32}(\mathbf{x}^1, \mathbf{z}_1) \cdots G_{32}(\mathbf{x}^1, \mathbf{z}_N) & G_{33}(\mathbf{x}^1, \mathbf{z}_1) \cdots G_{33}(\mathbf{x}^1, \mathbf{z}_N) \\
 \vdots & \vdots & \vdots \\
 G_{11}(\mathbf{x}^M, \mathbf{z}_1) \cdots G_{11}(\mathbf{x}^M, \mathbf{z}_N) & G_{12}(\mathbf{x}^M, \mathbf{z}_1) \cdots G_{12}(\mathbf{x}^M, \mathbf{z}_N) & G_{13}(\mathbf{x}^M, \mathbf{z}_1) \cdots G_{13}(\mathbf{x}^M, \mathbf{z}_N) \\
 G_{21}(\mathbf{x}^M, \mathbf{z}_1) \cdots G_{21}(\mathbf{x}^M, \mathbf{z}_N) & G_{22}(\mathbf{x}^M, \mathbf{z}_1) \cdots G_{22}(\mathbf{x}^M, \mathbf{z}_N) & G_{23}(\mathbf{x}^M, \mathbf{z}_1) \cdots G_{23}(\mathbf{x}^M, \mathbf{z}_N) \\
 G_{31}(\mathbf{x}^M, \mathbf{z}_1) \cdots G_{31}(\mathbf{x}^M, \mathbf{z}_N) & G_{32}(\mathbf{x}^M, \mathbf{z}_1) \cdots G_{32}(\mathbf{x}^M, \mathbf{z}_N) & G_{33}(\mathbf{x}^M, \mathbf{z}_1) \cdots G_{33}(\mathbf{x}^M, \mathbf{z}_N)
 \end{bmatrix} \times \begin{bmatrix} a_{11} \\ \vdots \\ a_{N1} \\ a_{12} \\ \vdots \\ a_{1N} \\ a_{13} \\ \vdots \\ a_{N3} \end{bmatrix} = \begin{bmatrix} a_{11} \\ \vdots \\ a_{N1} \\ a_{12} \\ \vdots \\ a_{1N} \\ a_{13} \\ \vdots \\ a_{N3} \end{bmatrix},$$

where vector $\mathbf{F} = [f_1^1, f_2^1, f_3^1, \dots, f_1^M, f_2^M, f_3^M]$ contains the value of displacement vector or stress vector components applied in M collocation points. If in any point the Neumann boundary condition is applied, we only have to replace all functions G to the function T , respectively in three rows of the matrix which are written for considered point. If the number of collocation points M is equal to the number of source points N , we obtain square system of $3M = 3N$ equations. It is possible to define more collocation points than sources ($M > N$). In that case, one should find the approximate solution in the least square sense.

After solving of the system and obtaining the vector of coefficients A we can easily determine the displacement vector in each point of the considered body with the help of (8).

References

- [Alderson et al. 2014] K. L. Alderson, A. Alderson, J. N. Grima, and K. W. Wojciechowski, "Auxetic materials and related systems", *Phys. Status Solidi B* **251** (2014), 263–266.
- [Almgren 1985] R. F. Almgren, "An isotropic three-dimensional structure with Poisson's ratio = -1 ", *J. Elasticity* **15** (1985), 427–430.
- [Bogomolny 1985] A. Bogomolny, "Fundamental solutions method for elliptic boundary value problems", *SIAM J. Numer. Anal.* **22**:4 (1985), 644–669.
- [Chen et al. 2009] L. Chen, C. Liu, J. Wang, W. Zhang, C. Hu, and S. Fan, "Auxetic materials with large negative Poisson's ratios based on highly oriented carbon nanotube structures", *Appl. Phys. Lett.* **94** (2009), 253111.
- [Fairweather et al. 2003] G. Fairweather, A. Karageorghis, and P. A. Martin, "The method of fundamental solutions for scattering and radiation problems", *Eng. Anal. Bound. Elem.* **27**:7 (2003), 759–769.
- [Gaspar et al. 2011] N. Gaspar, C. W. Smith, A. Alderson, J. N. Grima, and K. E. Evans, "A generalised three-dimensional tethered-nodule model for auxetic materials", *Journal of Material Science* **46** (2011), 372–384.
- [Gilat and Aboudi 2013] R. Gilat and J. Aboudi, "Behavior of elastoplastic auxetic microstructural arrays", *Materials* **6** (2013), 726–737.
- [Goldberg 1995] M. A. Goldberg, "The method of fundamental solutions for Poisson's equation", *Eng. Anal. Bound. Elem.* **16** (1995), 205–213.
- [Karageorghis and Fairweather 2000] A. Karageorghis and G. Fairweather, "The method of fundamental solutions for axisymmetric elasticity problems", *Comput. Mech.* **25** (2000), 524–532.
- [Kita 2003] E. Kita, "Indirect Trefftz method for boundary value problem of Poisson equation", *Eng. Anal. Bound. Elem.* **27** (2003), 825–833.

- [Kupradze 1967] V. Kupradze, “A method for the approximate solution of limiting problems in mathematical physics”, *U.S.S.R. Comput. Math. Math. Phys.* **4:6** (1967), 199–205.
- [Kupradze and Aleksidze 1964] V. D. Kupradze and M. A. Aleksidze, “The method of functional equations for the approximate solution of certain boundary-value problems”, *Ž. Vyčisl. Mat. i Mat. Fiz.* **4** (1964), 683–715. In Russian; translated in *U.S.S.R. Comput. Math. Math. Phys.* **4:4** (1966), 82–126.
- [Lakes 1987] R. Lakes, “Foam structures with a negative Poisson’s ratio”, *Science* **235** (1987), 1038–1040.
- [Lakes 1992] R. S. Lakes, “Saint-Venant end effects for materials with negative Poisson’s ratios”, *J. Applied Mechanics* **59** (1992), 744–746.
- [Landau and Lifshitz 1986] L. D. Landau and E. M. Lifshitz, *Course of theoretical physics, VII: Theory of elasticity*, 3rd ed., Pergamon Press, Oxford, 1986.
- [Lim 2004] T. C. Lim, “Elastic properties of a Poisson–Shear material”, *Journal of Material Science* **39** (2004), 4965–4969.
- [Maruszewski et al. 2014] B. T. Maruszewski, G. Sypniewska-Kamińska, and T. Walczak, “Application of MFS for 3D elastostatic problems — location of the sources and condition number analysis”, pp. 237–243 in *Recent advances in computational mechanics: Proceedings of the 20th conference on computer methods in mechanics (CMM2013)* (Poznań, Poland, 2013), edited by T. Łodygowski et al., CRC Press, Boca Raton, FL, 2014.
- [Mathon and Johnston 1977] R. Mathon and R. L. Johnston, “The approximate solution of elliptic boundary-value problems by fundamental solutions”, *SIAM J. Numer. Anal.* **14:4** (1977), 638–650.
- [de Medeiros et al. 2004] G. C. de Medeiros, P. W. Partridge, and J. O. Brandão, “The method of fundamental solutions with dual reciprocity for some problems in elasticity”, *Eng. Anal. Bound. Elem.* **28** (2004), 453–461.
- [Poullikkas 1998] A. Poullikkas, “The method of fundamental solutions for three-dimensional elastostatics problems”, *Comput. Struct.* **80** (1998), 100–107.
- [Poullikkas et al. 2001] A. Poullikkas, A. Karageorghis, and G. Georgiou, “The numerical solution of three-dimensional Signorini problems with the method of fundamental solutions”, *Eng. Anal. Bound. Elem.* **25** (2001), 221–227.
- [Poullikkas et al. 2002] A. Poullikkas, A. Karageorghis, and G. Georgiou, “The method of fundamental solutions for three-dimensional elastostatics problems”, *Comput. Struct.* **80:3-4** (2002), 365–370.
- [Walczak et al. 2014] T. Walczak, G. Sypniewska-Kaminska, B. T. Maruszewski, and K. W. Wojciechowski, “Mesh versus meshless method of elastic displacement determination in a common and an auxetic material”, *Phys. Status Solidi B* **251** (2014), 2225–2232.
- [Wojciechowski 2003] K. W. Wojciechowski, “Non-chiral, molecular model of negative Poisson ratio in two dimensions”, *J. Phys. A* **36:47** (2003), 11765–11778.
- [Yang et al. 2013] L. Yang, O. Harrysson, H. West, and D. Cormier, “Modeling of uniaxial compression in a 3D periodic re-entrant lattice structure”, *Journal of Material Science* **48** (2013), 1413–1422.
- [Zienkiewicz and Taylor 2000] O. C. Zienkiewicz and R. L. Taylor, *The finite element method, I: The basis*, 5th ed., Butterworth-Heinemann, Oxford, UK, 2000.

Received 20 Dec 2014. Revised 1 Sep 2015. Accepted 7 Oct 2015.

TOMASZ WALCZAK: tomasz.walczak@put.poznan.pl

Institute of Applied Mechanics, Poznań University of Technology, ul. Jana Pawła II 24, 60-965 Poznań, Poland

GRAZYNA SYPNIEWSKA-KAMIŃSKA: grazyna.sypniewska-kaminska@put.poznan.pl

Institute of Applied Mechanics, Poznań University of Technology, ul. Jana Pawła II 24, 60-965 Poznań, Poland

BOGDAN T. MARUSZEWSKI: bogdan.maruszewski@put.poznan.pl

Institute of Applied Mechanics, Poznań University of Technology, ul. Jana Pawła II 24, 60-965 Poznań, Poland

KRZYSZTOF W. WOJCIECHOWSKI: kww@ifmpan.poznan.pl

Institute of Molecular Physics, Polish Academy of Sciences, Smoluchowskiego 17, 60-179 Poznań, Poland

SUBMISSION GUIDELINES

ORIGINALITY

Authors may submit manuscripts in PDF format online at the Submissions page. Submission of a manuscript acknowledges that the manuscript is original and has neither previously, nor simultaneously, in whole or in part, been submitted elsewhere. Information regarding the preparation of manuscripts is provided below. Correspondence by email is requested for convenience and speed. For further information, write to contact@msp.org.

LANGUAGE

Manuscripts must be in English. A brief abstract of about 150 words or less must be included. The abstract should be self-contained and not make any reference to the bibliography. Also required are keywords and subject classification for the article, and, for each author, postal address, affiliation (if appropriate), and email address if available. A home-page URL is optional.

FORMAT

Authors can use their preferred manuscript-preparation software, including for example Microsoft Word or any variant of $\text{T}_{\text{E}}\text{X}$. The journal itself is produced in $\text{L}^{\text{A}}\text{T}_{\text{E}}\text{X}$, so accepted articles prepared using other software will be converted to $\text{L}^{\text{A}}\text{T}_{\text{E}}\text{X}$ at production time. Authors wishing to prepare their document in $\text{L}^{\text{A}}\text{T}_{\text{E}}\text{X}$ can follow the example file at www.jomms.net (but the use of other class files is acceptable). At submission time only a PDF file is required. After acceptance, authors must submit all source material (see especially Figures below).

REFERENCES

Bibliographical references should be complete, including article titles and page ranges. All references in the bibliography should be cited in the text. The use of $\text{BibT}_{\text{E}}\text{X}$ is preferred but not required. Tags will be converted to the house format (see a current issue for examples); however, for submission you may use the format of your choice. Links will be provided to all literature with known web locations; authors can supply their own links in addition to those provided by the editorial process.

FIGURES

Figures must be of publication quality. After acceptance, you will need to submit the original source files in vector format for all diagrams and graphs in your manuscript: vector EPS or vector PDF files are the most useful. (EPS stands for Encapsulated PostScript.)

Most drawing and graphing packages—Mathematica, Adobe Illustrator, Corel Draw, MATLAB, etc.—allow the user to save files in one of these formats. Make sure that what you're saving is vector graphics and not a bitmap. If you need help, please write to graphics@msp.org with as many details as you can about how your graphics were generated.

Please also include the original data for any plots. This is particularly important if you are unable to save Excel-generated plots in vector format. Saving them as bitmaps is not useful; please send the Excel (.xls) spreadsheets instead. Bundle your figure files into a single archive (using zip, tar, rar or other format of your choice) and upload on the link you been given at acceptance time.

Each figure should be captioned and numbered so that it can float. Small figures occupying no more than three lines of vertical space can be kept in the text (“the curve looks like this:”). It is acceptable to submit a manuscript with all figures at the end, if their placement is specified in the text by means of comments such as “Place Figure 1 here”. The same considerations apply to tables.

WHITE SPACE

Forced line breaks or page breaks should not be inserted in the document. There is no point in your trying to optimize line and page breaks in the original manuscript. The manuscript will be reformatted to use the journal's preferred fonts and layout.

PROOFS

Page proofs will be made available to authors (or to the designated corresponding author) at a Web site in PDF format. Failure to acknowledge the receipt of proofs or to return corrections within the requested deadline may cause publication to be postponed.

Special issue

Trends in Continuum Physics (TRECOP 2014)

Preface	BOGDAN T. MARUSZEWSKI, WOLFGANG MUSCHIK, ANDRZEJ RADOWICZ and KRZYSZTOF W. WOJCIECHOWSKI	1
Stress and displacement analysis of an auxetic quarter-plane under a concentrated force	PAWEŁ FRITZKOWSKI and HENRYK KAMIŃSKI	3
Laminar flow of a power-law fluid between corrugated plates	JAKUB KRZYSZTOF GRABSKI and JAN ADAM KOŁODZIEJ	23
A study of elastic-plastic deformation in the plate with the incremental theory and the meshless methods	MALGORZATA A. JANKOWSKA and JAN ADAM KOŁODZIEJ	41
Implementation of HAM and meshless method for torsion of functionally graded orthotropic bars	ANITA UŚCIEŁOWSKA and AGNIESZKA FRASKA	61
The application of the method of fundamental solutions in modeling auxetic materials	TOMASZ WALCZAK, GRAZYNA SYPNIEWSKA-KAMIŃSKA, BOGDAN T. MARUSZEWSKI and KRZYSZTOF W. WOJCIECHOWSKI	79

